Depth-Dependent Physiological Modulators of the BOLD Response in the Human Motor Cortex

Von der Fakultät für Physik und Geowissenschaften
der Universität Leipzig
genehmigte

D I S S E R T A T I O N

zur Erlangung des akademischen Grades
Doctor Rerum Naturalium
(Dr. rer. nat.)

vorgelegt
von Master of Science (M.Sc.) Maria Guidi

Gutachter: Prof. Dr. Harald E. Möller
Prof. Dr. David G. Norris

Tag der Verleihung: 26. Februar 2018

FAKULTÄT FÜR PHYSIK UND
GEOWISSENSCHAFTEN DER UNIVERSITÄT
LEIPZIG

MAX-PLANCK-INSTITUT FÜR KOGNITIONS- UND
NEUROWISSENSCHAFTEN

MAX-PLANCK-GESELLSCHAFT

Maria Guidi: *Depth-Dependent Physiological Modulators of the BOLD Response in the Human Motor Cortex*

È molto meglio non sapere una cosa, che saperla male.

— Unknown Professor

Dedicated to my parents, my grandparents,
and the other people of that history.

And, once again,
to Rondizzoni.

BIBLIOGRAPHISCHE BESCHREIBUNG

Dissertation von Maria Guidi, Universität Leipzig

DEPTH-DEPENDENT PHYSIOLOGICAL MODULATORS OF THE BOLD RESPONSE IN THE HUMAN MOTOR CORTEX

191 Seiten, 225 Literaturangaben, 60 Abbildungen, 6 Tabellen

Referat:

This dissertation proposes a set of methods for improving spatial localization of cerebral metabolic changes using functional magnetic resonance imaging (fMRI).

Blood oxygen level dependent (BOLD) fMRI estabilished itself as the most frequently used technique for mapping brain activity in humans. It is non-invasive and allows to obtain information about brain oxygenation changes in a few minutes. It was discovered in 1990 and, since then, it contributed enormously to the developments in neuroscientific research.

Nevertheless, the BOLD contrast suffers from inherent limitations. This comes from the fact that the observed response is the result of a complex interplay between cerebral blood flow (CBF), cerebral blood volume (CBV) and cerebral metabolic rate of oxygen consumption (CMRO2) and has a strong dependency on baseline blood volume and oxygenation. Therefore, the observed response is mislocalized from the site where the metabolic activity takes place and it is subject to high variability across experiments due to normal brain physiology. Since the peak of BOLD changes can be as much as 4 mm apart from the site of metabolic changes, the problem of spatial mislocalization is particularly constraining at submillimeter resolution.

Three methods are proposed in this work in order to overcome this limitation and make data more comparable. The first method involves a modification of an estabilished model for calibration of BOLD responses (the dilution model), in order to render it applicable at higher resolutions. The second method proposes a model-free scaling of the BOLD response, based on spatial normalization by a purely vascular response pattern. The third method takes into account the hypothesis that the cortical vasculature could act as a low-pass filter for BOLD fluctuations as the blood is carried downstream, and investigates differences in frequency composition of cortical laminae.
All methods are described and tested on a depth-dependent scale in the human motor cortex.

LIST OF PUBLICATIONS

Parts of text and figures present in this thesis have appeared previously in the material listed below.

PAPERS

1. Maria Guidi, Laurentius Huber, Leonie Lampe, Claudine J. Gauthier, and Harald E. Möller. Lamina-dependent calibrated BOLD response in human primary motor cortex. *NeuroImage*, 141:250–261, 2016.

2. Laurentius Huber, Dimo Ivanov, Daniel A. Handwerker, Sean Marrett, Maria Guidi, Kâmil Uludağ, Peter A. Bandettini, and Benedikt A. Poser. Techniques for blood volume fMRI with VASO: From low-resolution mapping towards sub-millimeter layer-dependent applications. *NeuroImage*, 2016.

3. Laurentius Huber, Dimo Ivanov, Maria Guidi, Robert Turner, Kâmil Uludağ, Harald E. Möller, and Benedikt A. Poser. Functional cerebral blood volume mapping with simultaneous multislice acquisition. *NeuroImage*, 125:1159–1168, 2015.

4. Laurentius Huber, Jozien Goense, Aneurin J. Kennerley, Robert Trampel, Maria Guidi, Enrico Reimer, Dimo Ivanov, Nicole Neef, Claudine J. Gauthier, Robert Turner, and Harald E. Möller. Cortical lamina-dependent blood volume changes in human brain at 7 T. *NeuroImage*, 107:23–33, 2015.

ORAL PRESENTATIONS

1. Maria Guidi, Irati Markuerkiaga, Lauren J. Bains, Laurentius Huber, Harald E. Möller, and David G. Norris. Frequency signature of cortical laminar fMRI. *Proceedings of the 25th Annual Meeting of the International Society for Magnetic Resonance in Medicine, Honolulu, HI, USA*, abstract 158, 2017.

2. Laurentius Huber, Daniel A. Handwerker, Andrew Hall, David C. Jangraw, Javier Gonzales-Castillo, Maria Guidi, Dimo Ivanov, Benedikt A. Poser, and Peter A. Bandettini. Cortical depth-dependent fMRI: heterogeneity across tasks, across participants, across days and along the cortical ribbon. *Proceedings of the 25th Annual Meeting of the International Society for Magnetic Resonance in Medicine, Honolulu, HI, USA*, abstract 237, 2017.

3. Maria Guidi, Laurentius Huber, Leonie Lampe, and Harald E. Möller. Cortical laminar resting-state fluctuations scale with hypercapnic response. *Proceedings of the 24th Annual Meeting of the International Society for Magnetic Resonance in Medicine, Singapore*, abstract 769, 2016.

4. Laurentius Huber, Daniel Handwerker, Javier Gonzales-Castillo, Sean Marrett, Maria Guidi, Dimo Ivanov, Benedikt Poser, Jozien Goense, and Peter A. Bandettini. Directional connectivity measured with layer-dependent fMRI in human sensory-motor system. *3rd Biennial Whistler Scientific Workshop on Brain Functional Organization, Connectivity and Behavior, Whistler, BC, Canada*, 2016.

5. Laurentius Huber, Daniel Handwerker, Javier Gonzales-Castillo, David Jangraw, Maria Guidi, Dimo Ivanov, Benedikt A. Poser, Jozien B.M. Goense, and Peter A. Bandettini. Effective Connectivity Measured with Layer-Dependent Resting-State Blood Volume FMRI in Humans. *Proceedings of the 24th Annual Meeting of the International Society for Magnetic Resonance in Medicine, Singapore*, abstract 948, 2016.

6. Maria Guidi, Laurentius Huber, Leonie Lampe, Claudine J. Gauthier, and Harald E. Möller. Layer-dependent calibrated BOLD response in human M1. *Proceedings of the 23rd Annual Meeting of the International Society for Magnetic Resonance in Medicine, Toronto, ON, Canada*, abstract 358, 2015.

7. Maria Guidi, Laurentius Huber, Leonie Lampe, Claudine J. Gauthier, and Harald E. Möller. Layer-dependent calibrated BOLD in human M1. *1st Summer School of Ultra-High Field Magnetic Resonance Imaging, Isola d'Elba, Italy*, 2015.

8. Laurentius Huber, Dimo Ivanov, Maria Guidi, Rober Turner, Kâmil Uludağ, and Harald E. Möller. Simultaneous multi-slice functional CBV measurements at 7 T. *Proceedings of the 23rd Annual Meeting of the International Society for Magnetic Resonance in Medicine, Toronto, ON, Canada*, abstract 600, 2015.

9. Harald E. Möller, Laurentius Huber, Maria Guidi, Juliane Dinse, and Pierre Louis Bazin. Unraveling cortical laminae with anatomical and functional MRI at 7.0 T. *6th Annual Scientific Symposium on Ultrahigh Field Magnetic Resonance, Berlin, Germany*, 2015.

10. Harald E. Möller, Laurentius Huber, Maria Guidi, and Robert Turner. Beyond BOLD-based fMRI: High-resolution mapping of blood volume changes related to neural activity. *1st Summer School of Ultra-High Field Magnetic Resonance Imaging, Isola d'Elba, Italy*, 2015.

11. Maria Guidi, Laurentius Huber, Leonie Lampe, Claudine J. Gauthier, and Harald E. Möller. Layer-dependent calibrated BOLD in human M1. *Proceedings of the 2nd Workshop on Imaging Cerebral Physiology: Manipulating Magnetic Resonance Contrast through Respiratory Challenges, Leipzig, Germany*, 2014.

12. Laurentius Huber, Jozien B.M. Goense, Aneurin Kennerley, Robert Trampel, Maria Guidi, Claudine J. Gauthier, Robert Turner, and Harald E. Möller. Layer-dependent CBV and BOLD responses in humans, monkeys, and rats at 7T. *ISMRM Workshop on Functional MRI: Emerging Techniques and New Interpretations, Charleston, SC, USA*, 2014.

13. Laurentius Huber, Aneurin Kennerley, Claudine J. Gauthier, Steffen Krieger, Maria Guidi, Dimo Ivanov, Robert Turner, and Harald E. Möller. Cerebral blood volume redistribution during hypercapnia. *Proceedings of the 2nd Workshop on Imaging Cerebral Physiology: Manipulating Magnetic Resonance Contrast through Respiratory Challenges, Leipzig, Germany*, 2014.

POSTERS

1. Maria Guidi, Christopher J. Steele, Laurentius Huber, Leonie Lampe, Viola Rjosk, Pierre Louis Bazin, and Harald E. Möller. High-Resolution CMRO2 Mapping During a Unilateral Pinch-Force Task *Proceedings of the 24th Annual Meeting of the International Society for Magnetic Resonance in Medicine, Singapore*, abstract 1720, 2016.

2. Maria Guidi, Christopher J. Steele, Laurentius Huber, Leonie Lampe, Viola Rjosk, Pierre Louis Bazin, and Harald E. Möller. High-Resolution CMRO2 Mapping During a Unilateral Pinch-Force Task *6th IMPRS NeuroCom Summer School, Leipzig, Germany*, 2016.

3. Laurentius Huber, Jozien B.M. Goense, Aneurin Kennerley, Maria Guidi, Robert Trampel, Robert Turner, and Harald E. Möller. Micro- and macrovascular contributions to layer-dependent blood volume fMRI: A multi-modal, multi-species comparison. *Proceedings of the 23rd Annual Meeting of the International Society for Magnetic Resonance in Medicine, Toronto, ON, Canada*, abstract 2114, 2015.

4. Laurentius Huber, Maria Guidi, Jozien B.M. Goense, Toralf Mildner, Robert Trampel, Jessica Schulz, Cornelius Eichner, Robert Turner, and Harald E. Möller. The magnitude point spread function is an inadequate measure of T2*-blurring in EPI. *Proceedings of the 23rd Annual Meeting of the International Society for Magnetic Resonance in Medicine, Toronto, ON, Canada*, abstract 2056, 2015.

5. Miguel Martínez-Maestro, Maria Guidi, Laurentius Huber, Štefan Holiga, Henrik Marschner, and Harald E. Möller. fMRS of visual cortex at 3T with periodic averaging of a block design paradigm. *Proceedings of the 23rd Annual Meeting of the International Society for Magnetic Resonance in Medicine, Toronto, ON, Canada*, abstract 4638, 2015.

6. Christian Labadie, Tomas Siegert, Enrico Reimer, Maria Guidi, Miguel Martínez-Maestro, Harald E. Möller, Robert Turner, and Jessica Schulz. Adaptive motion correction of single-voxel spectroscopy with real-time frequency correction at 3T and 7T. *Proceedings of the 22nd Annual Meeting of the International Society for Magnetic Resonance in Medicine, Milano, Italy*, 2014.

7. Miguel Martínez-Maestro, Maria Guidi, Christian Labadie, and Harald E. Möller. Should beginners revisit the ancient and honourable art of shimming at high fields? *Proceedings of the 22nd Annual Meeting of the International Society for Magnetic Resonance in Medicine, Milano, Italy*, abstract 7332, 2014.

AWARDS AND STIPENDS

1. ISMRM Summa cum Laude Merit Award for the conference talk: Layer-dependent calibrated BOLD response in human M1. *23rd Annual Meeting of the International Society for Magnetic Resonance in Medicine, Toronto, ON, Canada*, 2015.

2. ISMRM Magna cum Laude Merit Award for the conference poster: Should beginners revisit the ancient and honourable art of shimming at high fields? *22nd Annual Meeting of the International Society for Magnetic Resonance in Medicine, Milano, Italy*, 2014.

3. ISMRM Trainee Educational Stipend, for the *25th Annual Meeting of the International Society for Magnetic Resonance in Medicine, Honolulu, HI, USA*, 2017.

4. ISMRM Trainee Educational Stipend, for the *24th Annual Meeting of the International Society for Magnetic Resonance in Medicine, Singapore*, 2016.

5. ISMRM Trainee Educational Stipend, for the *23rd Annual Meeting of the International Society for Magnetic Resonance in Medicine, Toronto, ON, Canada*, 2015.

ACKNOWLEDGMENTS

I would like to acknowledge the people that contributed, in many different ways, to the development of this work.

First of all, I would like to sincerely thank my supervisor, Prof. Harald Möller, for his guidance throughout these years. Apart from his great scientific advice, I deeply acknowledge him for his extremely supportive and positive attitude.

I enormously thank Renzo Huber for getting me started into the field of layer fMRI. I am really happy my thesis ended up being focused on layers, and even more about the fact that I had the chance to work side-by-side with him. I also acknowledge him for his comic recommendations.

I would like to sincerely thank Christian Labadie for his great scientific help. He has been a great teacher during my first PhD year, and a valuable colleague afterwards.

I want to thank the group at the Donders Center in Nijmegen for being a great host during my secondment. I would like to give a special mention to Prof. David Norris for his great guidance and for trasmitting to me some of his enthusiasm for research. I deeply acknowledge Irati Markuerkiaga for helping me in any possible way. I only regret we have worked together for such a short time. I thank Lauren Bains for helping me setting up the 3D sequence and for taking the time to drive down to Essen. I also acknowledge Benedikt Poser for sequence support.

I would like to thank Alberto Merola, Esther Kühn and Pierre-Louis Bazin for helpful discussion. I thank Oleksii Omelchenko for great help with FSL and interesting discussion. I want to thank Christopher Steele for teaching me how to use the pinch-force system and helping with the analysis.

I am really thankful to the somatosensory group for setting up a great collaboration: Birol Taskin, Norman Forschack, Martin Grund, Till Nierhaus and Prof. Arno Villringer.

I would like to thank the MTAs for their great help, with a special mention to Domenica Wilfling for her outstanding support. I want to thank the physicians that helped me many times during the gas manipulation experiments: Leonie Lampe, Viola Rjosk, Kristin Ihle, Fabian Piecha. I am thankful to Enrico Reimer for his help with data transfer and software support. I want to thank Robert Trampel for scanner maintenance and support. I want to thank Claudine Gauthier and Steffen von Smuda for setting up the gas delivery system.

I would like to thank the NMR group for creating a positive working environment. Especially, I highly thank my friend, yoga teacher and

colleague Kathrin Lorenz for the harmony she brought in our office. I also acknowledge her for helium refilling. I am thankful to my friend Miguel Martínez-Maestro; I am grateful I had the chance to collaborate with him. I would like to thank Manoj Shrestha, Henrik Marschner, Tobias Lenich, Susanne Fuchs, Riccardo Metere, Ahmad Kanaan, Franz Patzig, Jakob Georgi, Jens Bode and Štefan Holiga for being ©AWESOME colleagues and friends. I want to thank Robert Trampel for taking the time to stop by our office everyday and for telling me a lot of things I wish I never heard of. I thank him also for fashion advices.

I want to thank all the people of the HiMR group. It has been a pleasure and fun being part of it.

The deepest acknowledgement goes to my family. They are by far the people who taught me the most, and to whom I dedicated my daily work.

I would like to acknowledge the European Union for funding this PhD through the Marie Curie ITN "HiMR".

A final mention goes to researchers from Magdeburg for giving me the right input to start writing this thesis: Arturo Cardenas-Blanco, Julio Acosta-Cabronero, Jose Pedro Valdes-Herrera.

CONTENTS

LIST OF FIGURES

LIST OF TABLES

ACRONYMS

AAT	arterial arrival time
ACS	autocalibration signal
ADP	adenosine diphosphate
ALFF	amplitude of low-frequency fluctuations
AP	action potential
ASL	arterial spin labeling
ATP	adenosine triphosphate
$\mathbf{B_0}$	external magnetic field
$\mathbf{B_1}$	time-varying magnetic field
$\mathbf{B_{eff}}$	effective magnetic field
CASL	continuous arterial spin labeling
CNR	contrast-to-noise ratio
CV	coefficient of variation
CVR	cerebrovascular reactivity
ΔB	field offset
$\Delta\omega$	frequency offset
BOLD	blood oxygen level dependent
CBF	cerebral blood flow
CBV	cerebral blood volume
CBV_o	resting cerebral blood volume
CMR_{glc}	cerebral metabolic rate of glucose consumption
$CMRO_2$	cerebral metabolic rate of oxygen consumption
CSF	cerebrospinal fluid
dHb	deoxy-haemoglobin

EEG	electroencephalography
$\mathcal{E}$	electromotive force
EPI	echo-planar imaging
EPSP	excitatory post-synaptic potential
EV	extravascular
EVI	echo-volumar imaging
fALFF	fractional amplitude of low-frequency fluctuations
fFA	fractional fluctuation amplitude
FID	free-induction decay
θ	flip angle
fMRI	functional magnetic resonance imaging
FOV	field of view
GABA	gamma-aminobutyric acid
Gln	glutamine
Glu	glutamate
GM	gray matter
G_P	phase encoding gradient
G_R	readout or frequency encoding gradient
GRE	gradient recalled echo
G_s	slice-selection gradient
Hb	haemoglobin
HRF	haemodynamic response function
ICV	intra-cortical vein
IPSP	inhibitory post-synaptic potential
IV	intravascular
k_B	Boltzmann's constant
LFP	local field potential
M	calibration parameter
$\mathbf{M}$	magnetization

$\mathbf{M_0}$	equilibrium magnetization
M1	primary motor cortex
MION	monocrystalline iron oxide nanoparticle
MR	magnetic resonance
MRI	magnetic resonance imaging
$\boldsymbol{\mu}$	magnetic moment
NMR	nuclear magnetic resonance
NO	nitric oxide
OEF	oxygen extraction fraction
ω_0	Larmor frequency
ω_{eff}	effective Larmor frequency
PASL	pulsed arterial spin labeling
pCASL	pseudo-continuous arterial spin labeling
PET	positron-emission tomography
$P_{ET}CO_2$	end-tidal partial pressure of carbon dioxide
$P_{ET}O_2$	end-tidal partial pressure of oxygen
Φ_M	magnetic flux
pMRI	parallel imaging
PSF	point spread function
PSU	post-stimulus undershoot
R_2	intrinsic transverse relaxation rate, equal to $1/T_2$
R_2^*	effective transverse relaxation rate, equal to $1/T_2^*$
R_2'	transverse relaxation rate due to field inhomogeneities, equal to $1/T_2'$
RF	radiofrequency
ROI	region of interest
RSFA	resting-state fluctuation amplitude
S1	primary somatosensory cortex
SAR	specific absorption rate

SE	spin echo
SEM	standard error of the mean
SMS	simultaneous multi-slice
SNR	signal-to-noise ratio
SO_2	oxygen saturation
SS-SI-VASO	slice-saturation slab-inversion VASO
T	temperature
T_A	acquisition time
T_1	spin-lattice longitudinal relaxation time
T_2	spin-spin (intrinsic) transverse relaxation time
T_2^*	effective transverse relaxation time
T_2'	transverse relaxation time due to field inhomogeneities
T_E	echo time
TI	inversion time
T_R	repetition time
tSD	temporal standard deviation
tSNR	temporal signal-to-noise ratio
V1	primary visual cortex
VASO	vascular space occupancy
Δx	voxel size
WM	white matter

Part I

INTRODUCTION

1 INTRODUCTION

Functional magnetic resonance imaging (fMRI) was discovered in 1990, relatively short after magnetic resonance (MR) scanners became commonly available in the clinic, which was around 1984.
The first blood oxygen level dependent (BOLD) human brain activation maps were obtained in the early '90s (Bandettini et al., 1992; Kwong et al., 1992; Ogawa et al., 1993). fMRI opened up a completely new way of observing the brain, making it possible to map brain activity via local changes in cerebral oxygenation. With the advent of echo-planar imaging (EPI) in clinical scanners, around 1996, fMRI "took off" and, since then, the number of published papers per year steadily increased (Bandettini, 2012).
BOLD fMRI dramatically influenced the way of doing neuroscientific research and became the most used imaging technique for studying brain function and connectivity.

Gradient echo (GRE) BOLD contrast increases upon activation due to an increase in oxygenation. The increase in oxygenation, rather than decrease, was already observed in previous work using PET (Fox and Raichle, 1986). Nevertheless, the chemical and biological processes behind it were not completely understood, and many questions are to date not answered.
In fact, oxygenation changes originate from a complex interplay of cerebral blood flow (CBF), cerebral blood volume (CBV) and cerebral metabolic rate of oxygen ($CMRO_2$), and the amplitude of the response depends on baseline blood volume and baseline oxygenation as well (Davis et al., 1998).
Such dependencies are putting a constraint on the interpretability of the technique, because a signal increase is originated by an unknown set of CBV, CBF and CMRO2 changes that cannot be deduced without additional measurements. Moreover, BOLD amplitude can vary substantially even if the neuronal activity does not, for example under the effect of caffeine (Chen and Parrish, 2009) or even under normal brain physiology.
These limitations are, thus, inherent to the data. Additionally, a number of routinely used pre- or post-processing steps are even further reducing data interpretability, which made the fMRI field face severe critiques (Eklund et al., 2016; Stelzer et al., 2014).

Alternative functional imaging techniques characterized by better spatial specificity and comparability are available. For example spin-echo (SE) BOLD imaging, arterial spin labeling (ASL) and vascular-space occupancy (VASO). Even though those are estabilished tech-

niques, they are not as widely used as GRE-BOLD, due to the fact that they have lower sensitivities and are also more cumbersome to implement. Finally, the data may require a number of non-standard analysis steps in order to be interpretable.
The spatial scale of brain activation seems to be in the order of several micrometers to centimeters, which makes signal changes detectable for macroscopic voxels size and, at the same time, makes the strive for higher resolution investigations and more spatially specific techniques meaningful (Bandettini, 2012).

In this sense, fMRI has been shown to benefit from higher field strengths, due to the increase in signal changes and in specificity to the cortical tissue (van der Zwaag et al., 2015). Namely, the temporal signal-to-noise ratio (tSNR), which is relevant for fMRI, increases linearly with field strength. However, this relationship allows a linear resolution increase of only about 25% when moving from 3 T to 7 T, if the same tSNR is desired.
Moreover, GRE-BOLD is weighted towards the venous blood due to its relatively high deoxygenated haemoglobin content and baseline volume. The draining veins comparment is, thus, the one undergoing the largest BOLD signal change but is located away from the capillary bed, and can be several millimeters apart from the site of neuronal activity (Turner, 2002). This effect has been recognized in the early days of fMRI, but became more recently a practical impedement due to the higher resolutions employed (Menon, 2002).

1.1 PURPOSE OF THIS WORK

This works aims at reducing, if not eliminating, some of the limitations in BOLD acquisitions listed in the previous section.
The principal targets are:

- Improve existing methods for metabolic fMRI to target submillimeter resolution.
- Develop novel methods to improve the spatial specificity and reproducibility of the BOLD response.
- Investigate spatial and temporal features of the BOLD response at submillimeter resolution.

In order to tackle those points, a field strength of 7 T is used, and novel acquisition methods are combined with improved analysis strategies and modeling.

In terms of acquisition, the SS-SI-VASO method (Huber et al., 2014b), i. e., a VASO variant optimized for field strengths of 7 T, has proven to be advantageous in terms of sensitivity with respect to the original VASO contrast (Lu et al., 2003), to be applicable at high resolutions,

and to be more specific to the capillary bed than GRE-BOLD. SS-SI-VASO signal changes are proportional to CBV changes, which are generally coupled to CBF changes (Grubb et al., 1974).
The dilution model (Davis et al., 1998; Hoge et al., 1999) offers a relationship between CBF and BOLD changes, and allows to find $CMRO_2$ changes. Therefore, its usage in combination with VASO data is investigated.

BOLD signal normalization by a breathing manipulation has also been proposed for reducing inter-subject variability due to vascular reactivity features (Bandettini and Wong, 1997), and has been demonstrated with resting-state data as well (Kannurpatti and Biswal, 2008). Its applicability is studied in this work at submillimeter resolutions, and compared to the dilution model results.

The human neocortex is divided into 6 cortical layers, which are segregated by function (input/output). Moreover, vascular features are approximately homogeneous within layers, with the highest venous vascular density in correspondence of upper layers and decreasing towards deeper layers. Therefore, given their homogeneous vascular and functional characteristics, signal averaging within layers should improve tSNR, and may represent a convenient target for a proof of principle of the methods proposed.

1.2 STRUCTURE OF THE THESIS

Apart from the Introduction (this part) and Conclusion, this dissertation is composed of the following parts: Background, Methods and Results.

The Background section reviews the physical principles behind nuclear magnetic resonance (NMR) and MRI, introduces the physiological mechanisms responsible for BOLD signal changes (the neurovascular coupling) and the relevance of mapping CBF and CBV changes. Finally, it describes the anatomical and functional features of the cortical layers.

The Methods section is divided into three Chapters: the first one describes how the SS-SI-VASO technique works and how it can be combined with simultaneous multi-slice and three-dimensional readouts. The second Chapter describes the Davis model for calibration in its original formulation and in its "modified formulation", developed in this work. The last Chapter lists the vascular reactivity indices that can be extracted from resting-state BOLD data, and the impact of noise in high resolution acquisitions.

The Results section summarizes, in three Chapters, the achievement obtained. The results from the modified BOLD model are presented in the first Chapter. The second Chapter shows the results obtained from scaling the BOLD response with the resting-state fluc-

tuation amplitude. The third chapter deals with the frequency composition of the BOLD response in different cortical layers.

Part II

BACKGROUND

2

THE BASICS OF MRI

Thanks to magnetic resonance imaging (MRI), it is possible to obtain accurate pictures of the brain and of other structures in the body non-invasively. Magnetic resonance scanners are a powerful research and diagnostic tool, and are nowadays worldwide available. The physical phenomenon behind MRI is the nuclear magnetic resonance (NMR). The history of NMR could be dated back to 1933, when the physicist Otto Stern published his work about the discovery of the magnetic moment of protons (Frisch and Stern, 1933; Estermann and Stern, 1933). Ten years later, he was awarded a Nobel prize. Several other nobel prizes were awarded to NMR-related discoveries in the following years: to the physicist Isidor Isaac Raabi in 1944 for the discovery of magnetic resonance in nuclei (Rabi, 1937; Rabi et al., 1939); to the physicists Felix Bloch and Edward Mills Purcell in 1952 for the discovery of NMR in liquids and solids (Fig. 1) (Bloch et al., 1946; Purcell et al., 1946); to the physical chemist Richard Robert Ernst in 1991 for dramatically improving the sensitivity of NMR spectra (Ernst and Anderson, 1966; Jeener et al., 1979); to the chemist/biophysicist Kurt Wüthrich in 2002 for determining the three-dimensional structure and dynamics of macromolecules using NMR (Kumar et al., 1980); to the chemist Paul Christian Lauterbur and to the physicist Sir Peter Mansfield in 2003 for discovering MRI and fast acquisition techniques (Lauterbur, 1973; Mansfield, 1977).

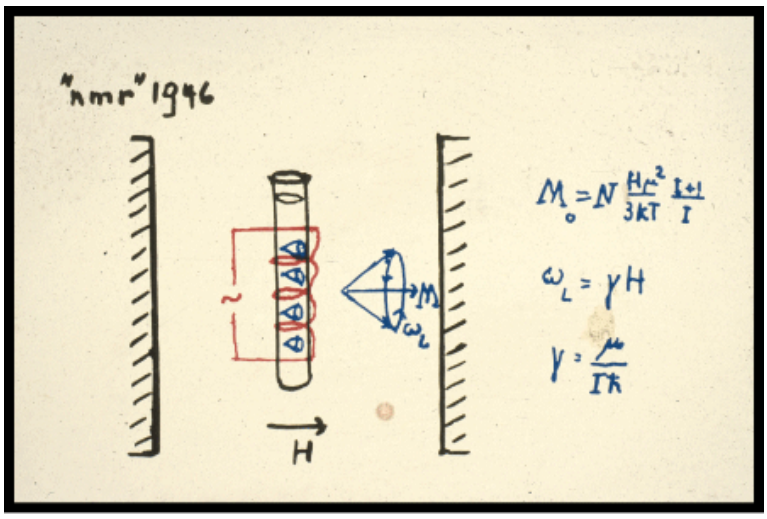

Figure 1: Page from Bloch's notebook showing the theory behind his famous experiment. Picture and description from (Elster, 2017).

This chapter provides the basics for understanding the NMR phenomenon, the generation of magnetic resonance (MR) images, pulse sequences, and some consideration about magnetic field strengths.
In Section 2.1, a quantum mechanical description of NMR is provided. The description focuses exclusively on ^1H nuclei due to their abundancy in the human body and the fact that they are the major contributors to the MR-signal. Section 2.2 reviews the basics of slice selection, phase and frequency encoding, and their k-space representation; Section 2.3 describes the principle of echo formation and echo-planar imaging (EPI); Section 2.4 lists some advantages and disadvantages of MRI for increasing field strengths.

This background chapter includes information from the following references: (Hornack, 2017; Seo et al., 2014; Ivanov, 2012; Buxton, 2009; Bernstein et al., 2004; Haacke et al., 1999).

2.1 THE NUCLEAR MAGNETIC RESONANCE PHENOMENON

2.1.1 *Interaction of Spins with an External Magnetic Field*

The interaction between nuclear spins and an external magnetic field ($\mathbf{B_0}$) is at the basics of the NMR phenomenon.

The spin of spin-1/2 particles, $\hat{\mathbf{S}}$, is a quantum mechanical operator described by:

$$\hat{\mathbf{S}} = \frac{\hbar}{2}\boldsymbol{\sigma} \tag{1}$$

where $\hbar$ is the Planck constant divided by 2π and $\boldsymbol{\sigma}$ are the Pauli matrices:

$$\sigma_x = \begin{pmatrix} 0 & 1 \\ 1 & 0 \end{pmatrix},\ \sigma_y = \begin{pmatrix} 0 & -i \\ i & 0 \end{pmatrix},\ \sigma_z = \begin{pmatrix} 1 & 0 \\ 0 & -1 \end{pmatrix}. \tag{2}$$

A magnetic moment ($\boldsymbol{\mu}$) is associated to a non-zero spin:

$$\boldsymbol{\mu} = \gamma\hat{\mathbf{S}} = \gamma\frac{\hbar}{2}\boldsymbol{\sigma} \tag{3}$$

where γ is the gyromagnetic ratio, which is specific for each nucleus. For ^1H nuclei, $\gamma/2\pi = 42.577$ MHz/T.
If an external magnetic field $\mathbf{B_0}$ is applied, the interaction with the dipole can be described by the Zeeman effect, with the hamiltonian $\hat{\mathbf{H}}$:

$$\hat{\mathbf{H}} = -\boldsymbol{\mu}\cdot\mathbf{B_0}. \tag{4}$$

The eigenvalues represent the discrete energy states, E_m:

$$E_m = -m\gamma\hbar B_0 \tag{5}$$

where m is the projection of the spin operator along the z-axis and it was assumed $\mathbf{B_0}$ to fulfill $B_x = B_y = 0$ and $B_z = B_0 = |\mathbf{B_0}|$. Taking into account ^1H nuclei (protons), $m = \pm 1/2$ and, thus, only two energy states are possible. The difference in energy between the spin-down and spin-up state can be written as:

$$\Delta E = E_{-1/2} - E_{+1/2} = \gamma \hbar B_0. \tag{6}$$

From Eq. 6 it can be seen that the parallel alignment of spins has a lower energy than the antiparallel alignment.

Boltzmann's statistics

If a group of spins is placed into a magnetic field, some of them align parallel to the external field, and some of them antiparallel to it. Since the parallel orientation corresponds to a lower energy state, slightly more spins have that orientation (Eq. 6). The ratio of the amount of spin up ($N_{+1/2}$) versus spin down ($N_{-1/2}$) follows Boltzmann's statistics:

$$\frac{N_{+1/2}}{N_{-1/2}} = e^{-\Delta E / k_B T}, \tag{7}$$

where k_B is the Boltzmann constant and T the temperature. Thus, at room temperature, only a very small fraction of spins is aligned parallel to the external magnetic field (the ratio in Eq. 7 is approximately 10^{-5} for a field strength of 7 T). The mismatch between spins up and spins down makes it possible to record a non-zero NMR signal. Therefore, the ratio in Eq. 7 is important because determines the upper limit of the intensity of the signal.

The Larmor frequency

Spins in a magnetic field precess with a characteristic frequency determined by their gyromagnetic ratio and the external field. It is denoted Larmor frequency (ω_0) and fulfills the equation:

$$\omega_0 = \gamma B_0. \tag{8}$$

Therefore, the energy difference between the spin up and the spin down state, can as well be written as:

$$\Delta E = \hbar \omega_0, \tag{9}$$

where Eq. 8 was substituted into Eq. 6.

2.1.2 *Macroscopic Magnetization*

The fact that the amount of spins aligned perpendicular to $\mathbf{B_0}$ outnumbers the amount of antiparallel spins, results in a net macroscopic magnetization $\mathbf{M_0}$, also called equilibrium magnetization ($M_z = |\mathbf{M_0}|$). Generally, the magnetization ($\mathbf{M}$) can be expressed as:

$$\mathbf{M} = \frac{d\boldsymbol{\mu}}{dV} \tag{10}$$

where dV is the volume element. An ensamble of spins having the same phase within dV is termed isochromat, and can be taken to behave in a similar way as a single dipole.

The effective magnetic field

According to Larmor equation, an external magnetic field produces a torque on any magnetic moments and, in turn, on the object magnetization in the assumption of non-interacting protons within each isochromat. The precession of the magnetization is described by the following equation of motion:

$$\frac{d\mathbf{M}}{dt} = \gamma \mathbf{M} \times \mathbf{B_{eff}} \tag{11}$$

where $\mathbf{B_{eff}}$ is the effective magnetic field and consists of a superposition of two fields: the constant $\mathbf{B_0}$ and the time-varying magnetic field ($\mathbf{B_1}$) perpendicular to the z-axis.
The spins are, thus, precessing around the direction of effective magnetic field ($\mathbf{B_{eff}}$) with an effective Larmor frequency ω_{eff}:

$$\omega_{eff} = \gamma B_{eff}. \tag{12}$$

$\mathbf{B_1}$ is a circularly polarized magnetic field in the xy plane:

$$\mathbf{B_1}(t) = B_1 \big(\cos(\omega_{RF} t)\hat{x} - \sin(\omega_{RF} t)\hat{y} \big), \tag{13}$$

where ω_{RF} is the frequency of rotation and, thus, $\mathbf{B_{eff}}$ can be written as:

$$\mathbf{B_{eff}} = B_1 \left(\cos(\omega_{RF} t)\hat{x} - \sin(\omega_{RF} t)\hat{y}\right) + B_0 \hat{z} \tag{14}$$

The rotating frame of reference

A rotating frame of reference is usually defined for convenience. The rotation matrix for a rotation around the z axis is:

$$R(\omega t) = \begin{pmatrix} \cos(\omega t) & -\sin(\omega t) \\ \sin(\omega t) & \cos(\omega t) \end{pmatrix} \tag{15}$$

And the transformation from the laboratory (fixed) reference frame to the rotating one for a generic vector $\mathbf{V}$ follows:

$$\left(\frac{d\mathbf{V}(t)}{dt}\right)_{lab} = \left(\frac{d\mathbf{V}(t)}{dt}\right)_{rot} + \mathbf{\Omega} \times \mathbf{V}(t)_{lab} \tag{16}$$

where $\mathbf{\Omega} = -\omega\hat{z}$ is the angular velocity and ω the angular frequency of the rotating frame.
In the rotating frame, the magnetization equation of motion (Eq. 11) becomes (making use of Eq. 11 and of $\mathbf{\Omega} = -\omega\hat{z}$):

$$\begin{aligned} \left(\frac{d\mathbf{M}}{dt}\right)_{rot} &= \frac{d\mathbf{M}}{dt} - \mathbf{\Omega} \times \mathbf{M} = \gamma \mathbf{M} \times \mathbf{B_{eff}} - \frac{\mathbf{\Omega}}{\gamma} \times \gamma \mathbf{M} = \\ &= \gamma \mathbf{M} \times (\mathbf{B_{eff}})_{rot} \end{aligned} \tag{17}$$

where $(\mathbf{B_{eff}})_{rot}$ is:

$$\begin{aligned}(\mathbf{B_{eff}})_{rot} =& B_1 \cos((\omega_{RF} - \omega)t)\hat{x} - B_1 \sin((\omega_{RF} - \omega)t)\hat{y} \\ &+ \left(B_0 - \frac{\omega}{\gamma}\right)\hat{z}\end{aligned} \tag{18}$$

where ω_{RF} is the frequency of the oscillating field in the rotating frame of reference and ω is the frequency of the rotating frame of reference with respect to the laboratory frame of reference.
If the frame of reference is on resonance, i. e., it rotates at the Larmor frequency ($\omega = \omega_0$), the $\hat{z}$ component in Eq. 18 is equal to zero and $\mathbf{B_1}$ appears stationary. Therefore, the magnetization precesses around an axis in the transverse plane.
Therefore, the pulse can be used to tilt the magnetization and the amount of tilting depends on the pulse duration τ and amplitude B_1:

$$\theta = \gamma \int_0^\tau B_1(t)dt. \tag{19}$$

where θ is the flip angle. For $\theta = 90°$, the magnetization is rotated to the transverse plane; for $\theta = 180°$, the magnetization is inverted.

2.1.3 *Relaxation and Bloch Equation*

During the application of a radiofrequency (RF) pulse, the magnetization is flipped by a certain flip angle (θ). After the pulse is played out, the magnetization will start to relax to the equilibrium value, $\mathbf{M_0}$.

There are two main processes that govern the rate of relaxation and are due to the interaction of the spins with their surrounding and with each other, respectively.

Spin-lattice relaxation

The spin-lattice longitudinal relaxation time (T_1) represents the energy exchange between the nuclei and the lattice they are embedded in. It is responsible for the relaxation of the longitudinal component of the magnetization, and can be described in the following way:

$$\frac{dM_z(t)}{dt} = -\frac{M_z(t) - M_0}{T_1}. \tag{20}$$

Spin-spin relaxation

The spin-spin (intrinsic) transverse relaxation time (T_2) reflects the dephasing due to the interaction among nuclei. It is responsible for the decay of the transverse components, and can be mathematically described as:

$$\begin{aligned}\frac{dM_x(t)}{dt} &= -\frac{M_x(t)}{T_2} \\ \frac{dM_y(t)}{dt} &= -\frac{M_y(t)}{T_2}.\end{aligned} \tag{21}$$

An additional dephasing component comes from the field inhomogeneities and is described by the transverse relaxation time due to

field inhomogeneities (T_2'), which, together with T_2, builds up the T_2^* effects. In particular, the effective transverse relaxation rate, equal to $1/T_2^*$ (R_2^*) is introduced. It is equal to the sum of the intrinsic transverse relaxation rate, equal to $1/T_2$ (R_2) and the transverse relaxation rate due to field inhomogeneities, equal to $1/T_2'$ (R_2') ($R_2^* = R_2 + R_2'$). The origin of this dephasing contributions and their relation to MRI are discussed in the following chapters.
Both T_1 and T_2 are material specific, and are responsible for the tissue contrast visible in MRI.

Bloch equation

The Bloch equations (Bloch et al., 1946) give the full dynamics of the magnetization, and combine the equations for relaxation (Eq. 20 and 21) with the equation of motion of the magnetization (Eq. 11):

$$\begin{aligned}
\frac{dM_x(t)}{dt} &= \gamma \left(\mathbf{M} \times \mathbf{B_{eff}}\right)_x - \frac{M_x(t)}{T_2} \\
\frac{dM_y(t)}{dt} &= \gamma \left(\mathbf{M} \times \mathbf{B_{eff}}\right)_y - \frac{M_y(t)}{T_2} \\
\frac{dM_z(t)}{dt} &= \gamma \left(\mathbf{M} \times \mathbf{B_{eff}}\right)_z - \frac{M_z(t) - M_0}{T_1}.
\end{aligned} \tag{22}$$

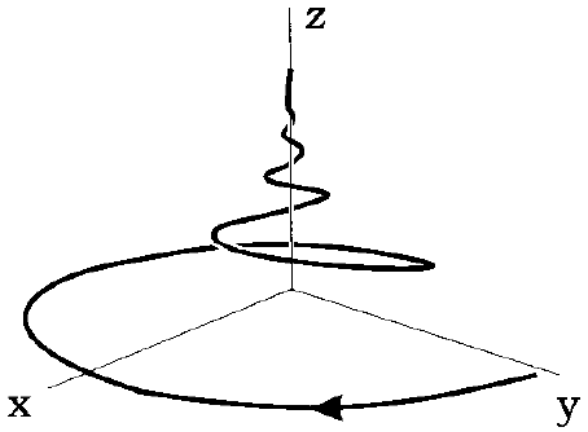

Figure 2: Relaxation of the magnetization vector in the laboratory frame of reference. The magnetization was initially tipped to the y axis and relaxes gradually to the equilibrium position (along the z axis). Picture from (Haacke et al., 1999).

Solutions to the Bloch equations

In the case of a static field, i. e., $\mathbf{B_{eff}} = B_0\hat{z}$, the solution to the Bloch equation reads:

$$\begin{aligned}
M_x(t) &= e^{-t/T_2}\left(M_x(0)\cos(\omega_0 t) + M_y(0)\sin(\omega_0 t)\right) \\
M_y(t) &= e^{-t/T_2}\left(M_y(0)\cos(\omega_0 t) - M_x(0)\sin(\omega_0 t)\right) \\
M_z(t) &= M_z(0)e^{-t/T_1} + M_0\left(1 - e^{-t/T_1}\right)
\end{aligned} \tag{23}$$

and the asymptotic solutions are:

$$M_x(t \to \infty) = M_y(t \to \infty) = 0, \quad M_z(t \to \infty) = M_0. \tag{24}$$

A graphical representation of the trajectory of the magnetization vector can be found in Fig. 2. The longitudinal component is restored, i. e., aligns back to the z axis, while the transversal components decay to zero with time.

2.2 PRINCIPLES OF MAGNETIC RESONANCE IMAGING

The rotational trajectory of the magnetization during its relaxation, as described by the Bloch equation (Eq. 22), creates a time-varying magnetic field that induces a voltage in a receiving coil (Faraday's law). The electromotive force ($\mathcal{E}$) induced in the receiveing coil is equal to the rate of change of the magnetic flux (Φ_M):

$$\begin{aligned}\mathcal{E} &= -\frac{d\Phi_M(t)}{dt} \\ &= -\int_{\text{sample}} \frac{d}{dt}\mathbf{M}(\mathbf{r},t)\cdot\mathbf{B}^{\mathbf{receive}}(\mathbf{r})d\mathbf{r}\end{aligned} \tag{25}$$

where $\mathbf{B}^{\mathbf{receive}}$ is the magnetic field induced by the unit current coil and the integral is carried over the whole sample volume. A Fourier transform of the signal induced in the coil allows the reconstruction of the imaged object.

2.2.1 *The Magnetic Field Gradients*

Since the precession frequency is proportional to the local magnetic field (Eq. 8), spatial changes in the field give rise to changes in frequency. Intuitively, if such spatial changes are controlled, a certain frequency is specific to a certain spatial position and spatial encoding is possible. A variation of magnetic field can be induced by magnetic field gradients.

A gradient can be defined as a vectorial quantity:

$$\mathbf{G} = G_x\hat{x} + G_y\hat{y} + G_z\hat{z}. \tag{26}$$

If the external magnetic field is described by $\mathbf{B}(\mathbf{r},t) = \mathbf{B_0} + [G\cdot\mathbf{r}]\,\hat{z}$, then the magnetization precesses around the z axis with the spatially varying angular velocity:

$$\boldsymbol{\omega} = -\gamma\mathbf{B} = -\gamma\,(\mathbf{B_0} + G\cdot\mathbf{r})\,\hat{z}. \tag{27}$$

Plugging Eq. 27 into Eq. 22 and ignoring relaxation effects, the Bloch equation takes the form:

$$\frac{d\mathbf{M}(\mathbf{r},t)}{dt} = -\gamma\,(\mathbf{B_0} + G\cdot\mathbf{r})\times\mathbf{M}(\mathbf{r},t) \tag{28}$$

Defining $M_\perp(\mathbf{r},t) = M_x(\mathbf{r},t) + iM_y(\mathbf{r},t)$, the solution to Eq. 28 can be written as:

$$M_\perp(\mathbf{r},t) = M_\perp(\mathbf{r},0)e^{-i\gamma Bt} = M_\perp(\mathbf{r},0)e^{-i\gamma(B_0+G\cdot\mathbf{r})t} \tag{29}$$

The signal S is proportional to the voltage induced in the coil and hence is an integration of the time derivative of the magnetization (Eq. 25):

$$\begin{aligned} S(t) &\approx \int_{\text{sample}} \frac{d}{dt}\mathbf{M}(\mathbf{r},t)\cdot\mathbf{B}^{\mathbf{receive}}(\mathbf{r})d\mathbf{r} \\ &\approx \int_{\text{sample}} \frac{d}{dt}\mathbf{M}_{\perp}(\mathbf{r},t)\cdot\boldsymbol{\Theta}(\mathbf{r})d\mathbf{r} \end{aligned} \tag{30}$$

where $\boldsymbol{\Theta}$ is the coil sensitivity, which depends on $\mathbf{B}^{\mathbf{receive}}$ (Seo et al., 2014). Substituting Eq. 29 into Eq. 30 and solving the time derivative, Eq. 30 takes the form:

$$\begin{aligned} &S(t) \approx \\ &-\int_{\text{sample}} i\gamma\left(B_0+\int_0^t G(t')\cdot\mathbf{r}dt'\right)M_{\perp}(\mathbf{r},0)e^{-i\gamma\left(B_0+\int_0^t G(t')\cdot\mathbf{r}dt'\right)t}\cdot\boldsymbol{\Theta}(\mathbf{r})d\mathbf{r} \\ &\approx -i\gamma B_0\int_{\text{sample}} M_{\perp}(\mathbf{r},0)e^{-i\gamma\int_0^t G(t')\cdot\mathbf{r}dt'}\cdot\boldsymbol{\Theta}(\mathbf{r})d\mathbf{r} \end{aligned} \tag{31}$$

where the last step followed the assumption of $|G\cdot\mathbf{r}| \ll B_0$. Introducing the wave vector $\mathbf{k}(t)$,

$$\mathbf{k}(t) = \frac{\gamma}{2\pi}\int_0^t G(t')\cdot\mathbf{r}dt', \tag{32}$$

and denoting $\mathbf{m}(\mathbf{r}) = M_{\perp}(\mathbf{r},0)\boldsymbol{\Theta}(\mathbf{r})$ allows rewriting Eq. 31 as:

$$S(\mathbf{k}(t)) \approx \int_{\text{sample}} \mathbf{m}(\mathbf{r})e^{-2\pi i\mathbf{k}(t)\cdot\mathbf{r}}d\mathbf{r} \tag{33}$$

whose inverse Fourier transform recovers the magnetization-dependent value $\mathbf{m}(\mathbf{r})$. Explicitly,

$$\mathbf{m}(\mathbf{r}) \approx \int_{k_x}\int_{k_y}\int_{k_z} S(k_x,k_y,k_z)e^{2\pi i(k_x x+k_y y+k_z z)}dk_x dk_y dk_z. \tag{34}$$

In case of a time constant gradient, the wave vector takes the form:

$$\mathbf{k}(t) = \frac{\gamma G t}{2\pi}. \tag{35}$$

The phase accumulated by the magnetization vector due to the local Larmor frequency, $\Delta\phi(\mathbf{r},t)$, can be expressed in terms of $\mathbf{k}(t)$:

$$\Delta\phi(\mathbf{r},t) = \Delta\omega(\mathbf{r})t = \gamma G\cdot\mathbf{r}t = 2\pi\mathbf{k}\cdot\mathbf{r}. \tag{36}$$

2.2.2 *Slice Selection*

A magnetic field gradient can be applied during the RF pulse to achieve slice selection. If, for example, an axial slice is acquired, the

gradient along the z direction is manipulated in order to achieve the desired slice thickness. For coronal and sagittal slices, gradients along x and y axes need to be employed.
The slice thickness (d) is related to the slice-selection gradient (G_s) in the following way:

$$d = \frac{\Delta\omega}{\gamma G_s} \tag{37}$$

where $\Delta\omega$ is the bandwidth of the RF pulse. The position of the slice is determined by the carrier frequency of the RF pulse.
The effect of G_s is a gradually changing resonance frequency along the z axis according to $\omega_0(z) = \gamma G z$.

In the ideal case, off-resonance effects are only due to the gradient and there is no phase dispersion. In order to achieve a rectangular slice profile, a sinc RF pulse is applied (whose Fourier transform is a rect function) together with the slice-selection gradient (Fig. 3).

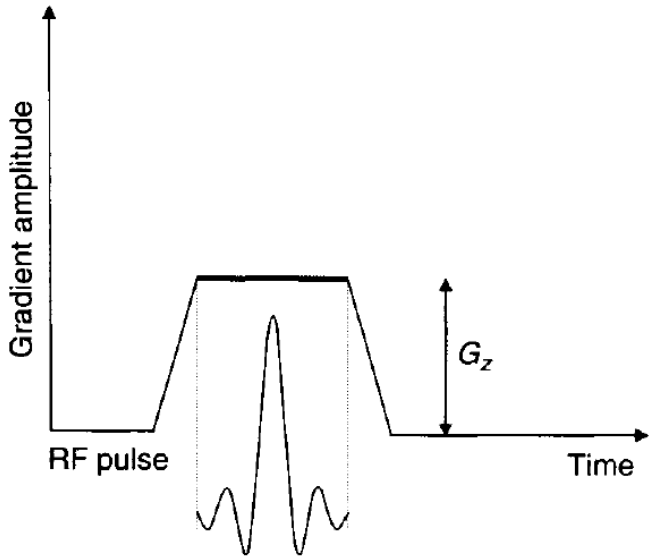

Figure 3: The constant gradient along the z axis is applied together with the RF pulse in order to achieve selection of an axial slice. Picture from (Bernstein et al., 2004).

2.2.3 *In-Plane Spatial Encoding*

The gradients along the x and y axes can be employed to achieve spatial encoding.

Frequency encoding

The readout or frequency encoding gradient (G_R) is a linear gradient along the x axis. It is switched on during signal acquisition in order to have a linear dependence between the frequency and the position:

$$\omega(x) = \gamma x G_R. \tag{38}$$

Phase encoding

The phase encoding gradient (G_P) modulates the phases of the isochromats along the y direction. It is switched on for a short period of time and induces position-dependent phases according to:

$$\phi(y) = \gamma \int_0^t y \cdot G_P(t')dt'. \tag{39}$$

Given that the signal measured during a MRI experiment is a sum of all the signals coming from the all the isochromats, the different phases add up and it is not possible to establish a one-to-one relationship with their positions. Therefore, the phase gradient is increased stepwise from $-G_P$ to $+G_P$ (each for an interval t_P) in order to have a different value for each sampled position. So, the nth-phase-encoding step is defined by:

$$\phi(y, n) = \phi_0 + n\gamma \int_0^{t_P} y \cdot G_P(t')dt' \tag{40}$$

and the position can be encoded through a Fourier transform.

Field of view

The field of views (FOVs) in the x and y direction are proportional ot the read and phase gradient, respectively. The FOV in the readout direction is given by:

$$FOV_x = \frac{\Delta\omega_{\text{receive}}}{\gamma G_R} \tag{41}$$

where $\Delta\omega_{\text{receive}}$ is the receiver bandwidth. For the FOV in the phase encoding direction the following relationship is valid:

$$FOV_y = \frac{1}{\gamma \Delta G_P t_P} \tag{42}$$

The voxel size in readout and phase encoding directions (Δx and Δy, respectively) can be calculated from the field of view, if the number of sampling points (N_x) and phase-encoding steps (N_y) are known:

$$\begin{aligned} \Delta x &= \frac{FOV_x}{N_x} = \frac{\Delta\omega_{\text{receive}}}{\gamma G_R N_x} \\ \Delta y &= \frac{FOV_y}{N_y} = \frac{1}{\gamma \Delta G_P t_P N_y} \end{aligned} \tag{43}$$

where it was made use of Eq. 41 and 42.

2.2.4 *The k-Space Representation*

Given that the NMR signal is related to the magnetization via a Fourier transformation (Eq. 34), and that the spatial encoding is achieved with frequency and phase modulation, the k-space concept represent a convenient tool for MRI (Twieg, 1983). In this view, image acquisition can be thought of as k-space sampling.

The k_x axis represents the frequency encoding, or read, axis, while the k_y axis is the phase encoding axis (Fig. 4). Since the readout and the phase encoding gradients modulate frequency and phase, respectively, they can be used to move around k-space. The area under a gradient lobe (that is, its amplitude time its duration) corresponds to distances in k-space.
When the readout gradient is switched on, a full k_x line in k-space is acquired. The phase encoding gradient does not need be switched on all the time, because the amount of phase accumulation depends on the total area of the gradients previously played out, regardless of the fact that their application is discontinuous or continuous (the phase is locked when the gradient is off). Therefore, gradient blips (i. e., gradients of short duration) are sometimes applied to increase k_y gradually from the acquisition of one k_x line to the next.

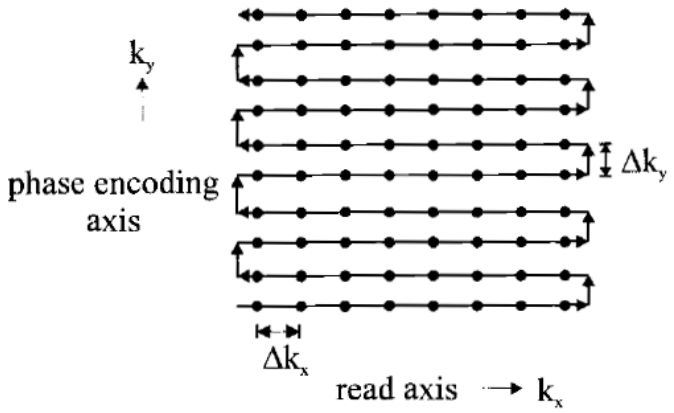

Figure 4: A schematic representation of sampling in k-space. k_x represents the read axis and k_y the phase encoding axis. Picture from (Haacke et al., 1999).

Properties of k*-space*

The extent of k-space (from $-k_{max}$ to $+k_{max}$) is related to the voxel size (Δx) in image space according to the relationship:

$$\Delta x = \frac{1}{2k_{max}}. \tag{44}$$

And the FOV is related to the sampling distance in k-space by an inverse relationship:

$$FOV = \frac{1}{\Delta k}. \tag{45}$$

The total number of data samples (N) in k-space equals the number of voxels in image space:

$$N = \frac{2k_{max}}{\Delta k} = \frac{FOV}{\Delta x}. \tag{46}$$

The points closer to the k-space center correspond to lower frequencies, i. e., the "bulk" of the image, while the points closer to the edges

of k-space correspond to higher frequencies, which represent the fine structures of the image.

An additional important property of k-space is its symmetry. Specifically, the Fourier transform of a real object is hermitian:

$$S(k_x, k_y, k_z) = S^*(-k_x, -k_y, -k_z). \tag{47}$$

This means that, in principle, only half of k-space is required to reconstruct the full image. In practice, this is not the case due to phase shifts and, consequently, only a portion of k-space is omitted in order to speed up the acquisition, and the k-space center is always sampled.

The point spread function

The point spread function (PSF) describes the response of an imaging system to a point signal source. It indicates the amount of blurring, that is, the contribution of neighbouring voxels to the signal intensity observed in a certain voxel. The PSF is, thus, a crucial quantity for the description of the true resolution of an MR image.
In the image space, it corresponds to the convolution of the smoothing function $w(x)$ with the object function $f(x)$, so that the smoothed function $h(x)$ is:

$$h(x) = w(x) \otimes f(x). \tag{48}$$

In k-space, the convolution corresponds to a simple multiplication:

$$H(k) = W(k)F(k), \tag{49}$$

where the capital letters denote the Fourier transform of the corresponding functions. The PSF is a windowing (or $rect$) function in k-space and a $sinc$ function in image space:

$$PSF(x) = \frac{\sin(2\pi k_{max} x)}{\pi x}. \tag{50}$$

The PSF, thus, decreases for higher values of k_{max}.

2.3 PULSE SEQUENCES

In general, an imaging sequence consists of the following elements: a RF excitation pulse, a slice selection gradient along z (followed by a rephasing gradient), a phase encoding gradient along y and a readout gradient along x.
In this simple case, the repetition time (T_R) corresponds to the time between one RF pulse and the next, and the echo time (T_E) the time of signal formation. In k-space, one line is acquired for each T_R, and the T_E is at $k_x = k_y = 0$. T_R and T_E are user-adjustable parameters and are important in determining the final contrast of the image (Fig. 5).

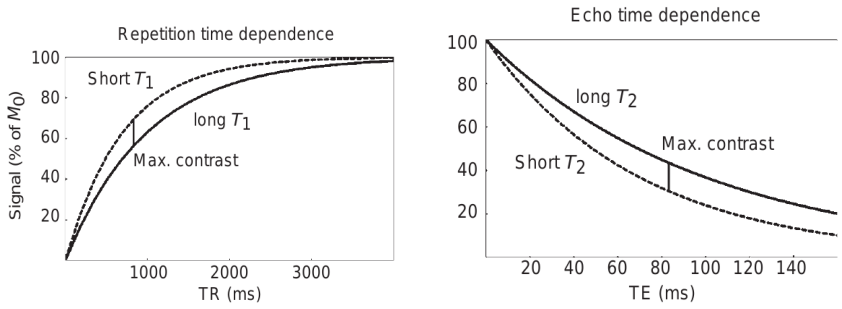

(a) (b)

Figure 5: Repetition (a) and echo time (b) dependence of the MR contrast between two tissue types. One tissue is characterized by long T_1 and T_2 (continuous line) and the other by short T_1 and T_2 (dashed line). The T_R allows adjusting the T_1 contrast, while the T_E the T_2 contrast. Adapted from (Buxton, 2009).

2.3.1 *Echo Formation*

There exist two main types of echoes: the spin echo and the gradient echo. Both of them are, actually, gradient echoes and differ only in the fact that spin echo includes a 180° RF pulse and frequency encoding gradients of the same polarity.

Gradient echo

For gradient echo, gradients along x are applied with different polarities. First, a negative gradient pulse is applied, which causes phase accumulation. Secondly, a positive gradient with an area twice as big as the previous negative lobe, is played out. The effect of the second frequency encoding gradient is to counterbalance the initial negative gradient in the first half (negative k_x values in k-space), and to readout the positive k_x values in the second one.

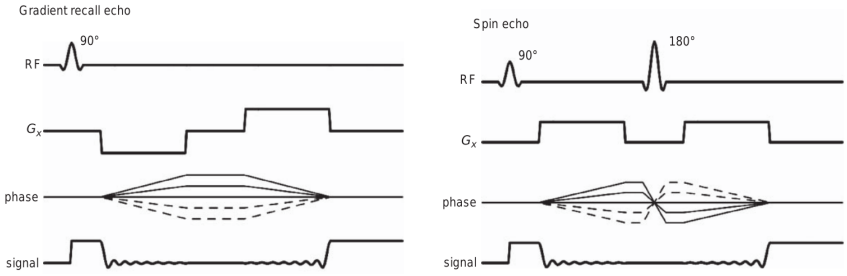

(a) (b)

Figure 6: Pulse diagrams for gradient echo (a) and spin echo (b). Both echoes originate from a gradient echo effect, with the only difference that spin echo employes a 180° RF pulse and, thus, the two lobes of the gradient G_x have the same polarity. Picture taken from (Buxton, 2009).

Spin echo

The spin echo originates from the fact that the 180° RF pulse rephases static field effects due to field inhomogeneities (T_2' effects). When

the spins are flipped, their trajectories are reversed and the accumulated phase goes back to zero, creating an echo of the original free-induction decay (FID). The echo is not as strong as the original FID signal due to the non-static field effects (T_2 effects).

A graphical representation of the two echo formations can be found in Fig. 6.

2.3.2 *Echo-planar imaging*

For functional magnetic resonance imaging (fMRI) applications, a quick acquisition is fundamental. The workhorse for signal readout is EPI (Mansfield, 1977), in which the full k-space is acquired after each RF pulse (in case of single-shot), instead of just one line.
The standard sampling pattern for EPI is cartesian and serpentine-like, such that lines are acquired with alternating positive and negative readout gradients. The steps in the k_y direction are achieved by small phase encoding gradient pulses, called blips. The full diagram of the sequence can be observed in Fig. 7.
The advantages of this technique are that it provides high sensitivity and can acquire whole brain volumes quickly (typically in 1-3 s).

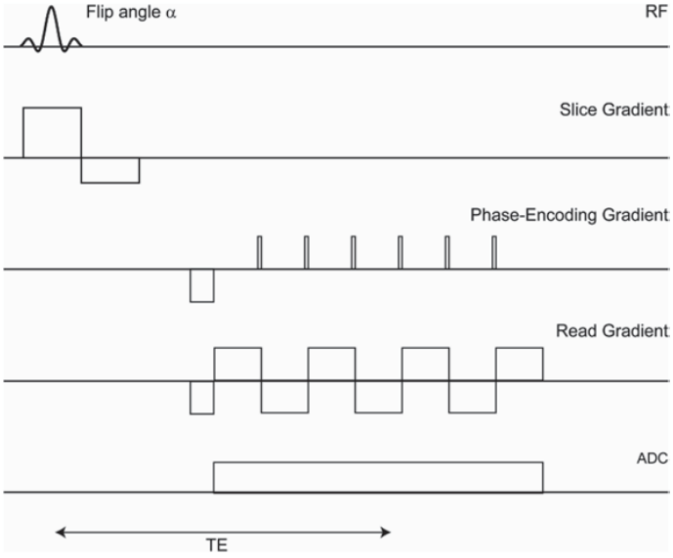

Figure 7: Echo-planar imaging. Picture from (Uludag et al., 2015).

Limitations

Several limitations of the technique are related to the acquisition time (T_A). First of all, effective transverse relaxation time (T_2^*) decay, in case of gradient recalled echo (GRE)-EPI, limits the T_A window to 100 ms or less (for $B_0 \geqslant 3$ T) before the signal decays away.
Secondly, the presence of susceptibility gradients creates artefacts. An additional linear gradient along y rescales the image and changes the actual T_E; a gradient along x shears the image and a gradient along z dephases the signal, creating signal voids (Uludag et al., 2015).
Distortions are reduced by decreasing the acquisition time. Apart

from strong gradients (which cannot be indefinitely strong, primarily due to physiological limits), parallel imaging can be used. Parallel imaging requires multichannel receiver coils and can speed up the acquisition by a factor of 3-4. It comes at a cost of signal-to-noise ratio (SNR), because the so called g-factor (geometry-factor) is introduced as well as a noise penalty of $\sqrt{R}$, where R is the acceleration factor. The $\sqrt{R}$ penalty is mostly affecting thermal noise and for many physiological noise-dominated fMRI application, this reduction in SNR is negligible.
The ratio of thermal to physiological noise in the image, however, can change: for high resolution, stronger gradient pulses need to be employed, and the consequent increase in acquisition bandwidth increases the amount of thermal noise in the voxel (Triantafyllou et al., 2005).

Other fast readout techniques travel around k-space following different trajectories; for example, spiral and radial patterns can be employed. Multiplexed and 3D acquisitions can be also beneficial for reducing T_A.

Finally, the scanner hardware plays a crucial role: for achieving high resolution in short time, strong gradients and quick gradient switching are required. Additionally, to benefit from parallel imaging techniques, multichannel receiver coils are necessary.

2.4 MRI DEPENDENCY ON EXTERNAL FIELD STRENGTH

Increasing the static magnetic field B_0 comes at advantages and disadvantages for MRI, leading to a net positive or negative effect, depending on the technique and application considered. The decrease in spatial scale of field inhomogeneities and the shortening of T_2 represent a problem for functional applications. Nevertheless, fMRI generally benefits from higher field strengths, but often several modification, even substantial, are necessary.

2.4.1 *Differences Between 7 T and Lower Fields*

With the transition from lower to higher fields, there are some relevant changes for MRI (van der Zwaag et al., 2015):

- The magnetization increases linearly, i. e., $M_0 \propto B_0$ (see Eq. 6 and 7).
- The wavelength of resonance radiofrequency becomes shorter ($\sim$ 30 cm in tissue at 3 T, $\sim$ 13 cm in tissue at 7 T).
- The resonance frequency increases (128 MHz at 3 T, 300 MHz at 7 T).
- The magnetic field susceptibility effects increase $\propto B_0$.

- T_1 becomes longer.
- T_2 and T_2^* become shorter ($T_2 \propto B_0^{-1}$).

2.4.2 *Advantages and Disadvantages for MRI*

The linear increase in M_0 with field strength is always advantageous because it means a linear increase in SNR, which can be traded for higher resolution.
The shorter wavelength of resonance radiofrequency can be an advantage because allows for better spatial differentiation for parallel reception and transmission, but often this B_1 inhomogeneity represents a problem because delivers an inhomogeneous tissue contrast (van der Zwaag et al., 2015).
The increased resonance frequency creates a higher $\mathcal{E}$ (Eq. 25), but the RF power needed for generating RF pulses increases too (as B_0^2), and therefore specific absorption rate (SAR) $\propto B_0^2$.
The increased in susceptibility effects has a twofold consequence in fMRI: on one hand, it increases the functional contrast because ΔR_2^* increases supralinearly with B_0 ($\sim\propto B_0^{1-1.5}$); on the other hand, the susceptibility-induced distortions in EPI increase accordingly (see Section 2.3.2).

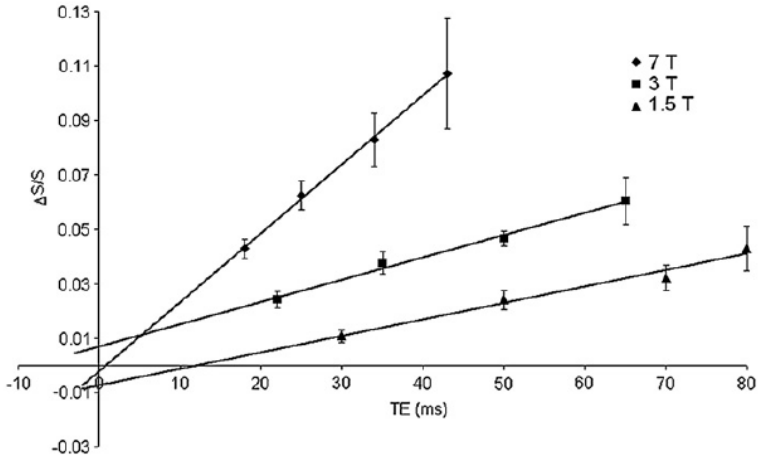

Figure 8: Functional signal changes (GRE-EPI) as a function of T_E at three different field strength for a voxel size of $1 \times 1 \times 3$ mm^3. The advantage of 7 T with respect to the lower field strengths is apparent. Picture from (van der Zwaag et al., 2009).

Finally, the changes in relaxation times are advantageous, in that they increase the corresponding contrasts. However, some drawbacks are associated to them: due to the longer T_1, higher T_Rs are needed to avoid inflow effects; the shorter T_2 and T_2^* make the available acquisition window shorter, and the maximal sensitivity is achieved for shorter T_Es, which means that stronger gradients are needed (van der Zwaag et al., 2015).

In conclusion, moving towards higher field has proven beneficial for several MRI techniques, including fMRI (see Fig. 8), and has allowed imaging at higher resolution.

3

IMAGING PHYSIOLOGICAL VARIABLES

The human brain at rest consumes up to 20% of the oxygen needed by the whole body, although it accounts for only 2% of the total body mass. Given that the brain lacks a way of storing energy over long periods of time, the energy supply has to be controlled on a fine spatial and temporal scale.

Early experiments performed by the physiologist Angelo Mosso with a plethysmograph (which measures blood flow using brain pulsations) and a "human circulation balance" (Fig. 9) indicated that blood could redistribute during cognitive states, resulting in an increase in brain blood flow, as compared with rest (Mosso, 1884, 1881).

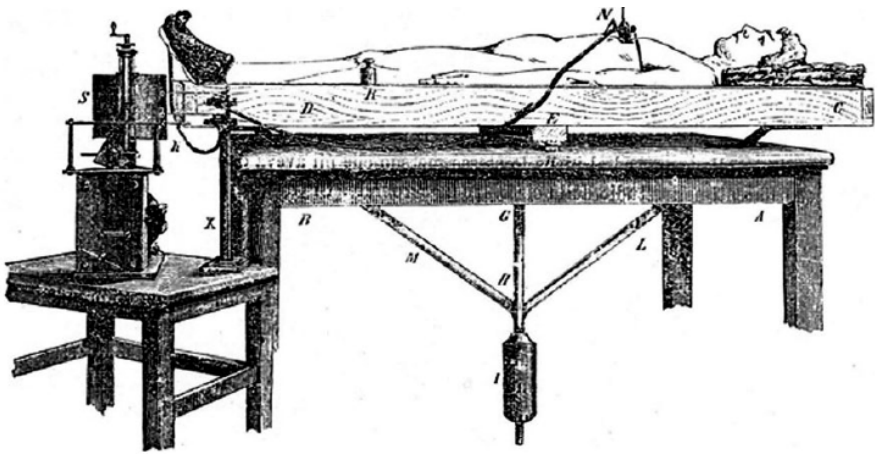

Figure 9: The human circulation balance in a drawing by Angelo Mosso (Mosso, 1884). A and B = wooden table with three apertures on its top; C and D = tilting bed; E = pivot with steel knife fulcrum; G and H = 1 m long iron rod bearing the counterweight; I = cast iron counterweight with screw regulation; M and L = two iron stiffening bars; N = pneumatic pneumograph; R = equilibrating weight; S = kymograph; X = vertical stand for graphic transducers. Picture and description taken from (Sandrone et al., 2014).

The fact that neuronal activity drives an increase in blood flow is at the very basis of fMRI. This phenomenon is called *neurovascular coupling* and the mechanisms behind it have been studied extensively but only partially understood. This makes the fMRI signal an indirect measure of neuronal activity; it is sensitive to physiological changes in the brain vascular tree, such as changes in oxygenation level, in cerebral blood volume (CBV) or/and in cerebral blood flow (CBF), which can or cannot be driven by neuronal activity.

The way these physiological changes are coupled to neuronal activity and how they are related to magnetic properties, detectable by MR-scanners, is reviewed in this chapter. Section 3.1 reviews the basics of brain metabolism and neurovascular coupling; Section 3.2 introduces the mechanisms behind the blood oxygen level dependent (BOLD) effect; Section 3.3 gives an overview of other imaging techniques used for functional imaging, based on CBV and CBF changes.

3.1 THE NEUROVASCULAR COUPLING

3.1.1 *Neural Activity*

The basic unit for information processing and transmission is the neuron. Its main constituents are the dendrites, where signals from other neurons are received and integrated, the soma, i. e., the cell body, and the axon, an elongated structure (up to 1 m long) that is responsible for information transmission to other neuronal cells (Fig. 10).

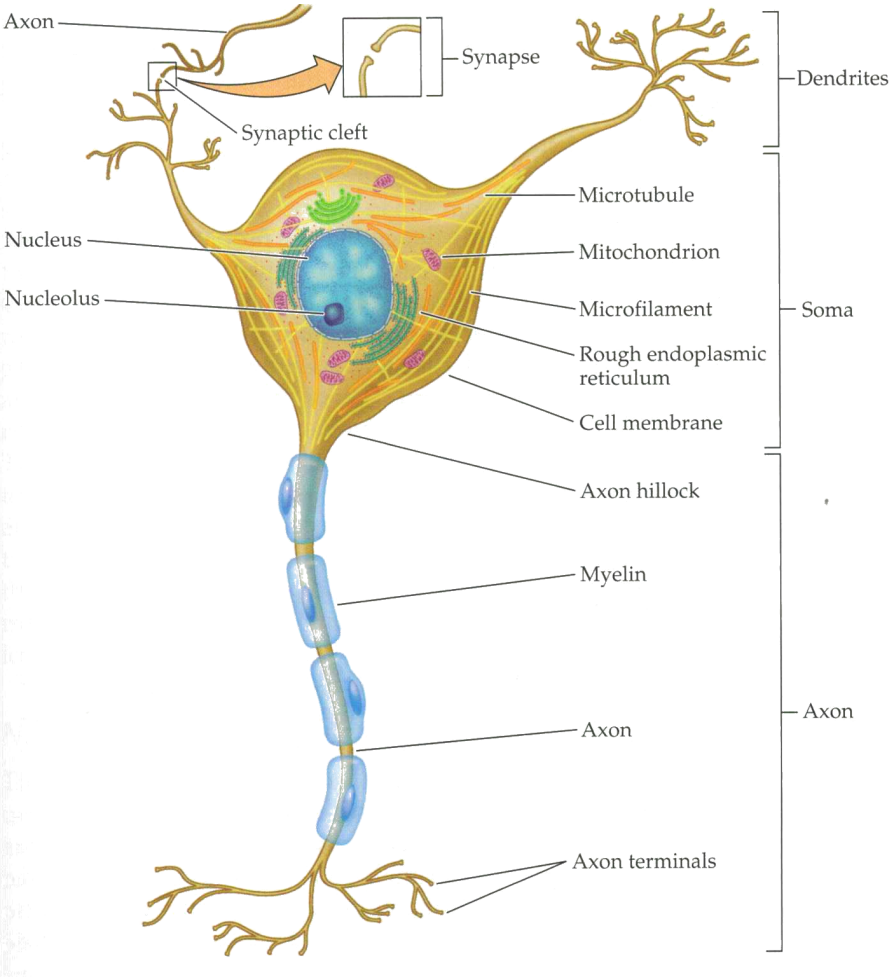

Figure 10: The neuron. Picture taken from (Huettel et al., 2004).

The cell membrane, a lipid bilayer, maintains a resting potential (of about -60 mV) and a concentration gradient between the internal and external environments. For neurons at rest, the concentration of K^+ is higher inside the membrane, while the concentration of Na^+, Ca^{2+} and Cl^- is higher in the extracellular space. The resting potential can be modified by selective opening of ion channels, which is elicited by neurotransmitter release, and is restored to the resting value by the sodium-potassium pump.

If the activity of a single neuron is taken into account, the information input starts at the dendrites. For example, when the excitatory neurotransmitter glutamate (Glu) is released, an influx of Na^+ and Ca^{2+} ions through the membrane takes place. This originates a cascade depolarization that propagates down to the presynaptic terminals at the end of the axon and is called action potential (AP). There, Ca^{2+} ion channels are opened, which in turn causes release of Glu into the synapse. The postsynaptic membrane will react to the release of Glu by selective opening of ion channels. The resulting change of potential is called excitatory post-synaptic potential (EPSP).

However, if the postsynaptic membrane is hyperpolarized, meaning that the potential is more negative due to Cl^- influx and/or K^+ outflux, an AP will not take place and the change of potential is called inhibitory post-synaptic potential (IPSP). The most common inhibitory neurotransmitter is gamma-aminobutyric acid (GABA).

Due to the fact that each neuron has many dendrites, the amount and timing of incoming EPSPs and IPSPs determine whether an action potential will take place or not. The action potential, thus, reflects the output activity of the neuron.

In essence, there are two main electrical events taking place at the neuronal level: the spiking activity (the AP) and the synaptic activity. Given that these two activities happen at different temporal scales (spikes have a duration of about 1 ms and postsynaptic potentials of up to 100 ms), they can be recorded and separated by filtering. The high-pass filtered signal yields spiking activity, while the low-pass filtered signal yields the local field potential (LFP), which reflects the integrated postsynaptic activity. It has been shown that the fMRI signal mainly reflects LFP rather than AP, i. e., the input to a certain brain area and the corresponding integrative processes (Logothetis et al., 2001).

3.1.2 *Brain Energy Metabolism*

The sodium-potassium pump needs adenosine triphosphate (ATP) to stabilize the potential across the membrane. It forces three Na^+ ions out of the cell and two K^+ ions inside the cell, per unit of ATP, which is consequently converted to adenosine diphosphate (ADP). ATP is also used for other aspects of brain physiology, but restoring the mem-

brane potential is estimated to account for about 75% of the total ATP usage, which is on the order of 30 to 50 μmol/g/min in the human brain (Huettel et al., 2004).

The ATP is produced from glucose via a process called glycolysis. Glucose is first transported from the capillaries to the neurons, where it can be broken down to form 2 ATP. However, under aerobic conditions, 18 times more ATP can be produced. This is due to the fact that pyruvate enters the tricarboxylic acid (TCA) cycle, which produces 2 more ATP, and oxidative phosphorylation, which delivers 34 more ATP.

A more recent view involves the role of astrocytes, a type of glial cell surrounding neurons, in the production of ATP. In this so-called astrocyte-neuron lactate shuttle hypothesis, the glucose is transported to the astrocytes, where it undergoes glycolysis; the resulting lactate is then transported to the neurons, where the oxidative metabolism takes place (Pellerin and Magistretti, 1994).

Given that the brain lacks a sensible energy storage, blood flow is responsible for its energy supply and is therefore regulated on a fine scale. The delivery of glucose and oxygen to the neurons, as well as the transport of waste carbon dioxide, happen at the capillar level. Capillaries are the finest vessels in the brain vasculature (5 to 10 μm) and any cell in the body was estimated to be at most 50 μm apart from the nearest capillary (Huettel et al., 2004). More consideration on the brain vasculature can be found in section 4.1.

3.1.3 *Functional Hyperemia*

In general, a local increase in brain activity will be accompanied by an increase in CBF, cerebral metabolic rate of glucose consumption (CMR_{glc}) and cerebral metabolic rate of oxygen consumption ($CMRO_2$) (more on that in section 3.2). In turn, blood velocity and CBV will also increase. However, for brief stimuli, the increase in CBF and CMR_{glc} may by far exceed that of $CMRO_2$ (Fig. 11a) (Raichle, 2001). This reflects the fact that glucose is being broken down anaerobically. This local increase in glycolysis could be explained by the fact that, after an EPSP, the released Glu needs to be cleared from the synapse, and hence it is taken up by the astrocytes, where it is converted to glutamine (Gln) and recycled (Fig. 11b,c). The conversion from Glu to Gln needs energy, which is produced by glycolysis of blood-borne glucose (Shulman et al., 2001). This resulting increase in oxygen availability can be detected by blood-oxygen sensitive fMRI (see section 3.2).

The blood flow can be controlled at different scales of the vascular tree: at the capillary, at the arteriolar and at the arterial level. In the context of mapping brain activity, the functional changes at the capillary and arteriolar site are the most relevant, due to their proximity

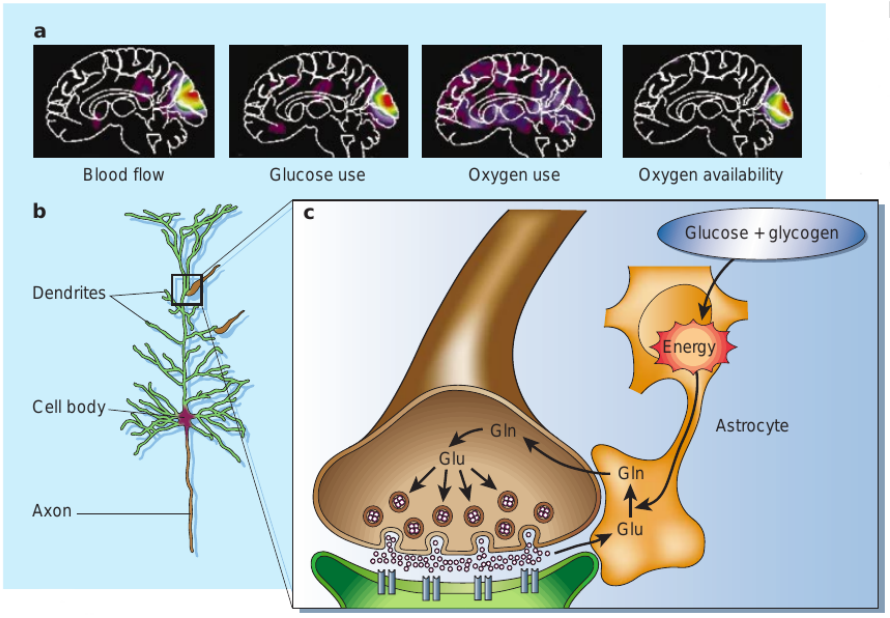

Figure 11: The neural basis of fMRI. (a) Changes in blood flow, glucose use, oxygen use and oxygen availability in a human brain following visual stimulation (checkerboard), measured with PET. (b) The metabolic changes are elicited by electric potentials at the dendrites of neurons. (c) The role of astrocytes in converting Glu to Gln. Picture taken from (Raichle, 2001).

to the site of metabolic changes. It is therefore important to consider and characterize the concomitant changes happening upstream (arteries) and downstream (veins) with respect to the capillary bed, which may represent a confound to the variable of interest.

Blood flow regulation at the arterial level

Arterial and arteriolar endothelium is wrapped with smooth muscle cells, which are capable of dilating and constricting. The smooth muscle cell tone regulation is driven by the polarization of the membrane, which depends on the interaction of K^+ and Ca^{2+} channels. There are many different vasodilating and vasoconstricting substances of neuronal, astrocytic and endothelial origin. In addition, substances carried by blood can also have a vasodilating effect. An example of this is CO_2, which induces acidosis (decreased pH) and hyperpolarizes the membrane, resulting in dilation of the vessel.

The exact interplay among different signaling pathways is still matter of debate. It has been proposed that the neuronal and astrocytic signaling pathways may take place on different timescales, given that the neuronal pathway is more direct and faster than the astrocyte-mediated one (Cauli, 2010). In the neuronal hypothesis, nitric oxide (NO) was initially considered to be responsible for controlling the vascular tone (Iadecola, 1993), but later discarded as the principal cause of vasodilation. Perivascular nerves have then been suggested to modulate vascular resistance via release of vasoactive substances (Hamel, 2006). In support of the astrocytic hypothesis is the

convenient position of astrocytes (between vessels and neurons) and the fact that they can express a large number of receptors, can elicit Ca^{2+} waves and can release vasoactive substances (Iadecola and Nedergaard, 2007).

Blood flow regulation at the capillary level

In addition to the arterial dilation, it has been shown that capillaries are also capable of actively dilating. Unlike arterial walls, they are not equipped with smooth muscle, but they are surrounded by some isolated cells, called pericytes, that are capable of regulating capillary diameter. Hall et al. found that pericytes are the first to respond upon electrical whisker stimulation in rats. According to their findings, capillaries dilate approximately 1.4 s before arterioles, and account for the 84% of CBF increase. The explanation for this effect would be the fact that capillaries are the vascular structure more proximal to neurons, and hence the first to sense neuronal signaling. It is not clear, though, whether arteriolar dilation is elicited by the membrane hyperpolarization signal propagating from the capillaries, or rather from vasoactive messengers that reach the arterioles at later times. Regardless of the mechanism behind the onset of arterial dilation, the study showed that capillaries play a crucial role in regulating blood flow (Hall et al., 2014).

3.2 THE BOLD CONTRAST

3.2.1 *The BOLD Phenomenon*

When an object is placed in a magnetic field, its magnetization changes by a certain amount. This amount is proportional to the specific magnetic susceptibility, χ, of the object. It is related to the object magnetization, $\mathbf{M}$, and the external magnetic field strength, $\mathbf{H}$, via the following relationship:

$$\mathbf{M} = \chi \mathbf{H}, \tag{51}$$

where $\mathbf{M}$ and $\mathbf{H}$ ($\mathbf{H} = \mathbf{B_0}/\mu$, with μ being the magnetic constant) are in units of A/m and χ is unitless.

Thus, local inhomogeneities in susceptibility, such as in the proximity of interfaces between different materials or tissues, will originate local magnetic field gradients.

Diamagnetic materials have $\chi < 0$, while paramagnetic, superparamagnetic and ferromagnetic materials have $\chi > 0$.

Biological tissues are generally weakly diamagnetic, but some components of body fluids, such as blood haemoglobin (Hb), not necessarily. Hb can be found in the brain in two states: oxygenated and deoxygenated. Deoxygenated haemoglobin, or deoxy-haemoglobin (dHb) is paramagnetic, but becomes diamagnetic when bound to oxygen.

Such state-dependent magnetic properties have an effect on the susceptibility difference between the intravascular (IV) and extravascular

(EV) compartments. When the blood is fully oxygenated, its susceptibilty is similar to the one of the surrounding tissue, so that the magnetic field gradient is minimal. When the concentration of deoxygenated haemoglobin increases, the gradient increases accordingly, following a linear relationship (Weisskoff and Kiihne, 1992). This effect can be seen as a signal decrease in T_2^*-weighted images. More deoxy-haemoglobin will, indeed, accelerate spin dephasing and reduce the effective T_2^*, leading to signal suppression.

The field offset (ΔB) within a voxel depends on the total amount of venous blood within that voxel. The field offset can be described in terms of frequency offset ($\Delta\omega$), which is directly proportional to ΔB (via $\omega = \gamma B$), and can be derived for the intravascular and extravascular compartments.

In the IV space, water molecules quickly exchange between red blood cells and plasma (the residence time of water in red blood cells is approximately 5 ms) under dynamic averaging conditions (Mohamed, 2006). All molecules experience a similar dynamic averaging and hence blood T_2 reduces as the dHb level increases. The frequency offset in the IV space, $\Delta\omega_{in}$, follows Eq. 52:

$$\Delta\omega_{in} = 2\pi\Delta\chi_0(1-Y)\omega_0\left(\cos^2\theta - 1/3\right) \tag{52}$$

where $\Delta\chi_0$ is the susceptibility difference between fully oxygenated and fully deoxygenated blood (hence haematocrit-dependent), Y is the oxygenation fraction in venous blood, ω_0 is the Larmor frequency corresponding to the applied magnetic field, θ is the angle between $\mathbf{B_0}$ and the vessel (see Fig. 12).

The frequency offset in the EV space, $\Delta\omega_{out}$, follows Eq. 53:

$$\Delta\omega_{out} = 2\pi\Delta\chi_0(1-Y)\omega_0\left(\frac{a}{r}\right)^2\sin^2\theta\cos(2\phi) \tag{53}$$

where a is the radius of the vessel, r the radial distance from the center of the vessel and ϕ is the angle between r and the plane formed by $\mathbf{B_0}$ and the vessel axis (see Fig. 12).

For $r = a$ in Eq. 53, i.e., at the vessel lumen, the frequency offset depends on the oxygenation level of the vessel and not on the vessel dimension.

For $r > a$, the magnitude of the frequency offset in Eq. 53 depends on the square of the vessel radius. For example, the frequency offset observed at $r = 15$ μm for a vessel with radius $a = 3$ μm is the same as the one observed at $r = 150$ μm for a vessel with radius $a = 30$ μm, meaning that the spatial spread of frequency shift is highly vessel-size dependent (Mohamed, 2006). In turn, whether a water molecule in the EV space experiences dynamic averaging or static dephasing during a T_E, depends on the size of the surrounding venous vessels (Fig. 13).

Finally, the direct dependency of $\Delta\omega_{out}$ on $\sin^2\theta$ implies that no field

distortion is produced in the surrounding of vessels parallel to $\mathbf{B_0}$ ($\theta = 0$) and is maximal for vessels perpendicular to $\mathbf{B_0}$ ($\theta = \pi$).

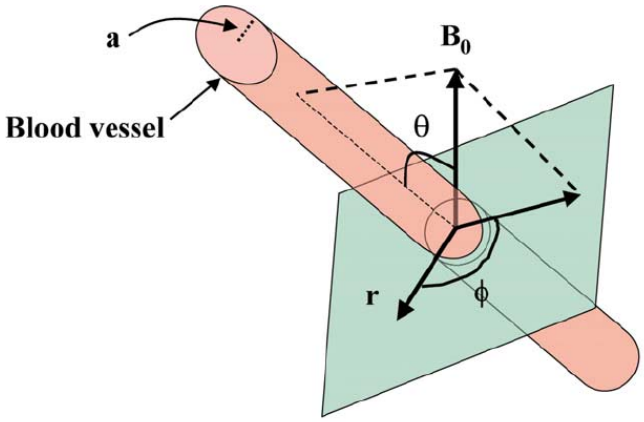

$$\Delta\omega_{in} = 2\pi\,\Delta\chi_0\,(1 - Y)\,\omega_0\,(\cos^2\theta - 1/3)$$

$$\Delta\omega_{out} = 2\pi\,\Delta\chi_0\,(1 - Y)\,\omega_0\,(a/r)^2\,(\sin^2\theta)\,(\cos 2\phi)$$

Figure 12: Intravascular ($\Delta\omega_{in}$) and extravascular ($\Delta\omega_{out}$) frequency shift induced by a change in dHb level within a dHb-containing blood vessel. Picture taken from (Kim and Ugurbil, 2003).

Upon brain activation, CBV, CBF and $CMRO_2$ increase. The complex interplay between those quantities (which is stimulus, subject, brain area, and time-of-the-day specific) leads to a net drop in oxygen extraction fraction (OEF) and, thus, [dHb] in the capillary and postcapillary compartments decreases, due to the fact that the cerebral blood flow increases relatively more than cerebral blood volume and cerebral metabolic rate of oxygen. The consequent frequency shifts around venous vessels allows the detection of a signal increase in T_2^*- and T_2-weighted images. This effect is the so-called BOLD effect, and was first reported by Seiji Ogawa in 1990 in rats (Ogawa et al., 1990).

3.2.2 *Pulse Sequences for BOLD Mapping*

Since its discovery, the BOLD effect has been largely employed for looking into brain function. However, changes in oxygenation, although in many cases coupled to brain activity, are not a direct measure of it. As mentioned earlier, decreases in [dHb] are to be expected in dHb-containing compartments, i.e., mainly capillary and postcapillary and, to some extent, arteriolar (see Section 4.1.3).
The amount of blood dHb depends primarily on three parameters: CBF, CBV and $CMRO_2$. Mapping each of those parameters separately is discussed in Sections 3.3 and 6.1.1. In the following, sequences sensitive to oxygenation changes are considered.

COMPARTMENT	T_1	T_2	T_2^*
Arterial blood water	1664 ms	96-122 ms	49-55 ms
Venous blood water	1584 ms	23-35 ms	15-22 ms
Gray matter	1209 ms	71 ms	42-66 ms
White Matter	758 ms	81 ms	45-53 ms
CSF	4300 ms	1442-2000 ms	–

Table 1: Relaxation times (T_1, T_2, T_2^*) of different brain compartments at 3T (Donahue et al., 2016; Peters et al., 2007; Wansapura et al., 1999).

COMPARTMENT	T_1	T_2	T_2^*
Arterial blood water	2200 ms	40 ms	37 ms
Venous blood water	2010 ms	12-15 ms	7-13 ms
Gray matter	1800 ms	45 ms	25-36 ms
White Matter	1100 ms	40 ms	24-35 ms
CSF	3800 ms	300-900 ms	168 ms

Table 2: Relaxation times (T_1, T_2, T_2^*) of different brain compartments at 7T (Peters et al., 2007; Grgac et al., 2013; Bluestein et al., 2012; Wyss et al., 2013; Pfeuffer et al., 2004; Rooney et al., 2007; Ogawa et al., 1993; Yacoub et al., 2001b; Ivanov et al., 2013; Koopmans et al., 2008; Li et al., 2006).

Changes in the dHb content within a voxel modify the associated T_2^* and T_2 values. Therefore, sequences that are generally used to map BOLD signal changes are based on GRE and spin echo (SE) contrasts, which are T_2^*- and T_2-weighted, respectively.
Although both sequences are sensitive to oxygenation changes and are similar in principle, the location and extent of the detected changes is not identical.
Regarding the readout, EPI offers the most suitable option for functional experiments, due to its speed and high sensitivity (Mansfield, 1977) and it has been used both in combination with GRE and SE.

Principles of GRE

For GRE sequences, an echo is formed when the frequency-encoding gradient (of positive polarity) exactly counterbalances an initial negative gradient lobe and the signal relaxes with R_2^*, which is the sum of R_2 and R_2' effects ($R_2^* = R_2 + R_2'$).

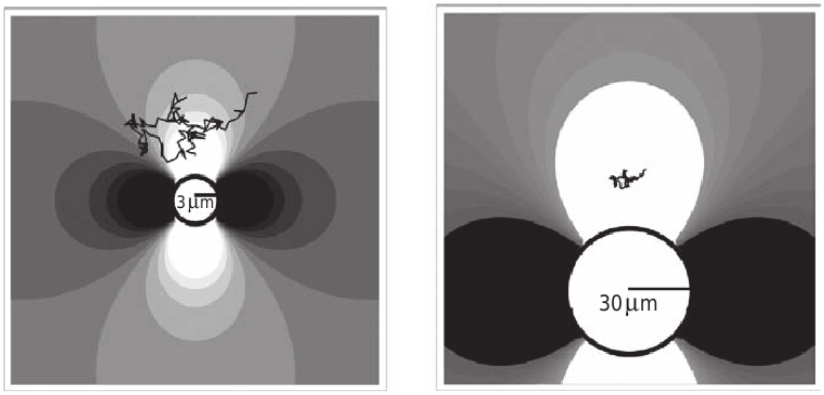

Figure 13: Dynamic averaging and static dephasing regimes. (a) Water molecules sample a range of different magnetic field around small vessels, due to the smaller scale of field inhomogeneities (dynamic averaging). (b) Water molecule sample a rather constant magnetic field around larger vessels (static dephasing). Picture taken from (Buxton, 2009).

Principles of SE

SE-EPI is very similar to GRE-EPI, with the exception that it adds a 180° pulse at $T_E/2$ to flip the phases and refocus T_2' effects and, hence, isolates pure T_2 effects. A net phase change is observable under static dephasing conditions, which are fulfilled around large vessels (as explained in Section 3.2.1), due to the extended spatial scale of the inhomogeneities. In case of dynamic averaging, there is no net phase change and the spin history cannot be recovered by a refocusing pulse.

Comparison between SE and GRE

In resume, T_2^* contrast arises from the IV+EV compartments of small+large vessels, while T_2 arises from the IV+EV compartments of small vessels and from the IV compartment of large vessels only. The fact that SE eliminates the EV signal around large vessels makes

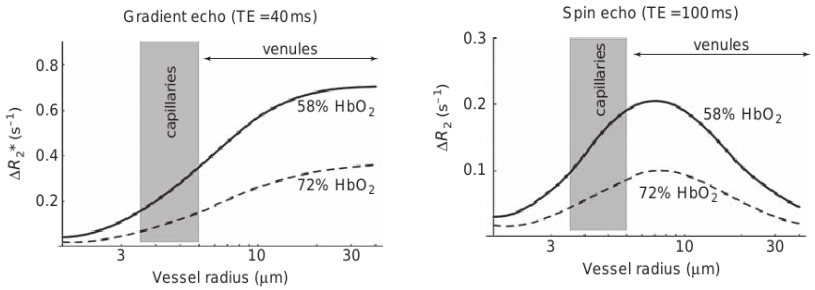

(a) (b)

Figure 14: Vessel size specificity of GRE and SE for two different oxygenation levels. (a) Amplitude of ΔR_2^* as a function of vessel radius for GRE. (b) Amplitude of ΔR_2 as a function of vessel radius for SE. Picture taken from (Buxton, 2009).

it more specific to the microvasculature than GRE and potentially closer to the actual site of metabolic changes within the parenchyma. At high fields, where the IV contribution decreases (due to a relative shortening of blood T_2 with respect to tissue T_2, see Tables 1 and 2) this effect is even more pronounced, making SE the sequence of choice in terms of spatial specificity.
However, the functional contrast of GRE and SE, which depends on ΔR_2^* and ΔR_2 respectively, is not of the same magnitude in correspondence of the microvasculature. Figure 14 shows the changes in relaxation rates for the two techniques as a function of vessel radius. While SE is largely devoid of large vessel contributions, GRE is dominated by signal changes arising from them. The scale of the two y-axes in Fig. 14 is different, meaning that ΔR_2^* are actually larger than ΔR_2 for all vessel sizes considered, even for the capillaries (shaded areas). Thus, refocusing T_2' effects reduces the sensitivity, and it was estimated that the ratio $\Delta R_2/\Delta R_2^*$ is 0.3-0.4 at 1.5 T and also at 9.4 T (Mohamed, 2006), meaning that the sensitivity of SE with respect to GRE does not increase for higher field strengths.
So, despite the large venous vessel contamination, GRE-EPI has been the mostly used technique at any field strength due to its high sensitivity and ease of implementation. Furthermore, the microvascular specificity of GRE increases supralinearly with B_0, with a ΔR_2^* ratio between 7 T and 4 T of 2.1 in gray matter and of 1.2 in vessel regions (Yacoub et al., 2001a).

3.2.3 *The Haemodynamic Response Function*

The haemodynamic response function (HRF) describes the temporal evolution of BOLD signal changes upon an ideally infinitesimally short stimulation. For longer stimuli, the HRF adds up linearly.
The time scale of the BOLD response is much longer than the one of

neuronal activity, due to the fact that vascular responses are much slower than neuronal changes.

Some features of interest of the response are the so-called initial dip and post-stimulus undershoot (PSU). Different theories have been formulated regarding the origin of these effects. It is generally agreed on the fact that they originate from temporal mismatches of the different variables building up the final dHb dynamics. In the balloon model, Buxton et al. model the CBV return to baseline to be slower than the CBF (Fig. 15), with the physiological motivation of relatively elastic arterial smooth muscle (regulating CBF) versus the passive volume changes happening in the veins (that contribute to BOLD due to the dHb content in the veins). Such mismatch would be sufficient explain the PSU without the need of assuming an uncoupling between CBF and $CMRO_2$ (Buxton et al., 1998).
Regarding the initial dip, a mismatch in OEF and CBF, due to an early increase in $CMRO_2$ before CBF starts to rise, would be a possible explanation, but it is not excluded that it might rise from a decoupling of CBF and CBV (Buxton, 2012).

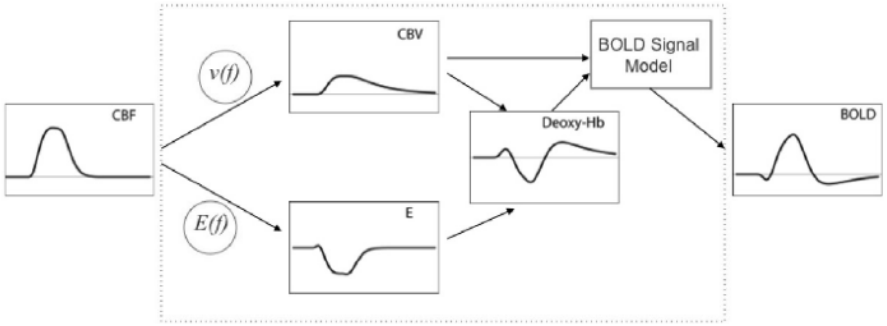

Figure 15: The HRF in the balloon model view. Picture taken from (Buxton, 2012).

The initial dip and the PSU have rised interest among the fMRI community due to the fact that they could be associated to interesting physiological features. The initial dip, indeed, has been related to the site of metabolic change in the hypothesis that it reflects an early oxidative metabolism change or an early arterial/arteriolar blood volume increase (Uludag, 2010), and it has been also investigated at high resolution (Siero et al., 2015). On the other hand, the PSU represents an interesting feature *per se*, and many works tried to understand whether it comes from a neuronal inhibitory mechanism or a vascular balloon-like effect (van Zijl et al., 2012).

3.3 CBF AND CBV MAPPING

The complex interplay of CBF, CBV and $CMRO_2$ behind the BOLD response makes it difficult to interpret. Mapping CBF and CBV changes

can be achieved non-invasively with arterial spin labeling (ASL) and vascular space occupancy (VASO), respectively, and is reviewed in the following subsections.
The advantage of having pure CBV and CBF instead of BOLD is the increase in specificity (due to the flow-regulation at the arteriolar and capillary level) and the possibility of comparing them across participants and tasks (less baseline effects than BOLD).

3.3.1 *CBF Mapping with ASL*

As discussed in Section 3.1.3, blood flow is regulated at the arteriolar and capillary level, i. e., close to the site of oxygen and glucose uptake. Therefore, CBF mapping is a useful quantity for studying location and effect size of metabolic changes following a stimulus, but also to localize hyper- and hypo-perfused regions in disease. CBF describes perfusion, i. e., the volume of blood that is delivered to 100 g of tissue per minute and is, therefore, measured in ml of blood/100 g of tissue/min. The most widespread sequence for measuring CBF is ASL and variations of it.

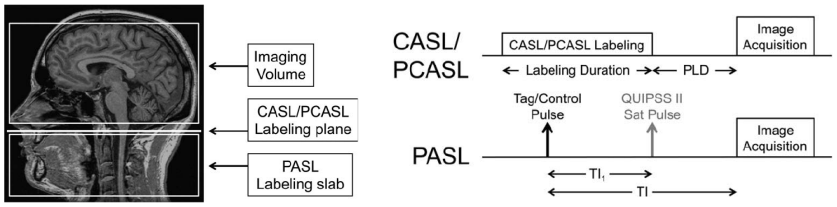

(a) (b)

Figure 16: (a) Graphic representation of the difference between CASL, pCASL and PASL. (b) Schematic of the acquisition scheme for CASL, pCASL and PASL. Pictures taken from (Alsop et al., 2015).

ASL is a non-invasive technique, based on T_1 contrast, which uses magnetically-tagged water protons as diffusible tracer to measure perfusion. In practice, the same volume is acquired with and without tagged water in an interleaved fashion, such that tag images alternate to control images. Any voxelwise difference between the tag and the control image should be related to the difference in the signal coming from the arterial blood water delivered during inversion time (TI). The amount of arterial water delivered is directly proportional to CBF and, hence, gives a measure of perfusion.
The water labeling follows the application of one or more RF pulse in the tagging plane, after which the spins are allowed to travel to the imaging plane after a delay time. Therefore, water magnetization decays between the tagging plane and the imaging slice, and depends on blood T_1. When the tagged water reaches the capillary and exchange with tissue, the decay is dominated by tissue T_1.

ASL labeling approaches

There are essentially two ways of labeling spin: continuous and pulsed.
In the continuous approach, the labeling occurs during a relatively long period of time (1-3 s) and is applied on a labeling plane. The tagging can be achieved with CASL, in which a single RF labeling pulse is used, or with pCASL, in which many rapid RF pulses are applied consecutively. pCASL can achieve better labeling efficiency and it is, thus, the variant of choice among the continuous techniques (Fig. 16).
In PASL, a single, short pulse (10-20 ms) is applied over an extended labeling slab (10-20 cm thick). With respect to pCASL, the SNR of PASL is lower, due to the fact that the labeling slab in PASL depends on the transmit RF coil coverage, so the bolus generated is generally of lower temporal duration, and suffer from more T_1 decay due to the istantaneous labeling (Alsop et al., 2015).

One of the main drawback of ASL is that its SNR is low compared to BOLD (Donahue et al., 2016).
ASL benefits from high-field acquisition due to the lengthening of T_1 values (see Tables 1 and 2 for comparison between 3 T and 7 T), which gives more time for post-labeling and readout because the spins keep their tagging for longer (Gardener et al., 2009). However, the increase in spatial inhomogeneity of B_0 and B_1 and the smaller coverage of RF transmit coils available at $B_0 \geqslant 7$ T, practically make the implementation of ASL at high field and high spatial resolution challenging and not readily suitable for submillimeter-resolution studies.

3.3.2 *CBV Mapping with VASO*

Mapping functional changes in CBV is, similarly as for CBF, interesting because it is a single variable (unlike BOLD) and because it is more specific to the location of metabolic changes, given that arterioles and capillaries actively dilate if the oxygen demand increases. Additionally, CBV is not always coupled to CBF and, therefore, an independent measure of it can help investigating the mechanism of flow-volume coupling (Goense et al., 2012).

The most widespread method for measuring CBV non-invasively with MR techniques is VASO. Other methods include monocrystalline iron oxide nanoparticle (MION), PET-based CBV measurements and gadolinium-CBV, which have been also used for VASO validation (Donahue et al., 2016).

Principles of VASO

VASO is based on T_1 differences between blood and tissue. The blood water magnetization is manipulated, so that its longitudinal component is zero at the time of image acquisition, and the signal comes from the tissue only. Changes in signal within a voxel are, thus, directly related to blood volume changes.
The nulling of blood water magnetization is achieved by application

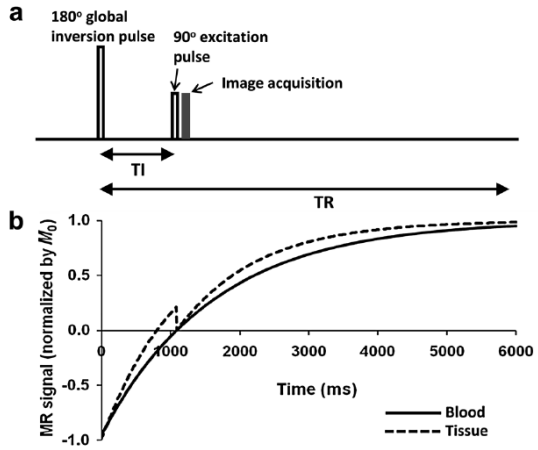

Figure 17: (a) Pulse sequence diagram for VASO. (b) Corresponding blood and tissue magnetization evolution. Picture taken from (Lu et al., 2013).

of a non-selective adiabatic inversion pulse and exploiting the difference in T_1 between blood and tissue ($T_{1,\text{tissue}} < T_{1,\text{blood}}$), which allows some residual tissue magnetization (approximately 10-20% of M_0) at the time TI, when the blood magnetization is zero and the image is acquired (Fig. 17).
The main problems related to VASO are due to inflow of fresh blood water and perfusion effects, both of which are minimized at long T_Rs (above 5000 ms) and, thus, come at the cost of temporal resolution. For this reason, several strategies have been implemented in order to minimize those artefacts (Donahue et al., 2016).

At high fields ($B_0 \geqslant 7$ T), benefits to the standard VASO technique are limited. On one hand, tissue and blood water T_1s start to converge, leaving only little magnetization available at the time of image acquisition and further reducing the SNR. On the other hand, BOLD-contamination effects are also stronger at high fields. In order to overcome those issues, slightly different implementations have been developed for high-field applications (Hua et al., 2013; Huber et al., 2014a). The slice-saturation slab-inversion VASO (SS-SI-VASO) (Huber et al., 2014a) is used in this work and its details of are, thus, discussed in the Methods.

4

THE CORTICAL LAYERS

The human neocortex can be though of as a convoluted sheet covering white matter. Its thickness can vary from approximately 1 to 5 mm depending on the brain region and local cortical curvature. Gray matter can be generally divided into six layers that run parallel to the surface; the definition of layers is based on the cell body arrangement (cytoarchitecture). Just like the thickness, the relative extent of each layer is area-specific. The motor cortex, for example, has only five layers because layer IV is lost during postnatal development.

Layers are segregated based on their function, such as input and output, and represent, thus, mesoscopic functional units.
The study of layer function has recently gained interest because it can provide information on cortical circuitry, on feedforward/feedback activities (Muckli et al., 2015; Olman et al., 2012) and on spatio-temporal features of functional responses, such as neurovascular coupling in positive and negative BOLD (Goense et al., 2012).

Functional imaging of layers is far from being a routinely-performed, standardized acquisition. Challenges arise from the high spatial resolution required (typically layers are below 1 mm thick), the physiological limits of BOLD (which is weighted towards the draining vasculature) at those resolution, the inadequacy of standard fMRI analysis tools, which were originally developed for voxel volumes on the order of $3 \times 3 \times 3$ mm^3. Therefore, imaging of layers requires improved acquisition and analysis strategies.

This chapter reviews the anatomical and functional characteristics of cortical layers with a focus on primary motor cortex (M1) (area 4) and primary somatosensory cortex (S1) (areas 3, 1, 2).
Section 4.1 reviews cellular and vascular composition of layers; Section 4.2 relates the anatomical properties of layers to the observed functional responses.
Throughout the chapter, the term *layer* indicates a cytoarchitectonically defined layer, while *vascular layer* indicates a layer defined by the vascular density and *lamina* indicates an artificial depth-dependent surface that do not necessarily correspond to an anatomical layer.

4.1 HISTOLOGY AND VASCULATURE

4.1.1 *Architectonics*

Neocortical layers are numbered from I (superficial) to VI (deep) based on their cell composition and density. Layers can be also referred to

as: molecular layer (layer I), external granular layer (layer II), external pyramidal layer (layer III), internal granular layer (layer IV), internal pyramidal layer (layer V) and multiform, or fusiform, layer (layer VI). Granular cells, abundant in granular layers, are a type of neuron with relatively small cell body and short axon. Pyramidal cells, which characterize agranular layers, are a type of neuron with bigger cell body and long axon.
Granular cortex is characterized by the presence of of layer IV (such as the postcentral gyrus); agranular cortex is lacking it (such as the precentral gyrus).

Equivolume arrangement of the cortical layers

The curvature of the cortex influences the thickness of the cortical layers differentially. The cortex appears squeezed at the sulci and stretched at the gyri, and so the layers. Bok identified the principal dendrites and defined the portions between them within a given layer as segments. He found that the volume of a segment is constant with respect to the curvature (Fig. 18), so that each segment located in the same layer has the same volume, regardless of its location along the cortical surface (Bok, 1929). This so-called equivolume arrangement allows the cortex to compensate high levels of folding with increased thickness and thus to maintain its full function.

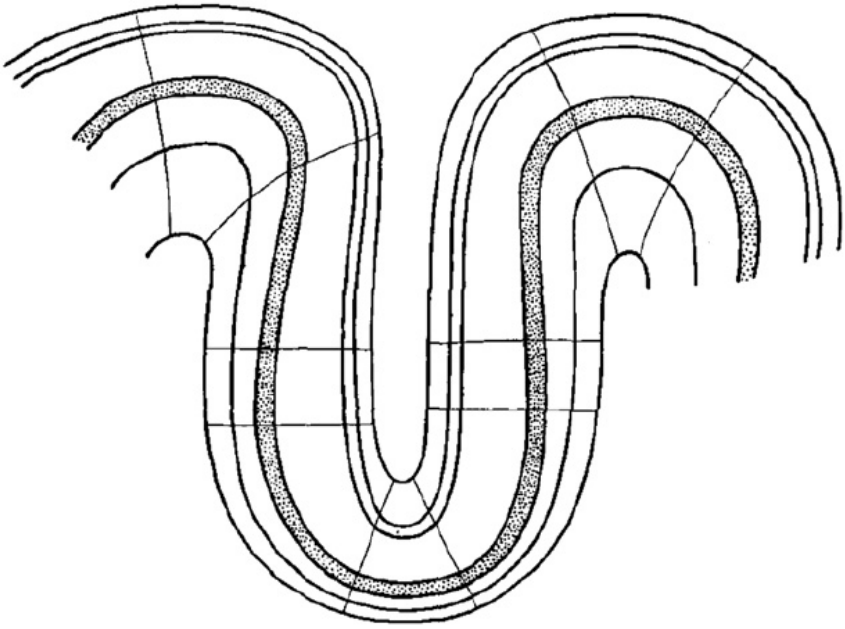

Figure 18: Sketch of the arrangement of the six cytoarchitectonic cortical layers. The lines perpendicular to the plane of the layers indicate principal dendrites and are delimiting one segment from the next. The relative volume is constant for each segment. Picture from (Bok, 1929).

4.1.2 *Vascular Composition of the Cortical Layers*

One of the relevant features for fMRI is the organization of the brain vasculature and its relationship to underlying cellular organization (Fig. 19). An extensive study in stained human postmortem samples was done in 1981 by Duvernoy et al. (Duvernoy et al., 1981). Brain vessels can be divided into pial, i.e., located at the cortical surface and parenchymal, i.e., running within the gray matter.

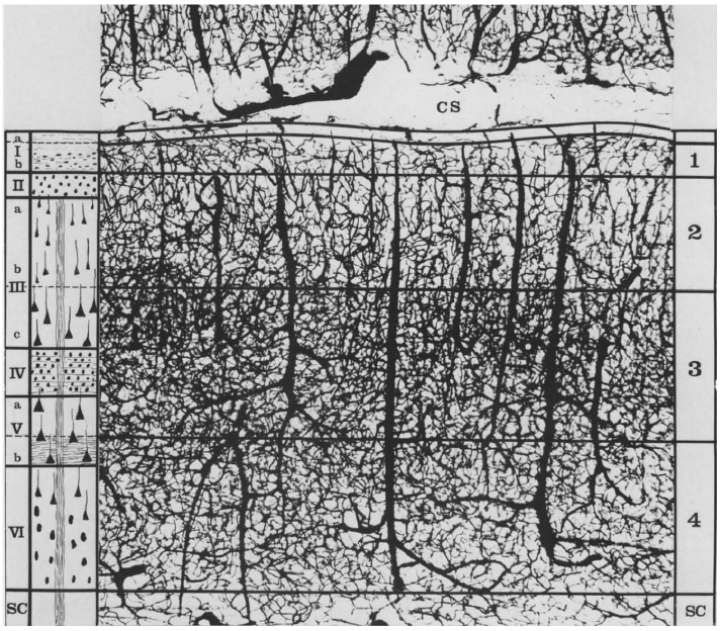

Figure 19: Intravascular india ink injection of a section of S1 (granular cortex) with an indication of the corresponding cellular layers. The vascular layer 3 presents the highest vascular density and includes part of cellular layers III, IV and V. I-VI: cellular layers, 1-4: vascular layers, CS: central sulcus, SC: subcortical white matter. Picture from (Duvernoy, 1999).

Pial vessels are the largest in size. Pial arteries, which supply the brain with oxygenated blood, can have diameters of 40-280 µm and pial veins, which drain away deoxygenated blood, of 130-380 µm. They are connected at right angles to cortical diving arteries and emerging veins, respectively.

Parenchymal vessels can be divided into arteries, arterioles, capillaries, venules and veins based on their size or oxygenation level (more on this in section 4.1.3). Capillaries are absent at the cortical surface and are more dense in the middle of the cortex. Opposite to larger vessels, which have a clear preferential orientation, they can branch in many more directions. Although the vast majority of fMRI models to date assumes the capillary orientation to be random, it has been shown by Lauwers et al. that they have a clear preferential orientation, approximately orthogonal to the surface, with a large degree (about 45°) of scattering (Lauwers et al., 2008).

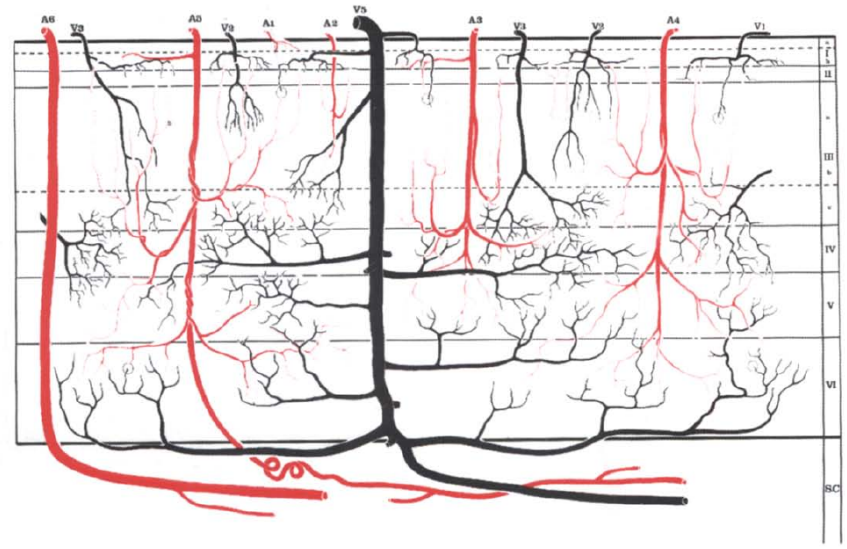

Figure 20: Intracortical arteries (red, labeled with A) and veins (black, labeled with V). The numbering (1-6) refers to the vessel classification based on their cortical reach, as detailed in the text. Picture taken from (Duvernoy et al., 1981).

Vessel classification

Following Duvernoy et al., parenchymal vessels can be classified into five groups based on their cortical reach (Fig. 20): groups 1 and 2 (reaching layers 2-3) include arteries with a diameter of 10-20 μm and veins of 20-30 μm; group 3 (reaching layers 3-5) arteries of 15-30 μm and veins of 45 μm; group 5 (reaching layer 6) arteries of 30-40 μm and veins of 65 μm; group 5 (reaching white matter) arteries of 30-75 μm and veins of 80-125 μm.
Capillaries are present in all layers but their density can vary with depth, especially in primary sensory cortices (Schmid et al., 2017). Their average diameter measures 5 μm.
Arterioles and venules can be further classified based on their branching order, with increasing order as the branching increases. So, high-order venules and arteries are closer to the capillaries than low-order ones.

Penetrating arteries are smaller in diameter than veins, but more numerous (Fig. 20), with a ratio of approximately 1.6:1 in visual cortex (Weber et al., 2008). This implies that the scale of regulation of blood irrigation and drainage are not analogous. Weber et al. found an irrigation volume of 0.44 mm^3 for large diving arteries and a draining volume of 0.70 mm^3 for large intracortical veins.

Imaging methods sensitive to hemodynamic changes in arteries have, thus, a different ultimate effective resolution with respect to methods sensitive to changes in veins (see Chapter 3 of (Ulmer and Jansen, 2010) and section 3.2 for further discussion).

Oxygenation, vascular composition and vessel size are relevant quantities for fMRI (as detailed in section 3.2). In parenchyma, the

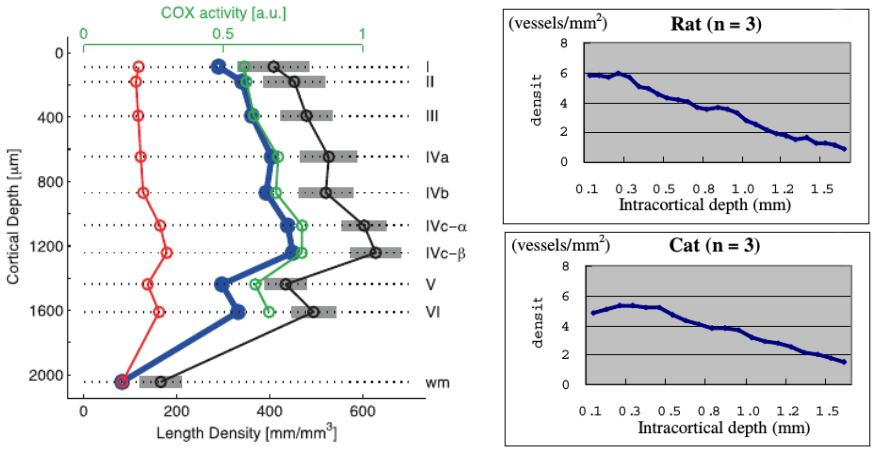

(a) (b)

Figure 21: (a) Density of capillaries (red), non-capillaries (blue) and overall parenchymal vessels (black) in V1. The green trace represents the cytochrome oxidase (COX) activity in arbitrary units. Modified from (Weber et al., 2008; Uludag et al., 2015). (b) Depth-dependent ICV density for rat and cat. Modified from (Park et al., 2005).

fraction of total blood volume (measured in ml of blood/ml of tissue) is 0.04-0.06 ml/ml, of which roughly 30% is arterial (precapillary) blood and 70% is venous (postcapillary) blood (van Zijl et al., 1998).

Vascular density across layers

The relative density of each compartment changes across depth. An enlightening study in macaque monkey primary and secondary visual cortices was done by Weber et al. (Weber et al., 2008). They reported that the microvascular density is strongly correlated with steady-state metabolism, and is maximal in layer IVc-β, while, interestingly, no strong correlation was found between the vascular density and the synaptic density (Weber et al., 2008) (Fig. 21a). Tsai et al. reported the same weak correlation in an extended number of regions of the mouse neocortex (Fig. 22) (Tsai et al., 2009).

The density of ICVs, i. e., the principal veins that are crossing gray matter (GM), increases from deeper to upper layers. A study comparing different species and brain regions found a similar shape of the density of vessels across the cortex (Fig. 21b) (Park et al., 2005), and simulations based on those findings reproduced accurately BOLD responses in humans (Markuerkiaga et al., 2016).

Vascularization of the primary motor and somatosensory cortices

Although the macrovascular depth-dependent density is similar in all species and brain region, the microvascular density is not. Therefore, results like the ones shown in Fig. 21a are only applicable to the brain region considered (visual cortex in that case). The sensory and motor cortices present a different vascular network organization. An india ink injection of a section of the central sulcus can be observed in Fig. 23. The gray matter can be easily distinguished from white

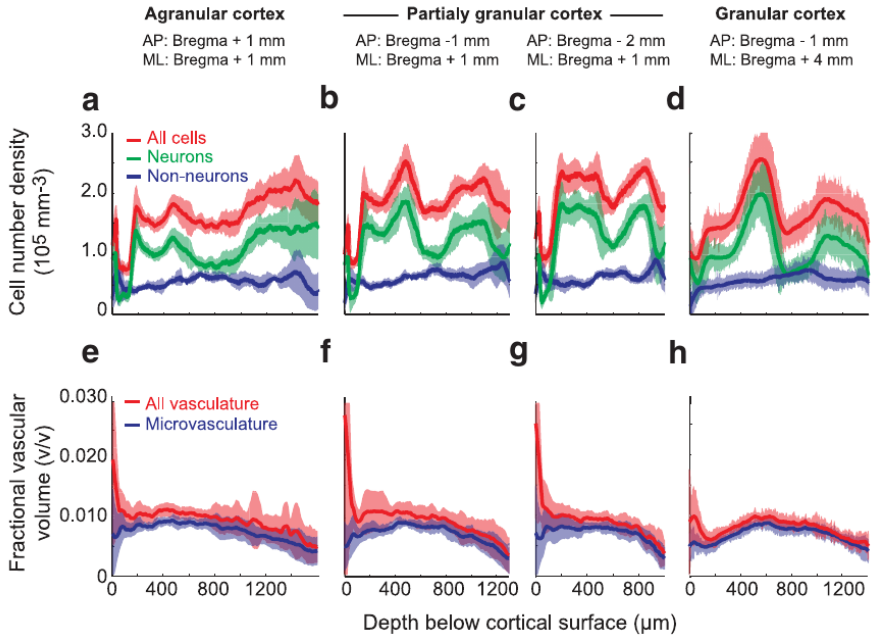

Figure 22: (a)-(d) Depth-dependent number densities of all cells (red), neurons (green) and non-neurons (blue) per unit volume of tissue in the mouse neocortex. (e)-(h) The corresponding fractional volume occupied by all vasculature (red) and by microvasculature (diameter < 6 μm; blue) as a function of cortical depth. AP: anterior-posterior; ML: medial-lateral. Picture from (Tsai et al., 2009).

matter due to the higher overall vascularization. M1 (the region extending upwards from the arrow in Fig. 23) has a homogeneous vascular network, with no appreciable density variations across cortical depth. S1 is not only thinner than M1 (approximately 2.5 mm versus 4.5 mm (von Economo and Koskinas, 1925)) but has also a more marked depth-dependent variations in vascular density. From Figs. 19 and 23 it is clear that vascular layer 3 of S1 is characterized by the highest microvascular density, which will have an impact on the relative amplitude of the BOLD response.

4.1.3 *Blood Oxygenation and Velocity*

The blood-borne oxygen extracted at the capillary level is supplied by the arteries and drained away by the veins. Arterial blood is, thus, more oxygenated than venous blood (and for this reason also brighter in color). The OEF in normal conditions is approximately 0.44, meaning that the oxygen content of the blood is decreased by 44% during its transit from the arteries to the veins (Ito et al., 2004). OEF is not a fixed quantity, and it generally decreases during activation.

Typical blood oxygen saturation (SO_2) levels are 95-100% for pial arteries and are 55-65% for pial veins. SO_2, though, changes substan-

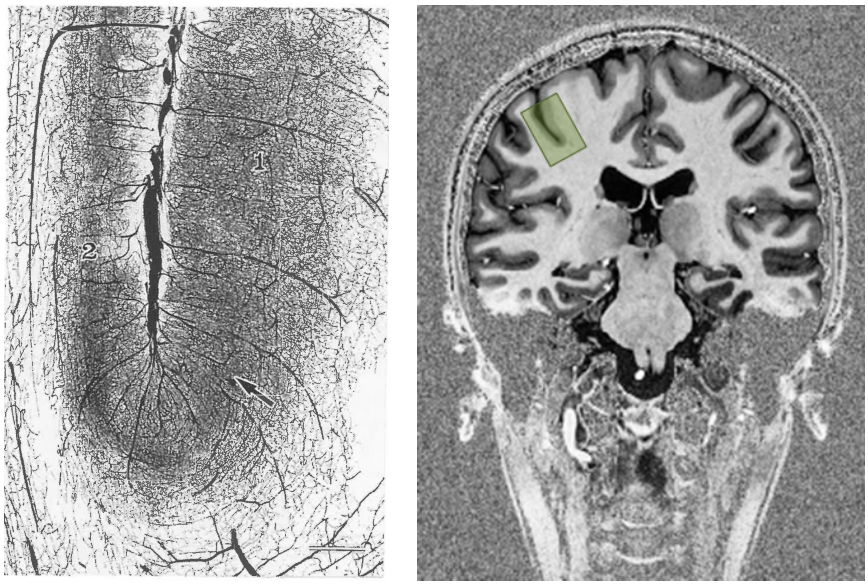

(a) (b)

Figure 23: Vascularization around the central sulcus. (a) Intravascular india ink injection of a section of the central sulcus. The side marked with 1 indicates the motor cortex (agranular cortex) and 2 the sensory cortex (granular cortex). The section shows the difference in thickness and vascularization between the two cortices: the sensory cortex is thinner than the motor cortex and has a high density of the third vascular layer (see also Fig. 19). The motor cortex has a more homogeneous vascular network. The sensory cortex extends around the bottom of the sulcus into area 3a (arrow). Bar length: 1.2 mm. Picture from (Duvernoy, 1999). (b) Indicative referential location of the anatomical section shown in (a).

tially also within the arteriolar, capillary and venular compartments. Sakadžić et al. reported a drop in SO_2 in mice from ~95% for low-order arterioles to ~73% for higher-order arterioles, and an increase from ~40% to ~65% going from high- to low-order venules. In the capillaries, SO_2 drops from ~65% to ~35%.

The relatively large change in SO_2 in the precapillary compartment means that some oxygen is extracted at the level of the arterial compartment. The portion of extracted oxygen was estimated to be about 50% of the total oxygen extracted during one arteriovenous passage (Sakadžić et al., 2014) and is somehow in contrast with an earlier view, considering the capillary bed the most relevant location of oxygen extraction. Another surprising finding is that the oxygenation level in the postcapillary venules slightly increases going downstream, challenging the idea of a constant SO_2 for the whole venular and venous vasculature. The reason for this has been explained in terms of oxygen diffusing in the cerebrospinal fluid (CSF) and tissue from arteries to ascending and pial veins (Blinder and Uludağ, 2016).

COMPARTMENT	SIZE Ø (μM)	SO_2 (%)	BLOOD VELOCITY (CM/S)
Arteries	30-280	95-100	0.54-2.11
Arterioles	10-120	75-95	0.41-1.09
Capillaries	5-8	30-80	0.07
Venules	15-180	40-60	0.09
Veins	20-590	55-65	0.20-0.44

Table 3: Size (diameter of the cross sectional area), oxygenation levels and blood velocity in different vascular compartments. Size and oxygenation values from (Donahue et al., 2016; Piechnik et al., 2008; Turner, 2002). Velocity values from (Kramer et al., 1974).

The change in SO_2 at baseline as a function of vessel diameter can be observed in Fig. 25 (full symbols).

A resume of some vascular and blood properties can be found in Table 3.

4.2 FUNCTIONAL CHARACTERIZATION

In section 4.1.1, it was stated that layers can be classifies based on their relative cell type abundancy. Nevertheless, the cell type itself does not completely explain function. For example, pyramidal cells, which are the main type of neuron in agranular layers, can be connecting to the different regions: pyramidal cells in layer II project to ipsilateral cortex, in layer III to contralateral cortex, in layer V to subcortical structures and in layer VI to thalamus.

Therefore, in functional terms, cytoarchitectonic layers can be divided into three units: the supragranular layer (including layers I to III), where the origin and termination of intracortical connections (inter- and intra-hemispheric) are located; the internal granular layer (layer IV), which receives thalamocortical connections and is particularly pronounced in sensory cortices; and the infragranular layer (layer V and VI), which connects the cortex to subcortical regions and is mainly developed in motor areas.

M1 and S1 circuitry

The afferents to M1 and S1 can be the thalamus, the ipsilateral cortex and the contralateral cortex. The thalamic input ends up in layer IV of S1 and in layers III and V of M1. The ipsilateral projections between M1 and S1 come from pyramidal cells in layers II and III and terminate in layers II and III of the two cortices. The contralateral connections proceed via corpus callosum and terminate to layers above those where the thalamocortical connections are most dense in S1. In M1 there are no callosal afferents. Efferent projections to basal gan-

glia, brain stem and spinal cord come from layer V of M1; efferents to the thalamus come from layer VI of M1.

4.2.1 *Hemodynamic Changes*

Laminar changes in BOLD, CBV *and* CBF

The functional segregation of layers and the fact that the vascular density reflects metabolism (Fig. 21) make functional imaging of layers possible. BOLD-based fMRI has the disadvantage of being weighted towards the venous vasculature, particularly to the large veins located at the pial surface, which have a large resting cerebral blood volume (CBV_0) and produce the largest BOLD signal changes. Pial veins do not colocalize with the site of neuronal activation and are, thus, said to be spatially unspecific. CBF- and CBV-weighted fMRI are more specific to the parenchyma and can resolve layers functionally (Goense et al., 2016). The study in Fig. 24 shows that the activation of layer IV of the cat visual cortex (elicited by visual stimulation) is visible in both CBV (Fig. 24b) and CBF (Fig. 24c) sensitive imaging, but not in BOLD, for which most of the signal changes comes from the cortical surface (Fig. 24a) (Jin and Kim, 2008a).

The magnitude of BOLD signal changes depends on baseline parameters and on functional variables. It can be written as Eq. 54 (for the derivation of the equation see Chapter 6):

$$\frac{\Delta S}{S_0} = M\Big[1 - \nu\Big(\frac{r}{f}\Big)^{\beta}\Big]. \tag{54}$$

The term $\Delta S/S_0$ denotes BOLD signal changes (S_0 being the baseline signal and $\Delta S = S_{act} - S_0$, with S_{act} being the signal during a task); the terms in square brackets are the variables that change during functional activation (ν denotes the change in blood volume, f in blood flow, r in oxygen metabolism and β is a field-dependent exponent); the parameter M reflects the baseline contribution of the response and can be expressed as in Eq. 55:

Baseline contributions

$$M = k\,CBV_0\,\big[dHb\big]_0^{\beta}\,T_E \tag{55}$$

where k is a proportionality constant, CBV_0 is the baseline blood volume, $\big[dHb\big]_0$ the baseline concentration of deoxy-haemoglobin and T_E the echo time. Therefore, the baseline values of CBV and dHb concentration have an influence on the BOLD response. Those are quantities that do not only depend on the vascular compartment but also on the cortical depth and represent a systematic bias to the magnitude of the cortical profile of evoked BOLD signal changes. A more detailed discussion on the baseline effects can be found in Chapters 6 and 8.

Apart from baseline contributions, there are depth-dependent features induced by functional activation. Upon strong stimuli, such as

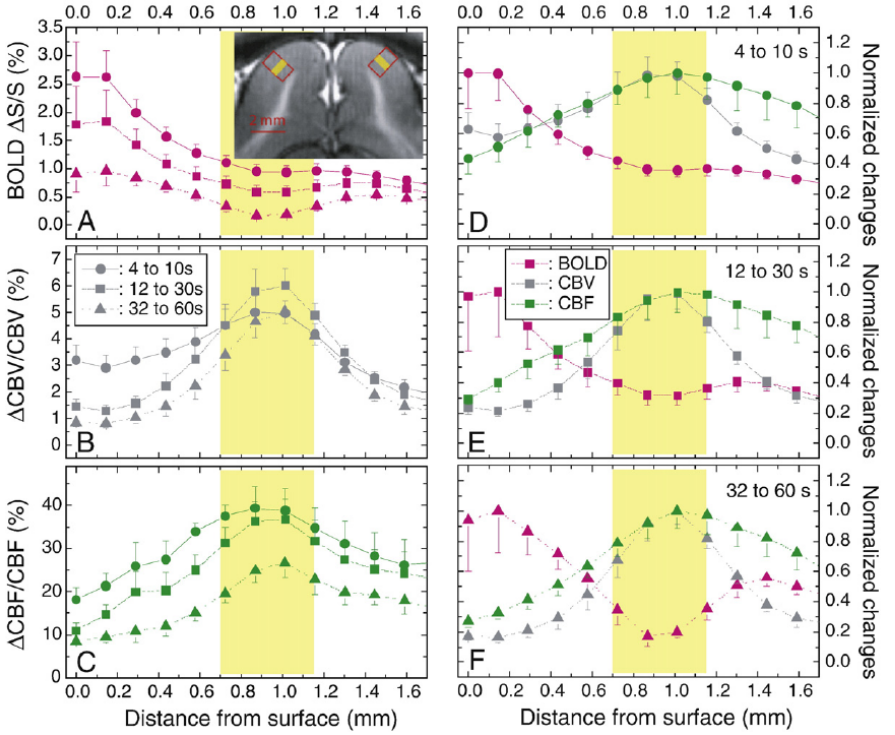

Figure 24: (a) BOLD changes, (b) CBV changes and (c) CBF changes in the cat visual cortex upon visual stimulation as a function of cortical depth and stimulus duration. (d-e) depth-dependent BOLD, CBV and CBF changes grouped by time periods of the stimulus. CBV and CBF signal changes peak in correspondence of layer IV (indicated by the yellow band), while BOLD signal changes peak at the pial surface. Picture from (Jin and Kim, 2008a).

hypercapnia, the oxygenation in the postcapillary vasculature changes from $(64 \pm 6)\%$ to $(72 \pm 6)\%$ and results in $\Delta T_2^* = 4$ ms (for intravascular BOLD in humans) (Ivanov et al., 2013). A comprehensive study of oxygen saturation changes during hypercapnia in mice showed that there are relevant increases not only in the postcapillary vessels, but also on the arteriolar side, whose magnitude depends on the vessel diameter and branching order (Fig. 25). Nevertheless, the arteriolar oxygen saturation changes are much smaller than the venular ones (about one third), meaning that imaging techniques based on pure oxygenation changes will be biased towards the postcapillary compartment.

T_2^* and T_2^* changes

Values of T_2^* and ΔT_2^* across layers are of interest for BOLD imaging.

In a study of the human visual cortex by Koopmans et al., marked T_2^* variations across layers were reported. Those differences reflect the different degrees of myelination and vascularization of the cortex (Koopmans et al., 2011). Changes in T_2^* during activation (within layers) were also found to be depth-specific and mostly confined to the

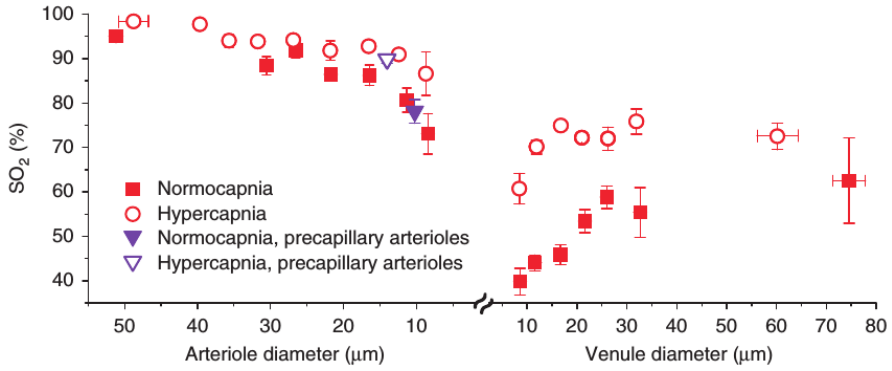

Figure 25: Intravascular oxygen saturation (SO_2) in mouse cerebral cortex as a function of the arteriolar and venular diameter during hypercapnia and normocapnia. The full symbols represent the values during normocapnia and the empty symbols the values during hypercapnia. Modified from (Sakadžić et al., 2014).

parenchyma rather than upper layers.
A study by Yen et al. using bilateral electrical stimulation of wrists in awake marmosets, confirmed that changes in T_2^* are specific to the parenchyma and that the earliest onset time is found in layers III-IV. Both studies reported that upper layers are dominated by S_0 changes, but those are likely to be apparent changes due to the fact that the model fit does not hold true anymore due to the lengthening of blood T_2^* during activation.
However, from the abovementioned studies, it is clear that the laminar contrast depends on the T_E used, given that each layer is characterized by a different T_2^* value and, therefore, distinguishing activity from different layers does not depend solely on the task and brain region considered, but also on the sequence parameters.

Spatial localization of the stimulus onset

Finally, the combination of spatial and temporal features of the response is relevant for the study of brain physiology. In studies comparing fMRI with 2-photon microscopy in the rat S1 upon electrical stimulation, it was observed that the onset and time to peak of the dilation onset decreases with increasing cortical depth (Tian et al., 2010). The dilation was reported to initiate below layer IV (that is the layer where the largest metabolic change is expected), i. e., in the infragranular layers V and VI (Uhlirova et al., 2016), and then propagate upward, with the largest delay in the capillaries of layer I.

The onset of the BOLD response does not necessarily initiate in deep layers together with the dilation. Yu et al. used line-scanning fMRI to show that layer IV of S1 is the first to produce a BOLD response upon direct forepaw stimulation in rats (Yu et al., 2014), consistent with the fact that layer IV is the input layer in the primary somatosensory cortex.

Part III

METHODS

5

SS-SI-VASO

CBV dynamics has been shown to provide better spatial localization of neural activity than BOLD signal changes. CBV changes can be obtained non-invasively with the VASO sequence (as described in Section 3.3.2).
At $B_0 = 7$ T, there are several challenges that hamper VASO implementation. First of all, $T_{1,blood}$ and $T_{1,tissue}$ are similar (see Table 2), which results in a small contrast-to-noise ratio (CNR) for VASO; moreover, BOLD effects are stronger with increasing field strength, and increasingly contaminate the VASO signal. Finally, inflow of non-inverted blood water spins is more likely to happen, because the inversion volume is smaller (typically only head coils are used at 7 T) and the time of blood nulling becomes longer, as compared to 3 T.
For those reasons, Jin and Kim state that a steady state for blood water spins is not achievable at 7 T and propose a slab-selective inversion (SI-VASO) approach (Jin and Kim, 2008b).
The slice-saturation slab-inversion VASO (SS-SI-VASO) technique manipulates tissue magnetization differently from blood magnetization, which is not considered to be in steady state. The contrast is, as in the original VASO technique, given by T_1 differences between blood and tissue.

This Chapter reviews the principles of SS-SI-VASO (Section 5.1) and presents two extensions to this technique: a simultaneous multi-slice implementation (Section 5.2), which increases spatial coverage, and a 3D implementation (Section 5.3), which provides SNR benefits in submillimeter resolution applications. Although the focus is on VASO considerations, the theoretical underpinnings are equally valid for BOLD imaging. BOLD contrast is, anyways, included in all SS-SI-VASO sequence variants and, therefore, simultaneous multi-slice (SMS) and 3D BOLD EPI could be considered as special cases of the SMS and 3D SS-SI-VASO implementations, respectively.

5.1 PRINCIPLES OF SS-SI-VASO

With respect to the standard VASO, the contrast in SS-SI-VASO is optimized by mutually adjusting the inversion time, the inversion slab and the inversion efficiency, and also by applying a 90° RF pulse in the imaging slice (Fig. 26) before slab-selective inversion.
The mutual time adjustments provides complete blood nulling in the microvasculature at the time of imaging, and the 90° RF pulses in-

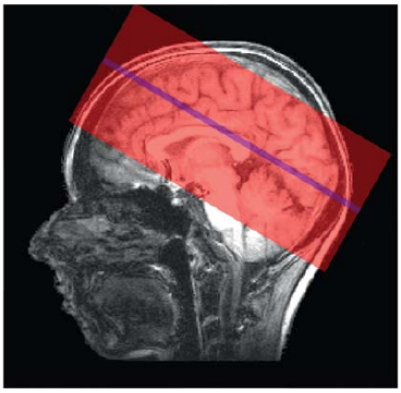

Figure 26: Indicative position of the inversion slab (red) and the imaging slice (purple) in SS-SI-VASO. Picture from (Huber et al., 2014b).

crease the available longitudinal magnetization of tissue at the time of image acquisition, consequently improving the mutual contrast. The 90° RF pulses are also used for acquiring additional volumes with pure BOLD contrast. Apart from providing a BOLD timecourse themselves, those volumes are used for removing BOLD contamination from the VASO contrast.

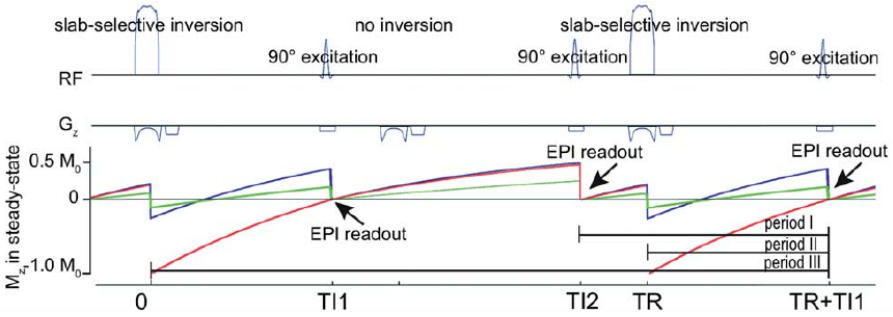

Figure 27: Sequence scheme for SS-SI-VASO. Red: once inverted blood; blue: gray matter; green: cerebrospinal fluid. Picture from (Huber et al., 2014b).

The above mentioned optimizations require some conditions to be fulfilled.

Once-inverted blood condition

The first condition is that, at time TI_1 (Fig. 27) all the blood present in the microvasculature of the imaging slice was inverted, and it was inverted only once. TI_1 corresponds to the blood nulling time, and is given by $TI_1 = \ln 2 \cdot T_{1,blood}$, in the assumption of a full inversion of the magnetization. At 7 T, $T_{1,blood} \approx 2100$ ms and, thus, $TI_1 \approx 1450$ ms. The arterial arrival time (AAT) of blood from the arteries at the upper neck to the microvasculature in the occipital lobe is $\approx$ 1500-2000 ms. Therefore $AAT > TI_1$, which means that there is no inflow of 'fresh' blood in the imaging slice at TI_1. In cases where $AAT < TI_1$, the technique is still applicable by making TI_1 shorter, reducing the inversion efficiency of the adiabatic preparation pulse. This is done

by adding a phase skip, which is proportional to the reduction in the transversal component of the magnetization, and in turn to the inversion efficiency (Huber et al., 2014b).

Refilling conditions

TI_2 is the time of pure BOLD contrast acquisition. In order to ensure that the microvasculature has been completely refilled before the EPI readout at TI_1, the time between the previous TI_2 and TI_1 (termed 'period I' in Fig. 27) should be longer than the microvasculature transit time. The microvasculature transit time has been estimated to be $\approx$ 1.16 s (Jespersen and Østergaard, 2012) and, hence, period I should be longer than that.
An additional refilling condition refers to 'period III' (Fig. 27); in order not to have any contamination from blood that has been inverted more than once, all of it should have left the imaging slice at the time of VASO acquisition (Jin and Kim, 2008b).

BOLD correction

If all the conditions are fulfilled and an interleaved BOLD/VASO timecourse is acquired, the correction for T_2^* effects can be performed. The GRE signal for voxels containing gray matter and blood during the blood nulled condition (nc), can be written as:

$$S_{GM,nc} \sim M_{z,GM,nc} \cdot e^{-T_E/T^*_{2,GM}} \tag{56}$$

where $M_{z,GM,nc}$ is the z magnetization of GM and is the variable of interest, since it changes accordingly to CBV changes. $T^*_{2,GM}$ is the T_2^* of gray matter. On the other hand, the signal for the blood condition, where blood magnetization is not nulled (nn) is described by the signal in the parenchyma (blood+GM):

$$S_{par,nn} \sim M_{z,par,nn} \cdot e^{-T_E/T^*_{2,par}} \tag{57}$$

where $M_{z,par,nn}$ is supposed not to change upon activation, due to the fact that blood and tissue have similar relative z-magnetizations at the time of BOLD contrast acquisition and, thus, redistribution of extravascular and intravascular comparment does not affect the overall longitudinal magnetization.
A CBV dependent quantities is, thus, obtained by dividing Eq. 56 by Eq. 57:

$$\frac{S_{GM,nc}}{S_{par,nn}} = \frac{M_{z,GM,nc} \cdot e^{-T_E/T^*_{2,GM}}}{M_{z,par,nn} \cdot e^{-T_E/T^*_{2,par}}} \approx \frac{M_{z,GM,nc}}{\text{const}} \propto 1 - \text{CBV}. \tag{58}$$

An additional assumption made in Eq. 58 was that the T_2^* of parenchyma (extravascular+intravascular) equals the T_2^* of gray matter (extravascular only), and that T_2^* does not change in the time between BOLD and VASO acquisitions.

Finally, it should be noted that VASO signal decreases are proportional to CBV increases (Eq. 58) and, therefore, negative signal changes are associate to an increase in blood volume fraction in the voxel.

5.2 SMS SS-SI-VASO

5.2.1 *Principles of SMS Readout*

Simultaneous excitation of multiple slices (SMS), or multiband imaging, has already been proposed in 1980 (Maudsley, 1980). Initially, due to the fact that single-channel receive coils were used, phase modulation of RF pulses was employed for disentangling the signal coming from different slices (Hadamard encoding). This required N_{slice} different phase patterns in order to disentangle the same number of different slices (Souza et al., 1988; Müller, 1988), which would improve the SNR but not the acquisition time. Larkman et al. proposed to combine multiband excitation with parallel imaging (pMRI) to disentangle the signal from different slices, which speeds up acquisition (Larkman et al., 2001).
Given its sensitivity and speed, the combination of SMS and pMRI to EPI represents an improvement to the standard multislice acquisition scheme (Moeller et al., 2010).

Multiband RF pulses

Multiband RF pulses deliver an increased SAR with respect to standard pulses. Parseval's theorem states that the power in image space scales like the power in k-space; therefore, for N simultaneously excited non overlapping slices, there is a proportional increase in power deposition (Barth et al., 2015). The power can, however, be reduced, and the following strategies have been proposed: VERSE (reduction of the amplitude of G_z at the peak RF power) (Conolly et al., 1988); optimized set of excitation phases by optimizing the modulation function (which is defined by $B_1(t) = A(t) \cdot B(t)$, where $A(t)$ is the $sinc$ function and $B(t) = \sum_j e^{i(\gamma G x_j t + \phi_j)}$ is the modulation function) (Wong, 2012); PINS (small G_z blips interleaved to rectangular RF pulses, which can be seen as a convolution of the slice profile with a comb function) (Koopmans et al., 2013); and multi-PINS (addition of a PINS pulse with a standard multiband pulse) (Eichner et al., 2014).

SMS sampling

The spatial encoding in multiband imaging can be achieved in three ways:

1. RF phase encoding: in this case, cycling patterns of RF phase are applied in order to shift the object within the FOV.
2. Gradient phase encoding: the z dimension, in this case, becomes a second phase encoding direction. Therefore, a FOV_z can be defined, such that $\Delta k_z = 1/FOV_z = 1/(N_{slice} \cdot gap)$, where gap is the distance between slices.
3. Coil encoding (pMRI): the sensitivity profiles is used for disentangling signal from different slices.

More often, a combination of gradient and coil encoding is employed, with the aid of CAIPIRINHA (described below).

Reconstruction methods: SENSE and GRAPPA

pMRI requires multiple receive coils, and exploits their sensitivity profiles in order to reconstruct the signal. It can be employed in standard multislice imaging as well as in SMS.

SENSE is an image-based method, in which a coil sensitivity matrix $\mathbf{C}$ is inverted in order to find the object $\boldsymbol{\rho}$ given the acquired data $\mathbf{S}$: $\boldsymbol{\rho} = \mathbf{C}^{-1} \cdot \mathbf{S}$. In general, $\mathbf{C}$ is not a square matrix and the inverse problem has an associated noise amplification, usually termed geometry factor, or simply g-factor. The g-factor depends on the matrix conditioning and in turn on the coil array geometry. For parallel imaging, the SNR penalty is given by:

$$\mathrm{SNR}_{\mathrm{pMRI}} = \frac{\mathrm{SNR}_{\mathrm{full}}}{g \cdot \sqrt{R}} \tag{59}$$

where g is the g-factor and R the acceleration factor. Closely spaced coils, or closely spaced slices (small gaps), produce similar sensitivity profiles, making the g-factor higher.
A solution to this problem is offered by CAIPIRINHA shifts (Breuer et al., 2005). CAIPIRINHA manipulates the phase of the RF pulse in order to achieve controlled FOV shifts of adjacent slices. This results in a much lower degree of signal overlapping and a consequent g-factor penalty reduction (Fig. 28).

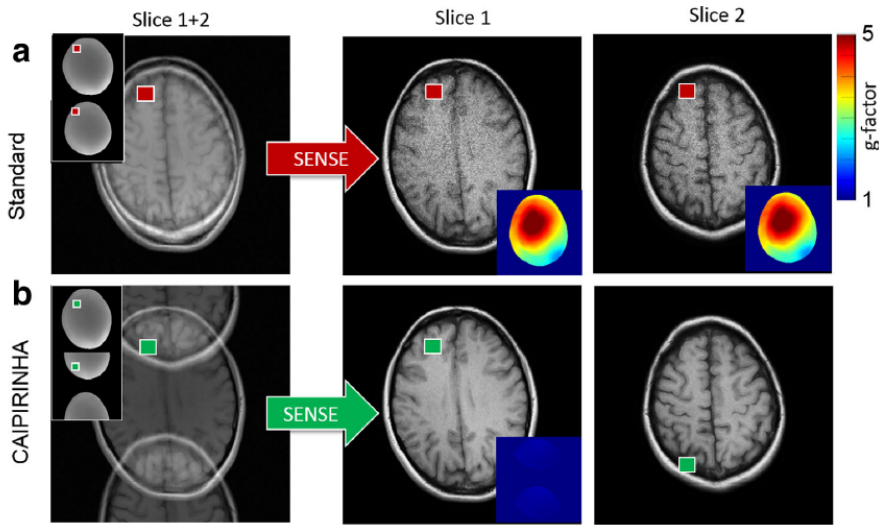

Figure 28: (a) Standard SENSE reconstruction and (b) CAIPIRINHA shifts added prior to SENSE reconstruction. CAIPIRINHA adds a FOV/2 shift for the most superior slices and reduces the noise coming from the inversion problem (g-factor). A g-factor of 1 is desired for no noise amplification (Eq. 59). Picture from (Barth et al., 2015).

GRAPPA is a k-space based pMRI reconstruction method. Missing k-space lines are synthesized before Fourier transform by a sliding-window method. To this end, an autocalibration signal (ACS), i. e., a fully sampled, low-resolution k-space, is acquired, which is used

to derive the GRAPPA weights. An improvement to the standard GRAPPA is represented by the slice GRAPPA, which uses slice-specific GRAPPA weigths.
An issue with GRAPPA is that the ACS lines are generally acquired in a segmented, multi-shot fashion in order to match echo-spacing and distortion of the fMRI timeseries. Therefore, the reference lines are acquired over some seconds, which introduces noise due to subject breathing. This noise is minimized if all segments of a given slice are acquired consecutively before shifting to the following slice, and the temporal stability is increased. This method is known as FLEET (Polimeni et al., 2016).

5.2.2 *Implementation in the VASO sequence*

The acquisition of multiple, consecutive slices, makes them to have different TI_1s. Therefore, the coverage of SS-SI-VASO is limited, especially when the resolution requires long echo trains.
The upper limit for readout is usually chosen in order to have variation in imaging time, ΔTI, not exceeding variations in blood nulling time, $\Delta T_1 \cdot \ln 2$. Variations in T_1 are due to fluctuations in oxygenation and haematocrit and are on the order of 200 ms. This restricts the acquisition window to less than 140 ms (Huber et al., 2015b), which corresponds to few slices, depending on the acquisition scheme (Huber et al., 2014b).

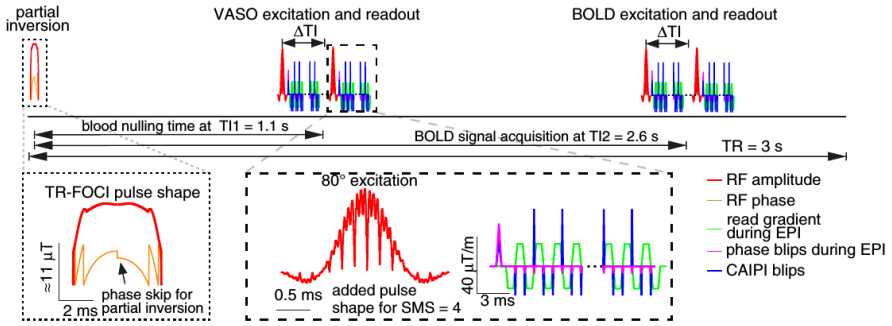

Figure 29: Acquisition scheme for SMS SS-SI-VASO. The inversion is achieved with a TR-FOCI adiabatic inversion pulse with reduced inversion efficiency; the multiband excitation pulse (red) for an SMS factor of 4 is shown. The VASO volumes are acquired in the time interval ΔTI_1, around the blood nulling time, $TI_1 = 1100$ ms. CAIPIRINHA (or CAIPI) blips (blue) are added for aliasing controlling, and here the CAIPIRINHA factor is 3. Pure BOLD signal is acquired at $TI_2 = 2600$ ms. Picture from (Huber et al., 2015b).

In light of this, an SMS acquisition can dramatically improve the coverage of the technique, and has been shown to extend the number

of slices that can be acquired to up to 20 (Huber et al., 2015b). SMS techniques achieve the acquisition of multiple slice simultaneously via a multiband excitation, and the coil sensitivities are then used to disentangle the signals from different slices.

Fig. 29 shows the acquisition scheme for SMS SS-SI-VASO for one repetition. The inversion is achieved with a TR-FOCI adiabatic inversion pulse (Hurley et al., 2010) with the addition of a phase skip in order to modulate the inversion efficiency and, in turn, the blood nulling time. At TI_1 and TI_2, VASO and BOLD volumes, respectively, are acquired: the multiband pulse is applied and the signal is readout. The summation of multiband *sinc* pulses is done using optimized phase schedules for minimizing peak RF power (Wong, 2012). In order to disentangle the signal coming from different slices, CAIPIRINHA shifts are applied (depicted in blue in Fig. 29). CAIPIRINHA is controlling the aliasing of each slice separately and hence aids image reconstruction (Breuer et al., 2005). ΔTI in Fig. 29 is the deviation from the predicted blood nulling time.

5.3 3D SS-SI-VASO

5.3.1 *Principles of 3D Readout*

The concept of a second phase encoding direction (corresponding to k_z) was already brought about in the previous section regarding SMS acquisition. Similarly, 3D acquisitions can benefit from an acceleration in the slice direction, which effectively reduces T_A. For example, for an acceleration factor of 2 in plane, the time saving for BOLD sequences is about 10-15% only, due to the T_E restrictions for maintaining a certain functional contrast (Poser et al., 2010). For the same acceleration in the slice direction, however, the time saving is 50%.

For 3D protocols, a thick slab (corresponding to the acquisition volume) is always excited, and k-space is sampled in 3 dimensions, plane by plane. To this purpose, frequency and phase encoding are analogous to the 2D case, and shot-to-shot increments of z gradients are applied (as in standard spin-warp imaging) to span the third dimension. A 3D Fourier transform is then performed to map the points in image space.
This method is different from echo-volumar imaging (EVI). In EVI, three-dimensional information is acquired during a single FID through gradient blips in two directions (y and z). Gradient hardware limitations, however, lead to long echo trains and sensitivity to susceptibility artefacts, which make this technique impractical.

One of the obvious advantages for the application of 3D readout is, thus, the possibility of using full acceleration capabilities (including CAIPIRINHA) in two dimensions, with a linearly dependent net decrease in acquisition time, similar as for the 2D SMS case. Addi-

tionally, the thickness of the excited slab gives an intrinsic SNR increase that scales with the square root of the number of slices: SNR $\propto \sqrt{N_{slices}}$. An advantage of 3D acquisitions over SMS is that, due to the excitation of a slab, high resolution in the slice direction is achievable without artefacts coming from imperfect slice excitation profiles.

On the other hand, the relatively long acquisition window (in the order of 100 ms), gives more time to physiologial artefacts (due to respiration, motion and heart beat) to build up. This results in image corruption if the physiological noise is the dominant part of the noise in the voxel, and this is generally true for voxels volumes of 1.3 µl and above.

It is, thus, challenging to infer from purely theoretical considerations whether 2D SMS or 3D readout is best suited for fMRI applications, as the choice is likely to be dependent on the desired spatial and temporal resolution, coverage and task.

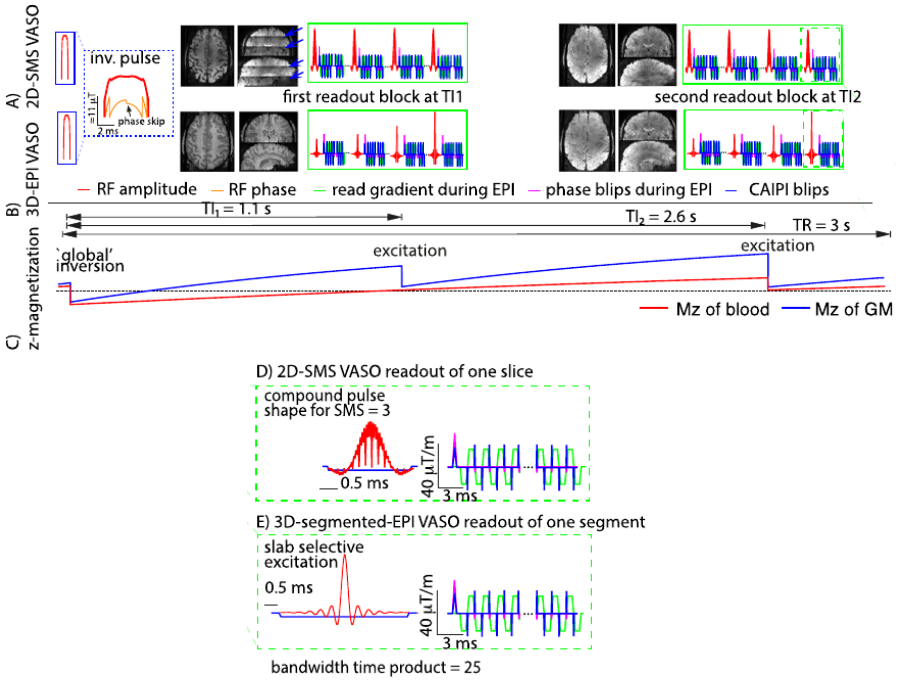

Figure 30: Acquisition scheme comparison between (a) SMS and (b) 3D SS-SI-VASO and (c) corresponding longitudinal magnetization evolution. In both cases, an adiabatic inversion pulse with phase skip is applied. VASO readout is at $TI_1 = 1100$ ms and BOLD readout is at $TI_2 = 2600$ ms. The repetition time is 3000 ms. (d) Readout block for one slice in SMS SS-SI-VASO, as described in Fig. 29. (e) Readout block for one segment in 3D SS-SI-VASO. A sharp slab-selective excitation with a bandwidth time product = 25 is applied. Adapted from (Huber et al., 2016b)

5.3.2 *Implementation in the VASO sequence*

CBV quantification can benefit from a 3D acquisition, since the effective TI_1 is constant across the whole volume.
However, due to the inversion pulse and the long T_R required in VASO, the 3D-EPI segments are acquired in a non steady-state condition (Huber et al., 2016b). This can cause T_1 blurring along the slice direction. To minimize this artifact, variable flip angles along z can be used to ensure a similar gray matter magnetization for every shot (Gai et al., 2011). Assuming $T_{1,GM} = 1800$ ms, T_1 relaxation between pulses can be estimated, and flip angles can be adjusted in order to have gradually increasing values, reaching up to a 90° excitation pulse at the end of the readout.

A comparison between SMS and 3D SS-SI-VASO acquisition schemes is shown in Fig. 30. An adiabatic inversion pulse is applied in both cases, and both sequences have the same TI_1 and TI_2. The readout follows a different selective excitation (slice and slab for SMS and 3D, respectively), as depicted in Figs. 30d-e. CAIPIRINHA shifts are used in both sequences, and therefore CAIPI blips are applied (Figs. 30d-e).

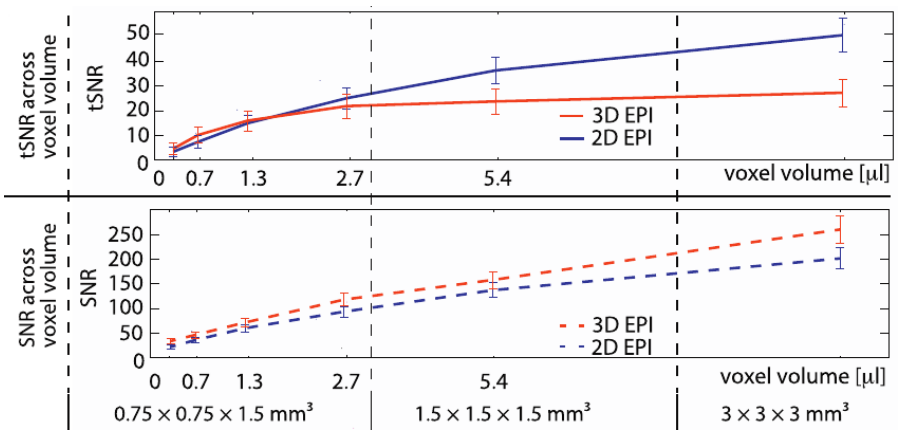

Figure 31: Top: temporal SNR comparison for SMS and 3D SS-SI-VASO across voxel volumes. It can be seen that for voxel volumes larger than 1.3 µl, the SMS version provides higher tSNR. This is due to the increasing physiological noise contribution in the voxel, as its volume increases. Bottom: SNR comparison for SMS and 3D SS-SI-VASO across voxel volumes. In this case, the 3D readout outperforms 2D SMS for all resolutions investigated. Adapted from (Huber et al., 2016b)

A comparison between SMS and 3D readout for different resolutions has been reported by (Huber et al., 2016b) and the results are shown in Fig. 31. SMS and 3D SS-SI-VASO acquisitions were performed at $3 \times 3 \times 3$ mm^3, $1.5 \times 1.5 \times 1.5$ mm^3 and $0.75 \times 0.75 \times 1.5$ mm^3 voxel sizes. The FOV, slice positioning and acceleration were optimized for each resolution, but kept the same for SMS and 3D.

The data are averaged across 7 participants for 240 VASO time steps. It can be observed that the temporal signal-to-noise ratio (tSNR) is higher for SMS EPI for voxel volumes above 1.3 µl, i. e., in the physiological noise dominated regime. Below 1.3 µl, however, 3D EPI outperforms SMS, indicating that it is a preferable technique in case of voxel sizes dominated by thermal noise. A feature of both tSNR curves is that they reach a plateau for increasing voxel volumes. This plateau is a result of physiological noise effects, as it cannot be seen in the SNR curve (Fig. 31), which is not showing a saturation of lower resolutions. From the SNR curve it can be seen that 3D EPI is dominating for all voxel volumes considered, again indicating the detrimental effects to that readout due to physiological artefacts.

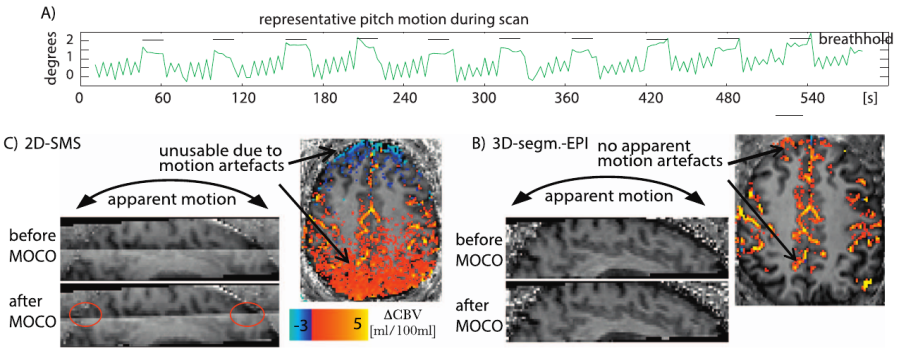

Figure 32: Motion artefacts in SMS VASO and 3D VASO. a) The pitch motion timecourse during the Valsalva maneuver task. The horizontal bars indicate the periods of breatholding. The sawtooth pattern between them reflects the fact that the breathing was paced and locked to the T_R. b) Effect of motion correction (MOCO) in segmented 3D EPI. The task-related activation can be disentangled from motion artefacts using retrospective motion correction. c) Effect of MOCO in 2D SMS EPI. Signal inhomogeneities along z result in discontinuous slice intensities. Motion correction interpolates the intensities and introduces strong artefacts. Picture from (Huber et al., 2016b)

Another point worth comparing between SMS and 3D is their susceptibility to motion artefacts. Huber et al. used a breathing task (Valsalva maneuver) in order to assess the effect of head motion. Fig. 32a shows a trace from the motion estimation routine of SPM. The pitch motion peaks corresponds to the intervals where the breathing task was performed, and they would corrupt the data if no retrospective motion correction is performed. The different inversion time across slices in SMS, resulting in different signal inhomogeneities, introduces artefacts in the reslicing procedure due to interpolation in the regions of intensity discontinuity (Fig. 32c) and hampers CBV quantification. For 3D EPI, the inversion time is the same for all slices and retrospective motion correction does not result in interpolation artefacts (Fig. 32b).

In conclusion, 3D SS-SI-VASO offers increased tSNR at submillimeter resolutions and less penalty due to motion artefacts with respect to its SMS counterpart and, hence, is preferable for layer dependent studies.

6

CALIBRATED FMRI

As described in Section 3.2, BOLD signal changes are an indirect measure of neuronal activity, and depend on relative changes in CBF, CBV and $CMRO_2$.
So, the BOLD response could be seen as the interaction of a vascular (CBF and CBV) and a neuronal ($CMRO_2$) component. Calibrated fMRI attempts to isolate the neuronal component by eliminating the vascular one, which usually require a CBF-sensitive scan and a breathing manipulation.
Calibrated fMRI has been validated at standard field strength and resolution, but faces challenges in high-field applications, due to the limited viability of CBF-sensitive techniques.

This Chapter reviews the mathematical formulation of the Davis model for calibration (Section 6.1.1) and explains the modifications that were done in this work in order to extend its applicability (Section 6.1.2).

6.1 THE DAVIS MODEL FOR CALIBRATION

6.1.1 *The Original Formulation*

Changes in dHb produce changes in extravascular R_2^*, which in turn give rise to GRE-BOLD signal changes.

Yablonskiy and Haacke derived the following analytical expression for R_2':

$$R_2' = \zeta \cdot \gamma \cdot \frac{4}{3} \cdot \pi \cdot \Delta\chi \cdot (1 - Y) \cdot B_0 \tag{60}$$

where ζ is the relative volume fraction of blood, γ is the gyromagnetic ratio, $\Delta\chi$ is the susceptibility difference between deoxygenated and oxygenated blood, and Y is the fraction of oxygenated blood (Yablonskiy and Haacke, 1994).
Changes in R_2^* give rise to BOLD signal changes. They can be expressed in a more compact form, where the dependency on venous CBV (CBV_v) and dHb is explicit (Blockley et al., 2013):

$$\Delta R_2^* = \kappa \cdot CBV_v \cdot [dHb]^\beta - \kappa \cdot CBV_{v,0} \cdot [dHb]_0^\beta \tag{61}$$

where κ is a constant that depends on vessel geometry, field strength, and $\Delta\chi$. The subscript '0' refers to the quantity at baseline and the exponent β depends on the diameter of the blood vessels (Blockley et al., 2013). It was estimated that $\beta = 1$ for larger vessels and $\beta =$

2 for capillaries (Ogawa et al., 1993). The baseline value of [dHb] depends on the baseline value of OEF and the haematocrit:

$$[\mathrm{dHb}]_0 \propto \mathrm{OEF}_0 \cdot \mathrm{Hct}. \tag{62}$$

The haematocrit represents the volume fraction of red blood cells in blood. It is usually ~ 40% in women and ~ 45% in men.
Signal changes in GRE-BOLD can be expressed as:

$$\frac{\Delta S}{S_0} = e^{-T_E \cdot \Delta R_2^*} - 1 \approx -T_E \cdot \Delta R_2^* \tag{63}$$

where it was assumed $T_E \cdot \Delta R_2^* \ll 1$. Substituting Eq. 61 into Eq. 63:

$$\frac{\Delta S}{S_0} = T_E \cdot \kappa \cdot \mathrm{CBV}_{v,o} \cdot [\mathrm{dHb}]_0^\beta \cdot \left[1 - \frac{\mathrm{CBV}_v}{\mathrm{CBV}_{v,0}} \left(\frac{[\mathrm{dHb}]}{[\mathrm{dHb}]_0}\right)^\beta\right]. \tag{64}$$

The calibration parameter (M) is introduced:

$$M := T_E \cdot \kappa \cdot \mathrm{CBV}_{v,o} \cdot [\mathrm{dHb}]_0^\beta \tag{65}$$

which is equal to the maximum BOLD signal change (ceiling effect), corresponding to a complete dHb washout from the vasculature, i. e., $[\mathrm{dHb}] = 0$ in Eq. 64.
Other assumptions are included in the model in order to relate Eq. 64 to quantities measurable with MRI techniques. The assumptions include:

- CBF and CBV are coupled via a power law relationship, i. e.,

$$\mathrm{CBV}_v = a \cdot \mathrm{CBF}^\alpha \quad \text{or} \quad \frac{\mathrm{CBV}_v}{\mathrm{CBV}_{v,0}} = \left(\frac{\mathrm{CBF}}{\mathrm{CBF}_0}\right)^\alpha \tag{66}$$

  where α is the Grubb exponent and is classically taken to be $\alpha = 0.38$ (Grubb et al., 1974).

- CMRO_2 follows Fick's principle, which states:

$$\mathrm{CMRO}_2 = \mathrm{CBF} \cdot 4[\mathrm{Hb}]_t \cdot (Y_a - Y_v) \tag{67}$$

  where the factor $4[\mathrm{Hb}]_t$ refers to the fact that each haemoglobin molecule can bind four oxygen molecules and $(Y_a - Y_v)$ is the difference between arterial and venous oxygen saturation values. It is related to the oxygen extraction fraction via:

$$\mathrm{OEF} = \frac{Y_a - Y_v}{Y_a} \approx Y_a - Y_v \approx 0.4 \tag{68}$$

  since $Y_a \approx 1$ and $Y_v \approx 0.6$.
  Defining $C_\alpha := 4[\mathrm{Hb}]_t$ and substituting in Eq. 67 together with Eq. 68, Fick's principle reads:

$$\mathrm{CMRO}_2 = C_\alpha \cdot \mathrm{CBF} \cdot \mathrm{OEF} \tag{69}$$

- The arterial compartment is fully oxygenated and, hence, dHb is only present in the venous vasculature. This allows to express the OEF as the ratio of [dHb]:

$$\frac{[\text{dHb}]}{[\text{dHb}]_0} = \frac{\text{OEF}}{\text{OEF}_0} \tag{70}$$

Combining Eqs. 70 and 69, the ratio of [dHb] can be rewritten as:

$$\frac{[\text{dHb}]}{[\text{dHb}]_0} = \frac{\text{CBF}_0}{\text{CBF}} \cdot \frac{\text{CMRO}_2}{\text{CMRO}_{2,0}}. \tag{71}$$

Substituting Eqs. 71, 66 and 65 into Eq. 64, the original formulation of the Davis model is obtained (Davis et al., 1998; Hoge et al., 1999):

$$\frac{\Delta S}{S_0} = M \cdot \left[1 - \left(\frac{\text{CBF}}{\text{CBF}_0}\right)^{\alpha-\beta} \cdot \left(\frac{\text{CMRO}_2}{\text{CMRO}_{2,0}}\right)^{\beta}\right] \tag{72}$$

which can be rewritten in a more compact notation upon substituting: $\Delta S/S_0 = \delta S$, $\text{CBF}/\text{CBF}_0 = f$ and $\text{CMRO}_2/\text{CMRO}_{2,0} = r$:

$$\delta S = M \cdot \left[1 - f^{\alpha-\beta} \cdot r^{\beta}\right]. \tag{73}$$

Eq. 73 isolates the component related to the oxygen metabolism from the CBF component, measurable with ASL. How the model is applied for calculation of CMRO_2 changes is reviewed in Section 6.1.3.

6.1.2 *The Modified Formulation*

VASO-fMRI has the potential to isolate CBV changes at submillimeter resolutions. In order to include it in the Davis model (Eq. 73), some substitutions need to be done.
Inverting Grubb's law (Eq. 66) to extract f as a function of $\nu_v = \text{CBV}_v/\text{CBV}_{v,0}$, i. e., $f = \nu_v^{1/\alpha}$, and substituting in Eq. 73, a formula for BOLD signal change depending on venous CBV changes is obtained:

$$\delta S = M \cdot \left[1 - (\nu_v)^{\frac{\alpha-\beta}{\alpha}} \cdot r^{\beta}\right]. \tag{74}$$

VASO is sensitive to total CBV changes (CBV_t), but Davis model considers exclusively venous CBV changes (CBV_v). In order to split CBV_t from CBV_v, it was assumed that the Grubb's power law (Eq. 66) holds true but with two different exponents. For total CBV, the classical $\alpha = 0.38$ is considered (Grubb et al., 1974):

$$\nu_t = f^{\alpha_t} = \left(\frac{\text{CBF}}{\text{CBF}_0}\right)^{\alpha_t} \quad \text{with} \quad \alpha_t = 0.38, \tag{75}$$

while, for venous CBV, an exponent of $\alpha = 0.2$ is taken from previous work (Chen and Pike, 2009):

$$v_v = f^{\alpha_v} = \left(\frac{CBF}{CBF_0}\right)^{\alpha_v} \quad \text{with} \quad \alpha_v = 0.2. \tag{76}$$

$\alpha = 0.2$ was observed to better reflect the flow-venous volume coupling during visual and somatosensory stimulation than the original Grubb exponent (Chen and Pike, 2009).
The quantities v_t and v_v refer to the values of CBV_t and CBV_v, respectively, normalized to their baseline.
Due to mass conservation, f is equal in the venous and total compartments. Therefore, Eqs. 75 and 76 can be combined to yield:

$$v_v = v_t^{\frac{\alpha_v}{\alpha_t}} \tag{77}$$

which expresses venous CBV (needed in the model) as a function of total CBV (obtainable with VASO).
Eq. 77 can be plugged into Eq. 74 to yield:

$$\delta S = M \cdot \left[1 - (v_t)^{\frac{\alpha_v - \beta}{\alpha_t}} \cdot r^{\beta}\right] \tag{78}$$

where the dependency with total CBV changes is made explicit.

6.1.3 *Extraction of $CMRO_2$ Changes*

Calibration involves the use of an iso-metabolic stimulus, i. e., a stimulus that is not eliciting any change in $CMRO_2$, in order to have a signal that has no neuronal component and allows the extraction of M from Eq. 73. In fact, for $r = 1$, Eqs. 73 and 78 take the forms, respectively:

$$\delta S_{hc} = M \cdot \left[1 - f_{hc}^{\alpha-\beta}\right] \quad \Rightarrow \quad M = \frac{\delta S_{hc}}{\left[1 - f_{hc}^{\alpha-\beta}\right]} \tag{79}$$

and

$$\delta S_{hc} = M \cdot \left[1 - (v_{t,hc})^{\frac{\alpha_v - \beta}{\alpha_t}}\right] \quad \Rightarrow \quad M = \frac{\delta S_{hc}}{\left[1 - (v_{t,hc})^{\frac{\alpha_v - \beta}{\alpha_t}}\right]} \tag{80}$$

where the subscript hc indicates hypercapnia, which is often taken as an iso-metabolic breathing challenge. The iso-metabolic assumption has been challenged by several works, and more details are devoted to this issue in Section 8.3.
M can then be used to extract r during a functional task (which will be denoted by the subscript $task$) involving metabolic changes. This is done by substituting Eq. 79 into 73:

$$\delta S_{task} = M \cdot \left[1 - f_{task}^{\alpha-\beta} \cdot r_{task}^{\beta}\right] = \frac{\delta S_{hc}}{\left[1 - f_{hc}^{\alpha-\beta}\right]} \cdot \left[1 - f_{task}^{\alpha-\beta} \cdot r_{task}^{\beta}\right]$$

(81)

and solving for r_{task}:

$$r_{task} = \left\{ \frac{1}{f_{task}^{\alpha-\beta}} - \frac{\delta S_{task}}{\delta S_{hc}} \cdot \frac{\left[1 - f_{hc}^{\alpha-\beta}\right]}{f_{task}^{\alpha-\beta}} \right\}^{-\beta} . \tag{82}$$

And, similarly, for Eq. 78:

$$r_{task} = \left\{ \frac{1}{(\nu_{t,task})^{\frac{\alpha_v-\beta}{\alpha_t}}} - \frac{\delta S_{task}}{\delta S_{hc}} \cdot \frac{\left[1 - (\nu_{t,hc})^{\frac{\alpha_v-\beta}{\alpha_t}}\right]}{(\nu_{t,task})^{\frac{\alpha_v-\beta}{\alpha_t}}} \right\}^{-\beta} . \tag{83}$$

The exponent β is taken to be ≈ 1 at 7 T (Kida et al., 2000; Martindale et al., 2008). VASO data can be used in the model, but baseline CBV needs to be assumed. In this work, a value of 5.5% was taken for the CBV_0 fraction with respect to the brain tissue volume in cerebral cortex (Lu and van Zijl, 2005).

6.1.4 *The Effect of Using CBV Instead of CBF in the Davis Model*

In the Davis model, the parameter having the largest impact on the estimated $CMRO_2$ changes is α_v, the venous coupling constant. In the standard application of calibrated BOLD experiments, CBF is measured, and the relatively small Grubb coupling constant down-scales the relatively large changes in measured CBF to relatively low changes of estimated CBV. However, if only CBV is measured for calibration of the BOLD effect, as in the present study, the small Grubb coupling constant up-scales the relatively small changes of measured CBV to large changes of estimated CBF. Consequently, estimated $CMRO_2$ changes are more affected by deviations in volume changes than deviations in flow changes. Hence, even small errors in measured CBV changes can have large effects on $CMRO_2$ estimates (see Fig. 33).

While this seems less than ideal, it should be noted that ASL provides good results for calibrated BOLD studies at conventional resolution (Hare et al., 2015), but its use is limited at high resolution (e.g., better than 2 mm isotropic) due to its relatively low CNR compared to BOLD, and at high field due to tagging limitations (Driver et al., 2012; Krieger et al., 2014a,b). VASO, on the other hand, has proven to provide a satisfactory SNR even at high fields and resolutions (Huber et al., 2015b, 2014a, 2015c), which opens the possibility of solving the Davis equation with CBV. The fact that the calculated $CMRO_2$ is more affected by errors in CBV is, therefore, compensated by the gain in SNR achieved by optimized VASO techniques with respect to current ASL results.

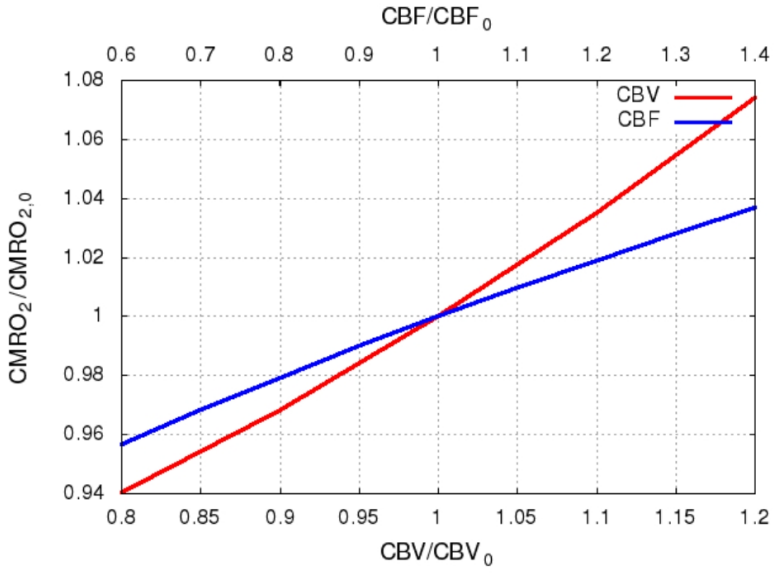

Figure 33: Errors in $CMRO_2$. The value of $CMRO_2$ can be obtained solving the Davis model as a function of $\nu = CBV/CBV_0$ or $f = CBF/CBF_0$. Red and blue solid lines indicate the relative error on $r = CMRO_2/CMRO_{2,0}$ that results from an error in the estimate of ν and f, respectively. The simulation shows that $CMRO_2$ is slightly more sensitive to errors in CBV (larger slope) compared to errors in CBF within a physiologically reasonable range. For example, overestimating the CBV change by 20% results in approximately 7% overestimation of $CMRO_2$ changes, while the same overestimation of CBF changes would only lead to an approximately 2% overestimation in $CMRO_2$. In both cases, the resulting bias in the $CMRO_2$ estimation is relatively low, when compared to the inter-subject variability of the experiment.

6.2 HYPERCAPNIA CALIBRATION

It was already mentioned that the isometabolic stimulus is often taken to be a breathing manipulation inducing hypercapnia. Hypercapnia is characterized by a vasodilation induced by a local pH change (acidosis) happening at the arterial smooth muscle and proportional to the increases in CO_2.
This has been generally achieved in two ways: either asking the participant to hold their breath, or administering a gas containing a higher CO_2 concentration than room air.

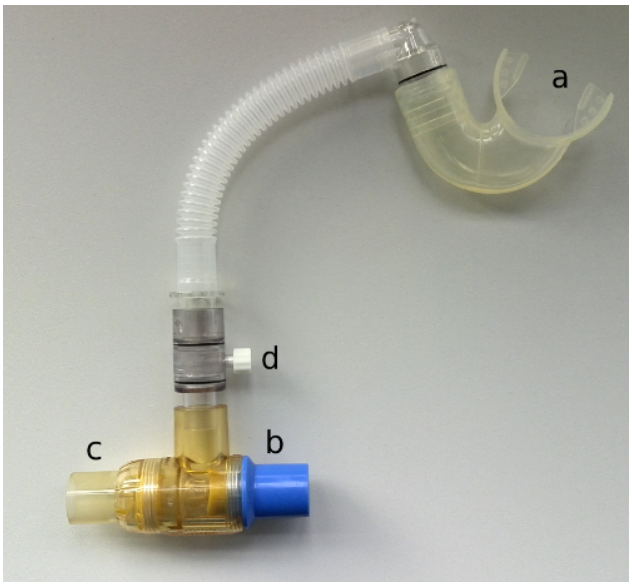

Figure 34: Mouth piece used for gas manipulation. (a) Part to be inserted in the mouth, through which the participant inhales and exhales. The participant also wears a nose clip in order to ensure that the inhalation and exhalation are through the mouth only. (b) Part to be connected to the inflow pipe; it is equipped with a one way valve, that opens only for inflowing gas. (c) Part to be connected to the outflow pipe; it is also equipped with a one way membrane, that opens only for outflowing gas. (d) Part to be connected to the sampling line, which goes to the BIOPAC modules.

Breath hold has several disadvantages, including: increased participant movement, difficulty to control for, and lower levels of vessel dilation. In this work, we used a gas delivery system for administering a gas mixture containing 5% CO_2, 21% O_2 and 74% N_2.

Safety

All procedures were approved by the ethics committee of the University of Leipzig, and experiments involving gas administration had to be performed under the supervision of a physician, who was monitoring the participant's heart beat, respiration, end-tidal partial pressure of carbon dioxide ($P_{ET}CO_2$) and end-tidal partial pressure of oxygen ($P_{ET}O_2$). The gas administration never exceeded 10 min, and the total time of the experiment was kept shorter than 60 min. A gas

mixture containing 5% of CO_2 balanced with room air is considered to elicit mild hypercapnia, and all participants tolerated it well.

Setup

The experimental setup for the gas delivery system and sampling consists of four main parts:

- Gas bottles containing premixed gases.
- A valve placed at the wall of the scanner room in order to open and regulate the gas flow.
- A mouth piece (Fig. 34) worn by the participant and connected via a pipe to the gas wall socket.
- A BIOPAC sampling system for $P_{ET}O_2$ and $P_{ET}CO_2$ recordings.

Effect on signal changes

Hypercapnia elicits a general vessel dilation. This means that CBF and CBV increase, and there is a positive signal change in BOLD and a negative (CBV increase) in VASO data (Fig. 35). Since vessels are more dense in gray matter, most of the signal changes is found in the cortex, and can reach values up to 7% for BOLD and 3% for VASO (own data, see Chapter 8). For mild hypercapnia, changes in CBF are expected to be in the order of 50%, and the venous oxygenation to increase by 26%. Moreover, end-tidal pressure values of carbon dioxide increase from 40 mmHg during normocapnia to 50 mmHg during hypercapnia (Xu et al., 2011).

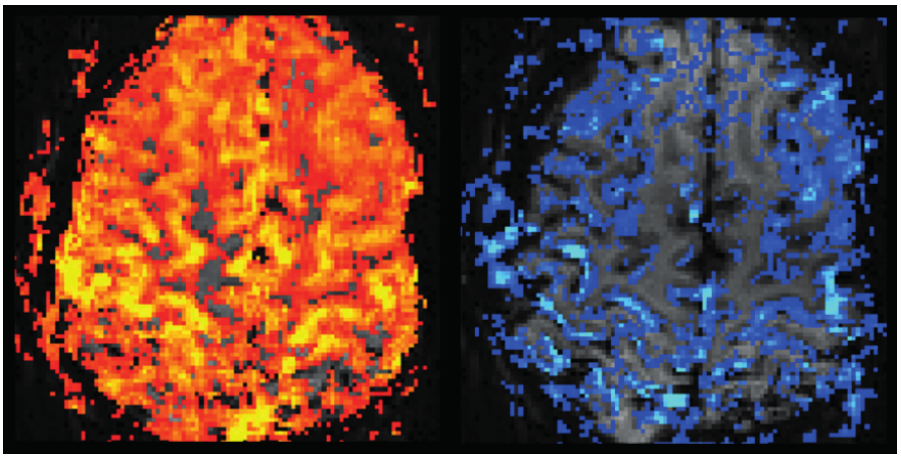

Figure 35: Hypercapnia-induced effects on Z-stat maps, for a block-design paradigm. BOLD is shown on the left and VASO on the right. The signal changes are spread all over gray matter.

Isometabolic assumption

Although the model considers $r = 1$ for hypercapnia stimulation, whether changes in CBF and CBV during hypercapnia are or are not accompanied by changes in $CMRO_2$ is a matter of debate (Bulte et al., 2012; Pike, 2012; Xu et al., 2011). In fact, there is evidence that mild hypercapnia elicits a significant suppression of $CMRO_2$ (Xu et al., 2011; Zappe et al., 2008). For example, Xu et al. report a reduction of $(13.4 \pm 2.3)\%$ in $CMRO_2$ in humans. Griffeth and Buxton simulated

the effect of $r \neq 1$ on $CMRO_2$ estimates, and found that the deviation would be $\sim 20\%$ for $r = 0.9$ for standard CBF values and CBF-$CMRO_2$ coupling (Fig 36, green trace). This variation is, in our experiments, smaller than the inter-participant variability (see Section 8.4).

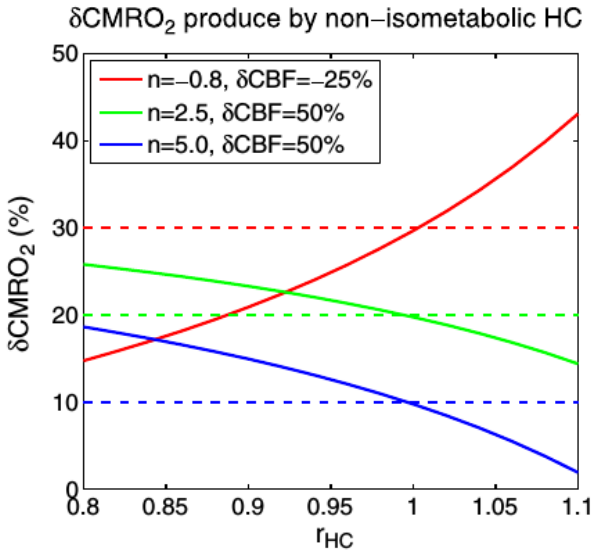

Figure 36: Dashed lines: $CMRO_2$ estimations for 3 different values of CBV and n ($n = (f-1)/(r-1)$). Continuous lines: deviation from the $CMRO_2$ values in case hypercapnia is non-isometabolic. Adapted from (Griffeth and Buxton, 2011).

6.3 MODEL ASSUMPTIONS

The simple, compact form of BOLD signal changes provided by the Davis model (Eq. 79) is the result of several assumptions and approximations. It is therefore necessary to evaluate their impact on the $CMRO_2$ estimation.

α and β exponents

The α exponent describes the coupling between functional changes in CBV and CBF. In the original formulation of the Davis model, blood volume changes were considered to be uniform in all compartments, without any differentiation between arteries, capillaries and veins. It has been shown, though, that different compartments have significantly different CBV responses upon the same CBF change (Chen and Pike, 2009; Stefanovic et al., 2008). In order to account for this effect, we took two different α values: α_t and α_v, for total and venous CBV, repectively (Eqs. 75 and 76).

The β exponent relates oxygenation changes to R_2^* changes (Eq. 61). It depends on vessel size as well as on field strength. This dependency comes about from the fact that changes in R_2^* around smaller vessels are lower as compared to larger vessel due to diffusion effects (Buxton, 2013). For routine field strengths, such as 3 T, $\beta = 1$ for large veins and $\beta = 2$ for capillaries (Ogawa et al., 1993), so an average

value of $\beta = 1.5$ has usually been taken. It has been shown that, due to decreasing intravascular contribution for increasing B_0 (Uludag et al., 2009), the relationship between changes in R_2^* and changes in dHb becomes linear and, thus, $\beta \approx 1$ (Kida et al., 2000; Martindale et al., 2008).

In order to assess the effect of the choice of the model parameters, depth-dependent profiles for $CMRO_2$, M, and normalized BOLD were evaluated for a range of α and β values (Fig. 37). Such profiles are the result of the application of the Davis model for the calibration of a finger tapping task with hypercapnia, and refer to the hand motor region of 10 subjects (more on this in Chapter 8). While keeping the other parameters fixed, α_v, α_t and β were varied once at the time in physiologically reasonable ranges (Griffeth and Buxton, 2011). In particular, the lowest and the highest boundaries of the chosen ranges were evaluated. It can be seen that the qualitative shape of the profiles is very similar for a wide range of α and β values. The choice of the parameters is primarily leading to a scaling effect.

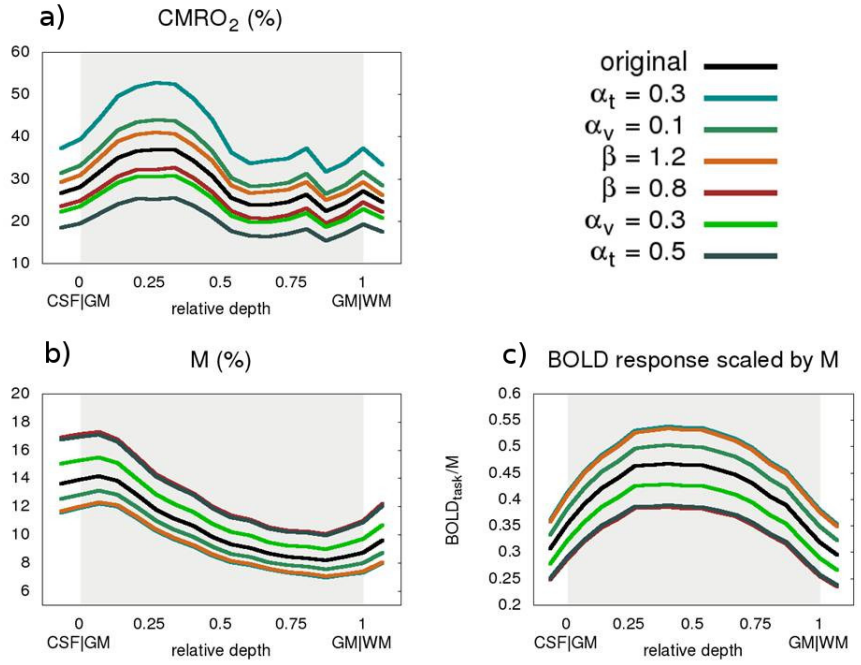

Figure 37: Effect of α and β variation in the Davis model estimates. Data are taken from the M1 region of 10 participants and averaged. The task involved a finger tapping paradigm and breathing manipulation in order to apply Davis model. Depth-dependent (a) $CMRO_2$ changes (b) M and (c) normalized task BOLD response (scaled by M), evaluated for a range of α_t, α_v and β values (color coded). Varying the exponents has an effect on the amplitude of the three quantities considered, but does not affect their shape.

Resting CBV

The value of resting CBV needs to be assumed in order to estimate v_t from VASO data. In our study, $CBV_0 = 0.055$ was used (Lu and van Zijl, 2005; Rostrup et al., 2005). Although this value is accurate

for GM and, thus, for voxel sizes on the order of the cortex thickness, where different local CBV_0 are averaged together, it is likely not to be valid for higher resolution, due to the high blood fraction at the pial surface (as described in Chapter 4). To quantitate this cortical variation, CBV_0 was calculated from a MION slice in the rat cortex (Fig. 38). It can be seen that resting CBV is markedly varying from the surface towards white matter (WM) in a linear way, if the uppermost values are excluded. To test the impact of this potential gradual variation of CBV_0 with cortical depth, profiles of CBV_t and CBV_v (obtained using Eq. 77) with different assumed CBV_0 distributions were calculated and are shown in Fig. 39. The underlying VASO data used are taken from an experiment involving a block design finger tapping. If CBV_0 is underestimated at the cortical surface, then CBV changes are overestimated, leading to a different depth-dependent profile. For the CBV_0 considered, the overestimation is $\sim 60\%$ for the superficial laminae. Therefore, an accurate knowledge of CBV_0 distribution would allow a marked improvement in the accuracy of ΔCBV estimation, especially in regions with higher vascular density.

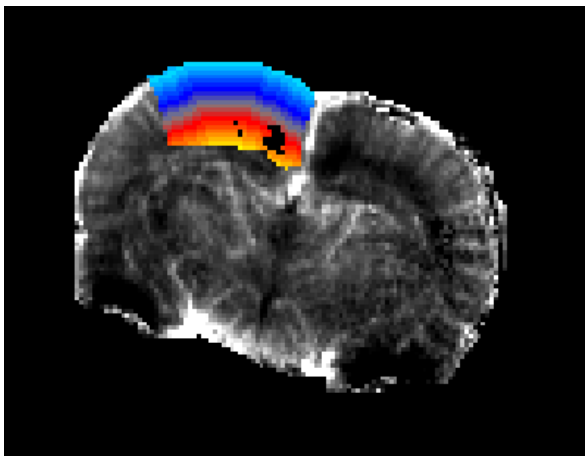

(a)

# layer	CBV_rest
0	0.0936365
1	0.0905411
2	0.0608847
3	0.0492111
4	0.0388432
5	0.0293665
6	0.025552
7	0.0222149
8	0.0194016
9	0.0176434
10	0.0140472
11	0.0114473
12	0.0109233
13	0.00833379
14	0.00699135
15	0.00604303
16	0.00610992

(b)

Figure 38: Resting CBV in the rat cortex. (a) A MION slice highlighting the region of interest, with color-encoded equidistant laminae. (b) Extracted values of resting CBV; the uppermost laminae show distinctly high values. The underlying MION image is a courtesy of Dr. Laurentius Huber.

Finally, Davis model assumes that the signal changes come from the extravascular compartment only (intravascular signal changes are neglected), volume exchange effects between blood and tissue are neglected, and the CBF-CBV coupling is assumed to be the same for a task and for hypercapnia. All of these assumptions might be oversimplifications. Therefore, Griffeth and Buxton analyzed the impact of these approximations by comparing the Davis model with a detailed, four-compartment model. They found that Davis model is able to

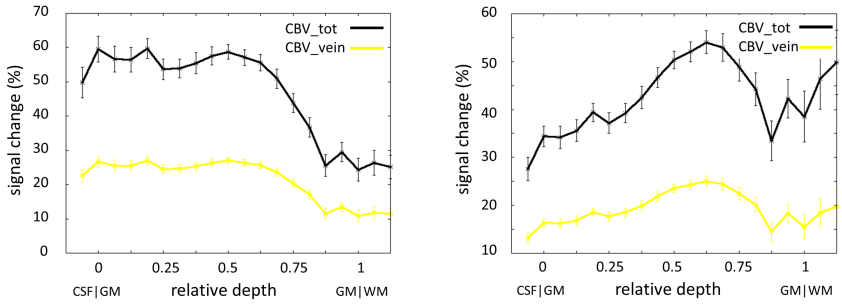

Figure 39: Depth dependent total (black) and venous (yellow) CBV changes induced by finger tapping in the motor cortex. A relative depth 0 corresponds to the border between CSF and GM, and 1 to the border between GM and WM. (a) CBV changes calculated assuming a constant $CBV_0 = 0.055$. (b) CBV changes calculated assuming a varying CBV_0, linearly descreasing from $CBV_0 = 0.095$ to $CBV_0 = 0.0285$. It can be seen that the assumption of a constant CBV_0, if proven to be wrong, would lead to an overestimation of the volume changes at the surface.

give reliable $CMRO_2$ estimates for standard CBF-$CMRO_2$ coupling values (Griffeth and Buxton, 2011).

7

VASCULAR REACTIVITY INDICES FROM RESTING-STATE FMRI DATA

The vascular term in the BOLD response follows the baseline venous CBV and oxygenation and is, thus, spatially unspecific. Chapter 6 presented a model that makes the dependency of BOLD on CBV, CBF and $CMRO_2$ explicit. The model requires an additional functional contrast and a breathing manipulation in order to be solved.
Another way of accounting for the cerebrovascular reactivity (CVR) component is a normalization of a task-induced (vascular and neuronal) BOLD response by a purely vascular response. The vascular response can be induced by a gas or breathing manipulation (Davis et al., 1998), but more recent observations suggest that it could be contained in the low frequency band of the resting-state BOLD responses (Biswal et al., 2007).

Despite the initial excitement, resting-state based methods for signal normalization did not really take off, with most of the calibrated BOLD studies still relying on gas manipulation or breath-hold scans. This might be due to the fact that resting-state normalization does not deliver a well defined physiological quantity. Moreover, several different methods have been proposed and most of them are missing a clear validation. Given that the band of interest is the low-frequency one, disentangling the neuronal contribution from the vascular contribution is not straightforward, and represents one of the biggest impediments to the use of resting-state fluctuations as a scaling factor (Lipp et al., 2015; Liu, 2013). Moreover, the choice of the T_R has an impact on the amount of aliased cardiac and respiration frequencies into the low-frequency band (Viessmann et al., 2016; Wise et al., 2004).

So far, these methods have only been applied at low spatial resolutions and their applicability at higher resolutions has not yet been investigated. The increase in resolution does not only mean lower sensitivity, but could affect the interpretation of the BOLD signal because the traditional neurovascular coupling assumptions might not be valid (Goense et al., 2012).

Apart from replacing hypercapnia challenges for scaling purposes, a characterization of resting-state BOLD signal fluctuations has an additional interest. That is, a frequency analysis of BOLD responses at submillimeter resolution might shed light on the noise distribution and on the frequencies relevant for neural activity.
Resting-state fluctuations of neuronal origin occur in a sub-second time scale (Ma et al., 2016). The time course of the HRF, however,

limits the detectability of neurally-driven BOLD oscillations to a restricted frequency range. This range has been typically taken to be 0.01-0.1 Hz for resting-state fMRI studies (Biswal et al., 1995), but neurally-driven fMRI signal oscillations have recently been observed at frequencies higher than 0.1 Hz, up to at least 0.75 Hz, and at amplitudes larger than the ones predicted by the canonical linear models (Lewis et al., 2016). Therefore, it is not completely clear what the meaningful frequency band for resting-state studies would be (Boubela et al., 2013; Yan et al., 2009).

Section 7.1 reviews some measures that have been proposed as indicators of CVR: resting-state fluctuation amplitude (RSFA), obtained from the time domain of spontaneous BOLD fluctuations, and introduced by Kannurpatti and Biswal (Kannurpatti and Biswal, 2008); amplitude of low-frequency fluctuations (ALFF) and fractional amplitude of low-frequency fluctuations (fALFF), indices derived from power spectra (Zang et al., 2007; Zou et al., 2008); fractional fluctuation amplitude (fFA), used to characterize the power in a certain frequency band. Section 7.2 describes the noise sources present in fMRI datasets and some strategies to reduce them.

7.1 CEREBROVASCULAR REACTIVITY

CVR is defined as the change is CBF upon a vasodilatory or vasoconstrictive stimulus:

$$\mathrm{CVR} = \frac{\Delta \mathrm{CBF}}{\Delta \mathrm{P_aCO_2}}, \tag{84}$$

where $\mathrm{P_aCO_2}$ is the arterial partial pressure of carbon dioxide.
CVR has been measured with perfusion-sensitive MR techniques, such as ASL and BOLD, during controlled change in $\mathrm{P_{ET}CO_2}$ induced by a gas manipulation or a breath holding task (Fierstra et al., 2013).

The resting-state BOLD (or rs-fMRI) signal, i. e., the signal acquired over a period of time in which the participant is neither actively performing any task nor sleeping, was shown to be driven by resting fluctuations in arterial $\mathrm{CO_2}$ levels (Wise et al., 2004). In light of this, it is tempting to use resting-state fluctations as proxy for CVR.
Several studies have extracted CVR-related quantities from rs-fMRI timecourses and showed their applicability in fMRI calibration. However, resting BOLD signal fluctuations are driven by other physiological and neuronal modulators (spontaneous neural activity, breathing, heart beath, Mayer waves, etc.), that also show cyclic features and can represent a confound.

7.1.1 *Resting-State Fluctuation Amplitude*

Kannurpatti and Biswal define RSFA as the temporal standard deviation (tSD) of the unfiltered resting-state timeseries (Fig. 40), and they

hypothesize it to be an indicator of arterial CO_2 variations (Kannurpatti and Biswal, 2008).

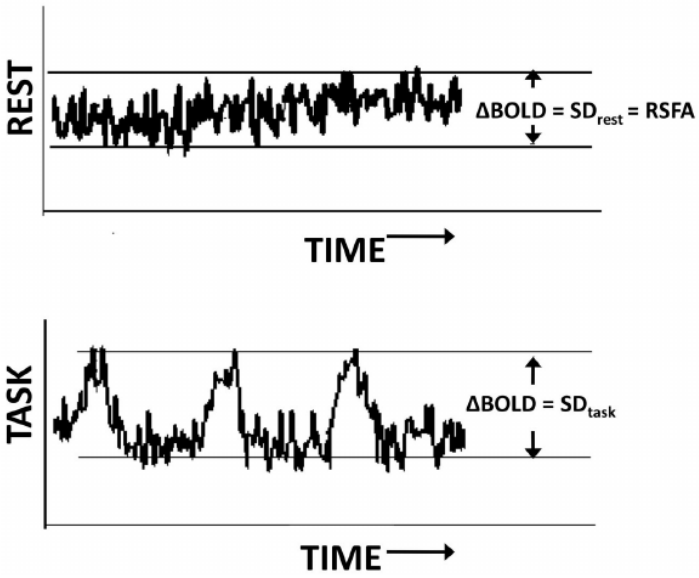

Figure 40: Graphical representation of RSFA estimation (top) and amplitude of the task timecourse (bottom). Picture from (Kannurpatti et al., 2012).

The use of RSFA as an index for vascular reactivity was validated by using it for scaling the BOLD response induced by a motor task, and comparing the results with a hypercapnia-based normalization. They used a GRE-EPI sequence with a voxel size of $3 \times 3 \times 7$ mm^3. A high correlation between RSFA and the hypercapnia induced response was observed across voxels (Fig. 41), as well as an 80% reduction in motor task response variability (Kannurpatti and Biswal, 2008).

7.1.2 *(Fractional) Amplitude of Low-Frequency Fluctuations*

ALFF are considered in several studies (Biswal et al., 1995; Kiviniemi et al., 2000; Zang et al., 2007).
Zang et al. define it as the power in the band 0.01-0.08 Hz of resting-state BOLD signal variations divided by the global mean in the brain (Fig. 42) and they use it as a marker in the context of diseased population studies (ADHD versus healthy participants).

Defined that way, however, higher ALFF can be found not only in regions of higher vascular sensitivity or neural activity, but also in regions where noise level is higher. Therefore Zou et al. introduced an improved index, called fALFF, in which ALFF is normalized by the square root of the power in the whole frequency range sampled, which was 0-0.25 Hz in their study. They reported higher fALFF values in region corresponding to the default mode network, and de-

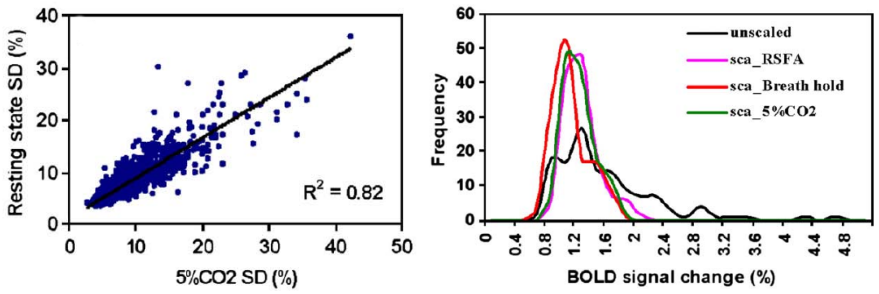

(a) (b)

Figure 41: Validation of RSFA as a scaling factor. (a) Correlation between resting-state tSD (RSFA) and tSD of the timecourse involving hypercapnia. (b) Effect of normalization of the motor task response (fingertapping) with different factors. Unscaled refers to the original timecourse, while sca_RSFA, sca_Breath hold and sca_5%CO_2 to the normalization using RSFA, breath hold and gas-induced hypercapnia respectively. The distribution of the scaled signal changes is very similar for all the normalizations considered, and is narrower than the unscaled distribution. Adapted from (Kannurpatti and Biswal, 2008).

creased fALFF in non-specific regions, such as cisterns and ventricles, where ALFF would be high due to strong physiological noise variations.

7.1.3 *Fractional Fluctuation Amplitude*

The fractional fluctuation amplitude was introduced in this work in order to extend the study of BOLD fluctuations. The definition is very similar to fALFF, with the difference that it also includes higher frequency bands, and is scaled by a portion of the whole power spectrum. The scaling band is, in this study, 0.4-0.5 Hz, which is least affected by physiological noise peaks.

fFA is not introduced with the assumption of being a neuronal or CVR indicator. It is rather a marker for the study of frequency distribution and characteristics across the cortex (see Chapter 10).

7.2 NOISE IN FMRI

The driving function of the above mentioned resting-state fluctuations is controversial. Some studies claim the considered frequency range to be indicative of arterial CO_2 fluctuations (Kannurpatti and Biswal, 2008), others of intensity of neuronal activity (Zang et al., 2007). Recently, Ma et al. showed that spontaneous neural activity is predictive of brain hemodynamics in mice, indicating that hemodynamic fluctuations are neural in origin (Ma et al., 2016).

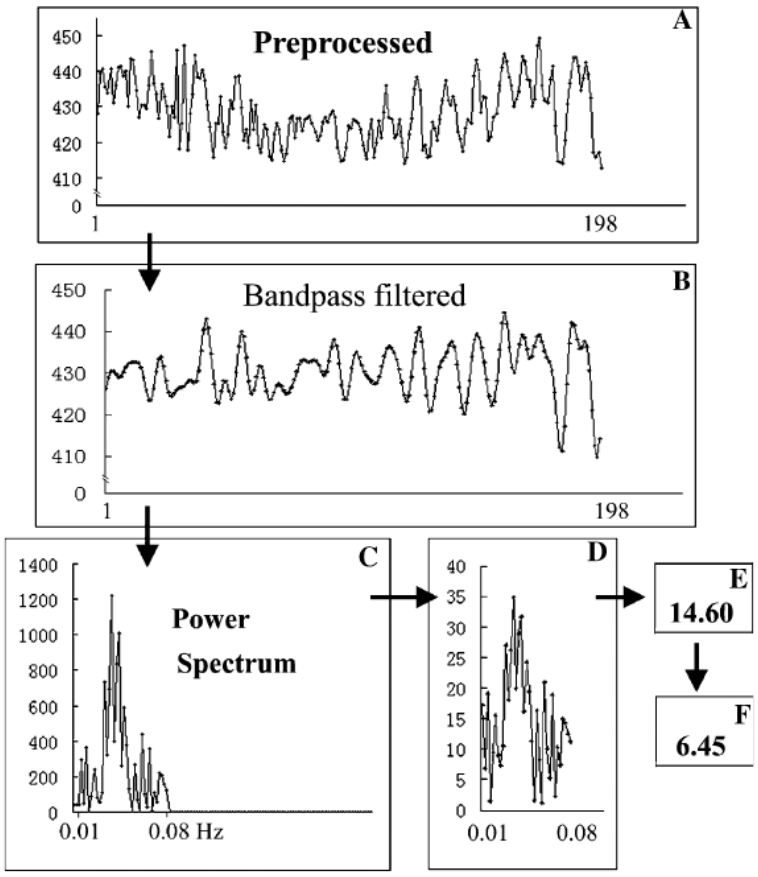

Figure 42: Graphical representation of ALFF estimation. (a) BOLD timecourse following preprocessing. (b) Bandpass filtered timecourse (the band 0.01-0.08 Hz is retained). (c) Power spectrum obtained with fast Fourier transform. (d) ALFF, i. e., the square root of the power spectrum in the band 0.01-0.08 Hz. (e) Averaged ALFF across 0.01-0.08 Hz. (f) Normalized ALFF (divided by the global mean of the brain mask). Picture from (Zang et al., 2007).

Nevertheless, noise plays an important role in resting-state fMRI and needs to be characterized before taking any conclusion on the nature of the observed oscillations (Bright and Murphy, 2015).

7.2.1 *Noise Characteristics*

A relevant quantity in fMRI is the temporal signal-to-noise ratio, tSNR. Obvious ways to improving it are increasing the available signal and/or reducing the noise level.
tSNR is defined as:

$$\text{tSNR} = \frac{\bar{S}}{\sigma} \tag{85}$$

where $\bar{S}$ is the temporal mean signal intensity and σ is the temporal standard deviation of the noise.

Assuming the noise sources to be uncorrelated, the noise can be written as:

$$\sigma = \sqrt{\sigma_T^2 + \sigma_S^2 + \sigma_P^2} \tag{86}$$

where σ_T represent thermal noise contributions (both from the scanner and the subject), σ_S the system noise due to drifting and hardware imperfections, and σ_P the physiological noise contributions, coming from the cardiorespiratory and metabolic subject dynamics.

Thermal noise

Non physiological terms can be grouped together (Krüger et al., 2001):

$$\sigma_0^2 := \sigma_T^2 + \sigma_S^2 \tag{87}$$

where σ_0 is the image noise, containing contribution from σ_T and σ_S. The SNR of a single image (SNR_0) can thus be written as:

$$SNR_0 = \frac{\bar{S}}{\sigma_0}. \tag{88}$$

Physiological noise

The physiological noise, on the other hand, can be split into two components (Krüger and Glover, 2001):

$$\sigma_P^2 = \sigma_B^2 + \sigma_{NB}^2 \tag{89}$$

where σ_B is BOLD-like noise and σ_{NB} non-BOLD noise:

$$\begin{aligned} \sigma_B &= c_1 \cdot \Delta R_2^* \cdot T_E \cdot S \\ \sigma_{NB} &= c_2 \cdot S \end{aligned} \tag{90}$$

with c_1 and c_2 being proportionality constants.
Defining:

$$\lambda^2 := (c_1 \cdot \Delta R_2^* \cdot T_E)^2 + c_2^2 \tag{91}$$

and substituting it, together with Eq. 87 into Eq. 85, yields:

$$tSNR = \frac{SNR_0}{\sqrt{1 + \lambda^2 \cdot SNR_0^2}}. \tag{92}$$

Eq. 92 gives a relationship between the image SNR and the temporal SNR. It can be observed that tSNR cannot increase indefinitely, and its maximal value depends on λ. Indeed, the asymptotic value of tSNR, $tSNR_L$, is:

$$tSNR_L \to \frac{1}{\lambda} \qquad \text{for} \quad SNR_0 \to \infty. \tag{93}$$

Voxel volume and field strength dependence

Eq. 92 can be rewritten as a function of voxel volume (V), assuming a direct proportionality of V with SNR_0 (with proportionality constant a):

$$tSNR = \frac{a \cdot V}{\sqrt{1 + (\lambda \cdot a \cdot V)^2}}. \tag{94}$$

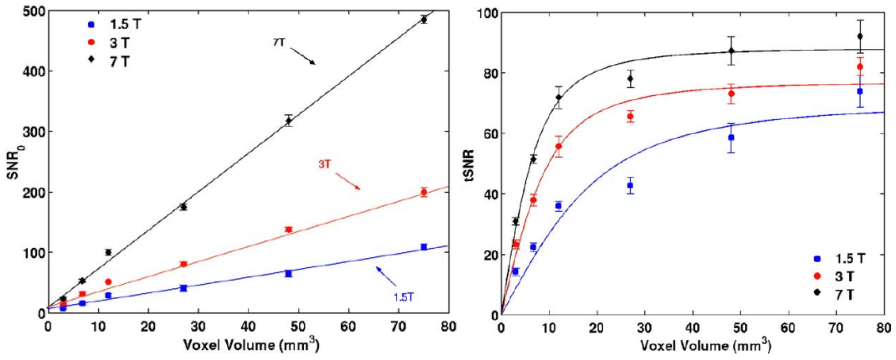

(a) (b)

Figure 43: (a) SNR_0 and (b) tSNR as a function of voxel volume for B_0 of 1.5 T (blue), 3 T (red) and 7 T (black). SNR_0 increases linearly with V, while tSNR reaches a plateau due to physiological noise contributions ($tSNR_L = 1/\lambda$). Adapted from (Triantafyllou et al., 2005).

The relationship between signal-to-noise ratio and voxel volume is reported in Fig. 43.

Fig. 43 also shows the SNR-B_0 dependency. SNR_0 increases linearly with B_0, due to the fact that $S \propto B_0^2$ and $\sigma_0 \propto B_0$. Physiological contributions depend on the signal intensity (Eq. 89) and, thus, $\sigma_P \propto B_0^2$. For this reason, moving to higher fields can result in a limited tSNR gain.

Physiological to thermal noise ratio

In order to determine which type of noise is dominant, it is useful to estimate the ratio of physiological to thermal noise. It can be calculated as a function of tSNR and SNR_0, combining Eqs. 85, 86, 87 and 88 (Triantafyllou et al., 2005):

$$\frac{\sigma_P}{\sigma_0} = \sqrt{\left(\frac{SNR_0}{tSNR}\right)^2 - 1}. \tag{95}$$

Eq. 95 increases linearly with B_0. Triantafyllou et al. found that, at standard resolutions of $3 \times 3 \times 3$ mm^3, the tSNR at 7 T is limited by σ_P ($\sigma_P/\sigma_0 = 2.2$ at 7 T and $\sigma_P/\sigma_0 = 0.9$ at 3 T) and gives a moderate increase in tSNR (tSNR $\approx$ 78 at 7 T versus tSNR $\approx$ 66 at 3 T) (Triantafyllou et al., 2005). Qualitatively, this effect can be seen in Fig. 43b in the fact that the black curve (7 T) reaches its asymptotic value for smaller voxel volumes than the blue curve (1.5 T).

Going to higher resolutions, relative tSNR benefits become larger. For a voxel size of $1 \times 1 \times 3$ mm^3, tSNR = 31 at 7 T (with a ratio $\sigma_P/\sigma_0 = 0.9$), while tSNR = 23 at 3 T (with a ratio $\sigma_P/\sigma_0 = 0.6$).

Bodurka et al. extend this analysis by defining the ideal voxel volume as the one where the variance in physiological noise matches the variance in thermal noise ($\sigma_P^2 = \sigma_0^2$). If $\sigma_P/\sigma_0 > 1$, then, increasing image

SNR does not improve timecourse SNR sensibly. This gives the ideal SNR values to be (Bodurka et al., 2007):

$$\mathrm{SNR}_0(\sigma_P = \sigma_0) = \mathrm{tSNR}_L \quad \text{and} \quad \mathrm{tSNR}(\sigma_P = \sigma_0) = \frac{\mathrm{tSNR}_L}{\sqrt{2}}. \quad (96)$$

They found the ideal voxel volume to be $(1.8\ \mathrm{mm})^3$ for gray matter at 3 T.

Another important issue in fMRI is relating the effect size to the voxel volume and scan duration. Due to the nonlinearity of that relationship, at resolutions of about 1 mm at 3 T, for example, if tSNR is halved, then the scan duration needs a 4-fold increase for detection of a 1% effect size (Murphy et al., 2007). The number of required timepoints (N) for reliably detecting the effect is (Murphy et al., 2007):

$$N = \frac{2}{R_{act}(1 - R_{act})} \left(\frac{\mathrm{erfc}^{-1}(P)}{\mathrm{tSNR} \cdot \mathrm{eff}} \right)^2 \quad (97)$$

where R_{act} represents the ratio of ON periods over OFF periods, erfc^{-1} is the inverse complementary error function, P is the significance level for detection and eff is the effect size (in percent).

Finally, in case multi-channel array coils are available and parallel imaging is employed, further noise is added to the image (as described in Section 5.2). However, if tSNR is close to its asymptotic limit, reductions in SNR_0 result in limited penalty (De Zwart et al., 2002). Triantafyllou et al. found that the relationship $\sigma_P = \lambda S$ holds true also for accelerated images, and that the σ_0 contribution increases as the acceleration factor increases (Triantafyllou et al., 2011).

7.2.2 *Residual Noise Reduction Strategies*

Even optimized sequences are affected by residual noise, and some strategies to reduce it can be employed.

Fig. 44 shows the power spectra for a BOLD timecourse (red) acquired with T_R= 328 ms, respiratory recording (green) and cardiac recording (blue) acquired at 1 kHz (Viessmann et al., 2016). Peak BOLD power can be observed at very low frequencies, and at higher ones, corresponding to the central cardiac and respiratory peaks.

The low-frequency component of the spectrum has a pink noise shape, i. e., decreases as $1/f$ (where f is the frequency), while higher frequencies have a white noise shape, except for the respiratory and cardiac peaks. Those are typical features for fMRI spectra.

The $1/f$ component is due to metabolic drifts and scanner instabilities. It is generally removed by filtering, so it is important that the response of interest does not fall into that frequency range, if block design paradigms are used.

The white noise component is due to thermal noise effects, both from

scanner and subject. Aliased cardiorespiratory components can also contribute to wideband noise.

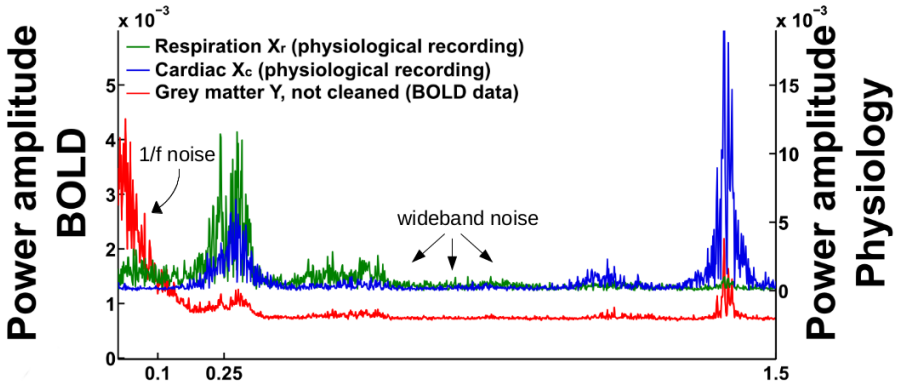

Figure 44: BOLD (red), respiratory (green) and cardiac (blue) power spectra. The BOLD spectrum is uncorrected, and some typical features can be observed: the $1/f$ (with f being the frequency) trend, and the peaks corresponding to the central cardiac and respiratory frequencies. Above approximately 0.1 Hz, the noise has a white shape, and it is indicated here as wideband noise. Adapted from (Viessmann et al., 2016).

Signal drift

Typically, fMRI timecourses are affected by scanner drifts, which is visible in the data as a slow baseline change. Since most of its power is localized at frequencies < 0.01 Hz, a highpass filter can be used to eliminate it. For lenghty acquisitions, higher order baseline drifts corrections might be needed.

Head motion

Head motion represents another confounding effect in fMRI. It can be retrospectively corrected for (usual a rigid body transformation with 6 degree of freedom is used for the purpose), or prospectively with the aid of additional hardware (Zaitsev et al., 2017).

Physiological noise

Physiological noise correction usually requires recording of the cardiac and respiratory traces and retrospective correction.
Alternatively, if the T_R is short enough ($< 500ms$), notch filtering could be used. The results, however, are often suboptimal because frequencies associated to cardiac and respiratory cycles can extend over a band whose width may be difficult to accurately define.
Anyways, since the T_R for most fMRI experiments is in the order of 1-3 s, several physiological events are undersampled. One of them is the cardiac cycle, which happens at a frequency of about 1 Hz.
The alias frequency is defined by $f_{alias}(n) = |f - n \cdot f_s|$, where $f = f_{alias}(0)$ is the true frequency of interest, f_s is the sampling frequency and $n \in \mathbb{N}$.
Fig. 45 shows how the cardiac frequency is aliased into lower frequencies if undersampled.

RETROICOR has been proposed for removing cardiorespiratory artefacts. It is an image-based, retrospective physiological noise correction for fMRI datasets (Glover et al., 2000). Cardiac and respiratory

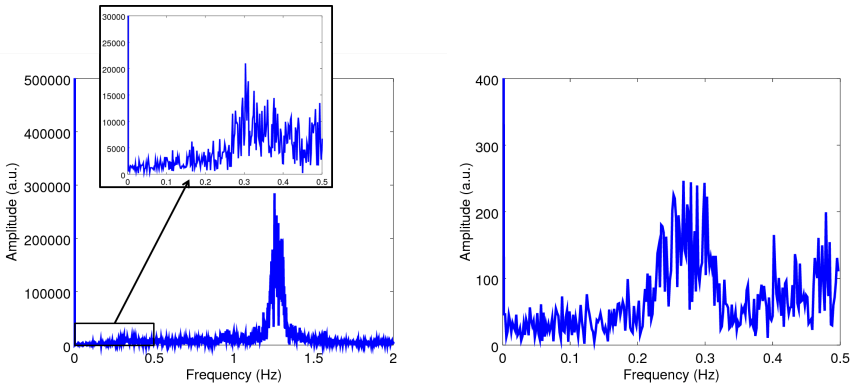

(a) (b)

Figure 45: (a) Fully sampled (1 ms) cardiac trace of one participant, with an inset showing the range 0-0.5 Hz. (b) Undersampled (1 s) version of the same cardiac trace. It can be observed how the peak is mapped into lower frequencies.

traces need to be recorded with external devices during the fMRI session, and then fed into the algorithm. The fluctuations are modeled as low-order Fourier series and then regressed out of the data.
The phase of the cardiac and respiratory cycles are calculated in two different ways, the former as a difference between the MR acquisition time and the previous peak, the latter using a histogram-equalized method in order to include the full waveform of the signal (Caballero-Gaudes and Reynolds, 2016).
Other ways of reducing physiological noise artefacts include triggering or gating, where the acquisition is synchronized to the physiological event (for example, pulse or inspiration), or pacing subject's respiration.

An additional strategy for getting rid of physiological noise is selecting the frequency of interest (if known) and excluding the remaining frequencies. For example, Liu et al. found the frequency band 0.02-0.04 Hz to be the best indicator of CVR, and use exclusively that one for their analysis (Liu et al., 2017).

Part IV

RESULTS

8

LAMINA-DEPENDENT CALIBRATED BOLD RESPONSE

The model introduced in Chapter 6 has the potential for estimating $CMRO_2$ at high resolution.
In this Chapter, the applicability of the model is demonstrated by calibrating a motor task with a breathing task. Another way of normalizing BOLD signal changes, which involves scaling the task-induced signal changes (Eq. 78) by the hypercapnia-induced signal changes, is investigated. This procedure also eliminates the purely vascular component from the BOLD response and, hence, should be more specific to the site of activation rather than being biased to the regions of large baseline blood volume (Cohen et al., 2004). The study is performed at a submillimeter resolution in order to obtain depth-dependent $CMRO_2$ estimates. Previous works have studied $CMRO_2$ on a layer-dependent levels in animals (Bohraus et al., 2011; Herman et al., 2013; Shen et al., 2008). The current work represents, to our knowledge, the first attempt in estimating depth-dependent $CMRO_2$ in humans.

Results from this study have been presented at the 23rd meeting of the International Society for Magnetic Resonance in Medicine in Toronto, Ontario, Canada, with the title "Layer-Dependent Calibrated BOLD Response in Human M1" (Guidi et al., 2015) and later published in NeuroImage with the title "Lamina-dependent calibrated BOLD response in human primary motor cortex" (Guidi et al., 2016a).

8.1 MATERIALS AND METHODS

8.1.1 *Experiments*

11 volunteers (7 male; mean age 26 $\pm$ 3 years, range: 21-31 years) participated in the study for a total of 13 sessions. All participants gave informed written consent prior to the experiments, which had been approved by the Ethics Committee of the University of Leipzig. The paradigm included unilateral finger tapping and a concurrent gas challenge involving 5% CO2 (see Fig. 46).

Functional paradigm

The paradigm consisted of an alternation of rest (30 s) and self-paced unilateral finger tapping (30 s), instructed to be at a frequency of about 1 to 2 Hz and involving a sequential tapping of index finger, middle finger, ring finger and little finger on the thumb. The onset of the tapping and rest periods was communicated to the volunteer by

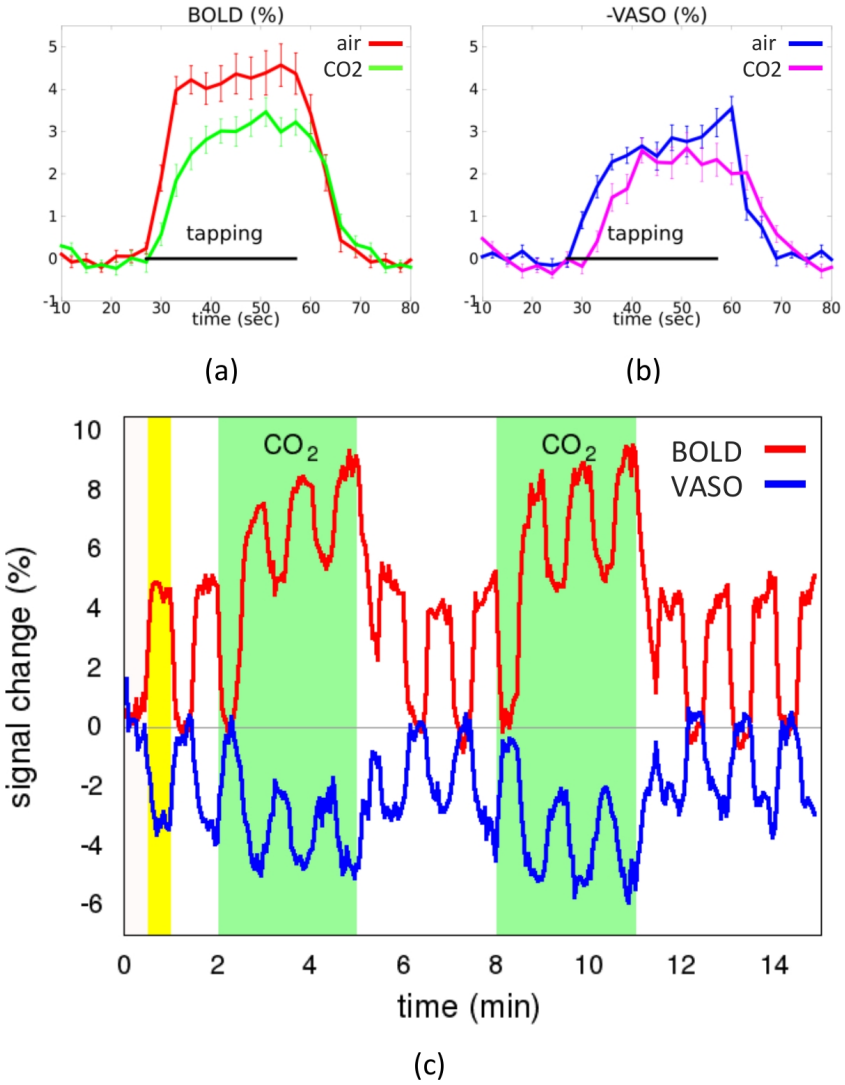

Figure 46: Functional responses to the paradigm. (a) BOLD and (b) VASO signal changes within the region of interest in the hand-knob area (averaged over trials and subjects; error bars indicate the inter-subject standard error of the mean) elicited by finger-tapping during normal air breathing ('air') and hypercapnia ('CO_2') calculated from their respective baseline. Both contrasts show a saturation in the signal change when the task is performed in the hypercapnic state, in accordance with previous observations. Note that the VASO signal changes are negative in sign and were inverted in (b) for easier comparison with the BOLD changes. (c) Timecourses of BOLD and VASO signal changes during the entire session (average over all subjects). The yellow shading indicates the first episode of tapping, while the green shadings (labeled 'CO_2') indicate the two intervals of hypercapnic gas administration. The red and blue solid lines represent the (positive) BOLD and (negative) VASO signal changes in the ROI, respectively (error bars are not shown here for better visibility).

means of a visual command projected onto a screen. The total length of the paradigm was 15 minutes.

Gas challenge

The volunteers wore a mouth piece during the entire duration of the paradigm. A gas mixture containing 74% N_2, 21% O_2 and 5% CO_2 was administered for two blocks of 3 min each, interspersed with intervals of 3 min of room air administration, during the functional paradigm. Physiological values (end-tidal CO_2, end-tidal O_2, heart rate, and respiration rate) were recorded using a BIOPAC MP150 system (BIOPAC Systems Inc., Goleta, CA, USA). A physician administered the gases and monitored the physiological parameters during the entire session. All participants successfully completed the experiment and tolerated the gas challenge well.

Magnetic resonance imaging

All experiments were performed on a MAGNETOM 7 T scanner (Siemens Healthcare, Erlangen, Germany). Either a 24- ($N = 7$) or a 32-channel ($N = 3$) receive head-coil (NOVA Medical Inc., Wilmington, MA, USA), both with single-channel circularly polarized transmission, was used, depending on availability. For fMRI, the SS-SI-VASO technique (Huber et al., 2014b), which provides BOLD and BOLD-weighted VASO contrasts in an interleaved fashion, was employed with the following parameters: $T_E = 18$ ms; $T_R = 1500$ ms; inversion time, $T_I = 1000$ ms; partial Fourier factor: 5/8 (in order to keep T_E short and, hence, the VASO signal proportional to total CBV (Huber et al., 2014a)); 20% phase oversampling (left-right direction, to avoid aliasing artifacts despite the relatively small FOV); number of slices: 7, flip angle: 130°, image matrix: 64×64, nominal voxel size: 0.8×0.8 mm^2, slice thickness: 1.2-1.5 mm, depending on the participant's brain anatomy. No parallel imaging acceleration was applied since the coil sensitivity profile is on the same spatial scale as the FOV. To identify anatomical boundaries, additional inversion-recovery EPI acquisitions were performed with identical sequence parameters and FOV as used for the functional scans, except of the inversion times, which were$T_I = 37/200/300/1200/1500$ ms and the repetition time $T_R = 2000$ ms.

Every participant's anatomy was studied on previously acquired MP2RAGE (Marques et al., 2010) images, in order to plan slice orientation and save time during the session. The clear anatomical landmarks, that is, the central sulcus and the typical omega or epsilon shape of the primary motor cortex in the axial plane (Caulo et al., 2007), make this area easily identifiable. Due to the asymmetric voxel size used here, it is crucial that the slices are aligned perpendicularly to the axis of M1 to minimize partial voluming. For this reason, the hemisphere of choice (and, hence, the contralateral hand chosen for tapping) was the one characterized by the least folded hand-knob area for obtaining the most anatomically straight cortical ribbon of M1, regardless of the hand dominance of the participant. The FOV was centered on M1 and the fold-over was minimized by means of

phase oversampling in order to leave the center of the FOV free from artifacts. The slice orientation was considered to be inadequate for further lamina-dependent analysis whenever the displacement of the surface of the hand-knob region between two consecutive slices exceeded one voxel. Based on this criterion, three subjects had to be excluded from the analysis due to suboptimal slice orientation. A more in-depth and graphical explanation of these aspects can be found in a previous publication (Huber et al., 2015a).

Preprocessing

Functional time series were linearly de-trended to remove low frequency drifts, and then realigned using SPM8 (University College London, UK). Given that the tapping task and the gas challenge were interleaved, that is, conducted during the same imaging scan and with the same slice orientation, no additional co-registration between calibration and task data, other than the motion correction realignment, was necessary. Potential loss of spatial specificity and smoothing during the co-registration step was thus avoided. The data from the inversion-recovery EPI series were evaluated to obtain maps of T_1 and were further used to map GM, WM, and CSF in EPI-space with identical geometry as the functional scans. The maps were used for visual identification of anatomical boundaries and were not intended to be used for accurate T_1 estimation.

VASO volumes were corrected for BOLD weighting and split from the BOLD time series. The BOLD weighting in the VASO contrast is due to the fact that, at 7 T, the extravascular contribution accounts for about the 90% of the total BOLD signal change (Uludag et al., 2009) and, therefore, contaminates the VASO contrast. This contamination was corrected for, in the same way as detailed in (Huber et al., 2014b).

Postprocessing

Z-score maps were obtained using FSL FEAT (University of Oxford, UK). BOLD maps were used to define a ROI in M1. No smoothing was applied at any stage of the analysis to best preserve spatial information.

The GM was divided into laminae in the following way: The functional volumes were resized from a 64×64 to a 256×256 matrix using the nearest-neighbor resampling method. This regridding was performed to obtain smooth laminae across the cortical depth and to minimize artifacts (Tsao, 2003). Such artifacts may arise from the relatively coarse nominal resolution of 0.8 mm compared to the overall cortical thickness of about 4 mm, similar to previous animal studies (Jin and Kim, 2008a). The slice with the best through-slice orientation was chosen, and the contour between GM and CSF on a relatively straight portion of the cortex was manually drawn with FSLView (Jenkinson et al., 2012), following the visible anatomical landmarks in the BOLD volumes and with the aid of M_0, WM, GM and CSF maps. From this contour, equidistant laminae were grown into the GM with a custom-made algorithm based on C++ and ODIN libraries (Jochimsen and von Mengershausen, 2004) (Fig. 47). In contrast to

ultra-high resolutions ($\leqslant$ 70 µm), where equivolume laminae are vital for proper alignment with anatomical structures, the results of equivolume and equidistance layering algorithms are virtually identical at coarser resolutions ($\geqslant$ 400 µm) (Waehnert et al., 2014). With the terms equidistance and equivolume, we indicate a different subdivision of the cortical ribbon into laminae. In the equidistant approach, the Euclidean distance from the boundary surface is kept constant (i. e., for each lamina, every point is equally distant from the boundary). In the equivolume approach, the volume fraction in cortical segments is preserved, thus differing from the equidistance approach if the curvature of the boundary differs from zero. The latter approach was shown to be closer to the actual arrangement of anatomical layers (Waehnert et al., 2014). For the present study, however, the equidistance approach is believed to resemble the curvature of the anatomical layering with sufficient accuracy.

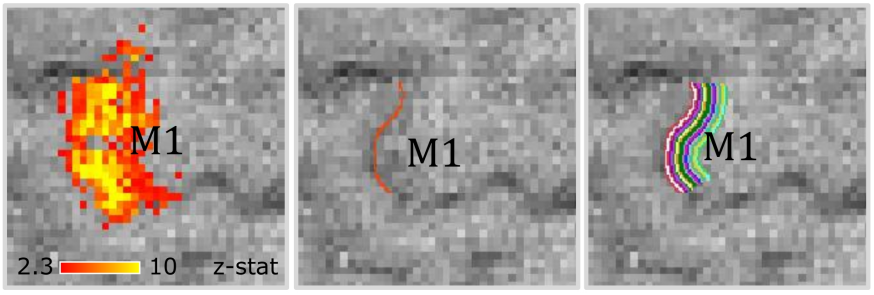

Figure 47: Drawing the GM/CSF contour and corresponding laminae using a equidistance approach for one representative participant. (a) The choice of the ROI is based on the BOLD activation map. (b) The contour between GM and CSF is manually delineated on the resized EPI volumes (here, a resized VASO slice is shown). The resizing consists of changing the matrix size from 64×64 to 256×256 using a nearest-neighbor resampling method. (c) The equidistant layers are then grown from the contour; the interpolated voxels result in a spatial extent of 0.2×0.2 mm^2, thus the minimum thickness of a lamina is 0.2 mm and the maximum is 0.28 mm, depending on the voxel orientation relative to the GM/CSF surface. The mask is defined such that it contains the ROI and accomodates 20 laminae.

BOLD and VASO signal profiles as well as M and $CMRO_2$ profiles were estimated for each lamina, that is, each point in the profile corresponds to a different cortical depth, but does not a priori correspond to a single histological layer. For each participant, the laminar profile of the signal change induced by hypercapnia, δS_{hc}, was calculated as the relative signal change during hypercapnia with respect to baseline (i.e., during normal air breathing). That is, only the intervals of rest (no motor task) during the gas manipulation were used for averaging. The finger-tapping-induced signal change, δS_{task}, was

calculated after averaging all tapping intervals performed during normal air breathing but not during the gas manipulation as the signal is known to saturate during hypercapnia (Fig. 46).

The estimation of laminar $CMRO_2$ profiles was done as follows: For each participant, the average signal change was calculated for each contrast and lamina, and the results were input into the Davis model as discussed above. For the calculation of average signal changes (for any contrast and challenge), the first three time points (9 s) following cessation or onset of the task were excluded from the calculation, in order to avoid averaging non-steady-state intervals. For the same reason, trials right after a hypercapnia block were removed from the analysis. Therefore, for each subject and each lamina, percentage values for the BOLD signal change during finger tapping, the BOLD signal change during hypercapnia, the VASO signal change during finger tapping, and the VASO signal change during hypercapnia were obtained. The average values presented result from averaging each lamina signal change across participants.

Additionally, average scaled signal profiles were obtained for BOLD and VASO contrasts on a laminar basis by normalizing the task-induced activation by the hypercapnia-induced activation. This way, the non-neural vascular components remote from the activated brain tissue that are present in both challenges (i. e., tapping and hypercapnia) are removed and the resulting profile might be a better indicator of brain metabolism than non-normalized, raw signal changes (Cohen et al., 2004).

Finally, the BOLD signal changes recorded during the finger-tapping task (averaged as described above) were scaled by the laminar M profile. The resulting profile should be free from contributions depending on magnetic field strength, T_E and baseline CBV, and should yield more meaningful percent BOLD signal changes.

Signal changes were obtained from ROIs (BOLD Z-score maps) regardless of whether voxels in the VASO timecourses passed the statistical threshold of activation in order to minimize bias of layer-dependent variations of the detection threshold (Goense et al., 2012).

8.2 RESULTS

Robust BOLD and VASO activations were found in all participants within the hand-knob area (Fig. 48).

The average tSNR was (20.7 ± 2.2) for BOLD and (15.2 ± 2.4) for VASO. The functional CNR (defined as $(\Delta S/S_0) \cdot \text{tSNR}$) for the finger-tapping contrast was (0.9 ± 0.3) for BOLD and (-0.4 ± 0.2) for VASO; the functional CNR for the pure hypercapnia challenge (i. e., without concomitant tapping) was (1.1 ± 0.2) for BOLD and (-0.4 ± 0.1) for VASO. The statistical activation maps show the responses under different conditions ('hc' and 'task') and for different contrasts (BOLD

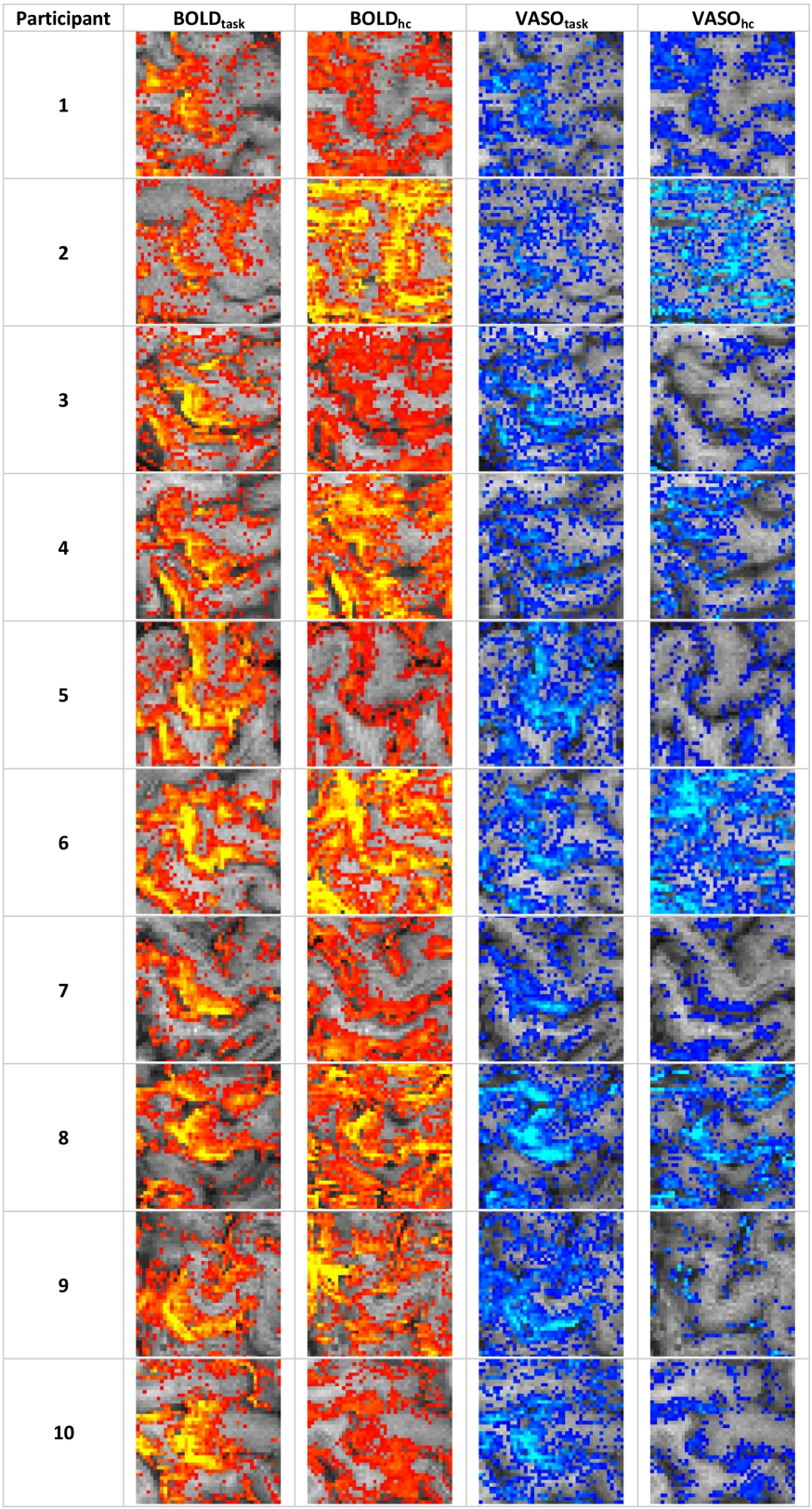

Figure 48: Statistical activation maps for each participant. BOLD and VASO Z-score maps in the hand-knob area of each participant. $BOLD_{task}$ and $VASO_{task}$ indicate activations during the finger-tapping paradigm performed during normocapnia, while $BOLD_{hc}$ and $VASO_{hc}$ refer to the activation induced by the gas manipulation in the absence of the functional task. The Z-score ranges are [2-10] for BOLD and [1-6] for VASO.

and VASO). Only a portion of the entire FOV is shown in the figure. The functional responses of the BOLD and VASO signals during the tapping task robustly outline the omega-shaped cortical ribbon of the hand-knob (M1) and, to some extent, the primary somatosensory areas (S1) on the opposite side of the central sulcus. The response to hypercapnia is not specific to particular brain areas but is detectable all over the GM within the FOV. There were considerable variations in the overall amplitude responses across subjects. However, these variations were consistent across the entire FOV and across different tasks and contrasts for a given subject. For example, participants 1, 2, 7 showed relatively small responses to hypercapnia and finger tapping in BOLD and VASO maps, while participants 4, 8, 9 showed relatively large responses (Table 4). This variability may be attributable to variations in individual baseline physiology and state (see Section 8.3).

N	BOLD_{task}	BOLD_{hc}	VASO_{task}	VASO_{hc}
1	2.33 ± 0.98	4.71 ± 1.95	-1.18 ± 0.47	-2.40 ± 0.88
2	2.93 ± 1.30	3.68 ± 2.10	-1.72 ± 0.89	-2.51 ± 1.35
3	3.40 ± 0.43	4.86 ± 1.04	-2.77 ± 0.44	-3.26 ± 0.98
4	5.49 ± 2.25	6.15 ± 2.77	-3.15 ± 1.07	-2.37 ± 0.58
5	5.35 ± 2.15	5.69 ± 2.77	-3.49 ± 0.94	-2.45 ± 0.88
6	5.23 ± 1.96	5.91 ± 2.34	-2.77 ± 0.95	-2.61 ± 1.11
7	2.57 ± 0.53	4.89 ± 0.79	-2.00 ± 0.37	-2.78 ± 0.91
8	4.82 ± 1.72	6.63 ± 3.44	-3.47 ± 0.68	-2.68 ± 0.93
9	6.58 ± 2.88	5.71 ± 1.62	-4.08 ± 1.56	-1.61 ± 0.44
10	6.08 ± 3.07	5.42 ± 2.40	-2.87 ± 0.46	-1.96 ± 0.63
MEAN	$\mathbf{4.48 \pm 1.54}$	$\mathbf{5.37 \pm 0.85}$	$\mathbf{-2.75 \pm 0.89}$	$\mathbf{-2.46 \pm 0.45}$
CV	34%	16%	32%	18%

Table 4: Summary of the individual and averaged (across participants) percent signal changes (mean $\pm$ standard deviation inside the ROI in M1) evoked by finger-tapping and the breathing challenge in all subjects and their coefficients of variation (CV). N indicates the participants, BOLD_{task} and VASO_{task} indicate activations during the finger-tapping paradigm performed during normocapnia, while BOLD_{hc} and VASO_{hc} refer to the activations induced by the gas manipulation in the absence of the functional task (SD = standard deviation; CV = coefficient of variation).

Averaged BOLD and VASO signal changes within the ROI and corresponding full timecourses are shown in Fig. 46. The BOLD response arising from task performance during the gas manipulation (green trace in Fig. 46a) was partially saturated and slightly delayed when compared to the response during normal air breathing. The VASO response to finger-tapping during hypercapnia (purple trace in Fig. 46b) was also slightly delayed when compared to finger-tapping during normocapnia, but very subtle differences in the response amplitudes between both conditions were found to be insignificant. In Fig. 46c, the average ROI timecourse of BOLD and VASO signal changes, corrected for baseline signal drifts, is shown; the 15 finger-tapping blocks (one of them indicated by yellow shading) as well as the two hypercapnia intervals (green shading) can be easily distinguished. The corresponding relative BOLD and VASO signal changes during the finger-tapping task were $(4.5 \pm 1.5)\%$ and $(-2.7 \pm 0.9)\%$, respectively (mean $\pm$ standard deviation across participants). The relative signal changes arising from the gas manipulation were $(5.4 \pm 0.8)\%$ and $(-2.5 \pm 0.5)\%$, respectively. For the majority of the participants, the relative BOLD signal increase evoked from the breathing challenge was higher in amplitude than the one evoked from the finger-tapping task, although this difference was not significant due to the high variability across voxels; this trend was not observed in the VASO results (Table 4).

Fig. 49 presents the average laminar profiles for BOLD and VASO signal changes during the finger-tapping task and the hypercapnic state. The BOLD profiles, both for finger tapping (S_{task}) and hypercapnia (S_{hc}), showed significantly higher values (two-tailed Student's t-test; $P < 0.01$) in correspondence to the upper laminae (from 0 to 0.25 of the relative depth as shown in Fig. 49a) as compared to the values found in deeper laminae. This reflects the fact that GRE-BOLD is more sensitive to large veins than to capillaries (Buxton, 2013). By contrast, the corresponding VASO profiles showed significantly higher values at larger depth (0.1 to 0.5 of the relative depth) within the GM, but lower values at the cortical surface (two-tailed Student's t-test; $P < 0.01$). This is in line with the fact that the CBV change is scarcely affected by large veins and more specific to the capillary bed (Kennerley et al., 2005; Kim and Ogawa, 2012).

The scaled profiles are shown in Figs. 49c-d. In the scaled BOLD profile, contributions from large veins at the pial surface were significantly reduced; however, no clear peak inside the GM could be distinguished (i. e., no significant difference). The same holds true for the scaled VASO profile. As a characteristic difference, scaling of the VASO profile yielded values slightly exceeding 1 throughout GM, reflecting the fact that the motor task produced relatively higher CBV changes than the respiratory challenge.

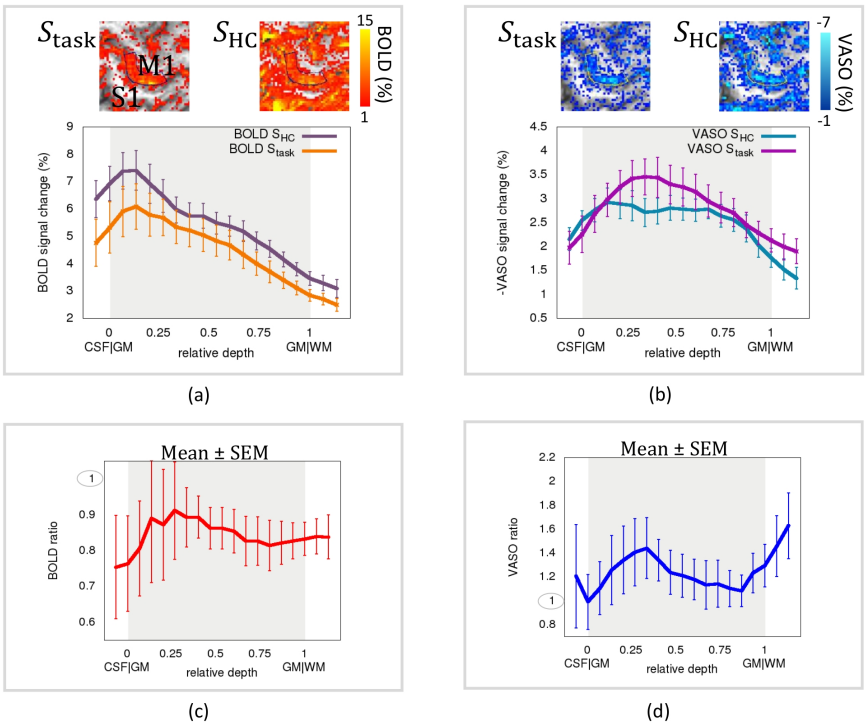

Figure 49: Laminar profiles during functional activation and scaled profiles. (a) BOLD and (b) VASO laminar profiles. Note that the VASO signal changes, which are negative in sign, were inverted for easier comparison with the BOLD profiles. Gray shading indicates the width of the cortex. Arbitrary values of 0 and 1 are assigned to the relative depth at the positions of the CSF interface and the WM interface, respectively. The insets show relative signal changes calculated from the preprocessed data in the hand-knob area during finger tapping (S_{task}) and during hypercapnia (S_{hc}) for one representative participant. The error bars refer to the standard error of the mean (SEM) across participants. Scaled cortical profiles for (c) BOLD and (d) VASO, obtained by dividing the tapping-induced activation profile by the hypercapnia-induced activation profile. Gray shading indicates the width of the cortex (as in Fig. 49). The error bars refer to the standard error of the mean (SEM) across participants.

Application of the modified Davis model (Eqs. 78 and 80) yields estimates of M and $CMRO_2$ on a laminar basis. The corresponding profiles are shown in Fig. 50. The calibration constant, M, showed a marked variation with depth, with higher values at the CSF interface and a steady decrease towards the WM boundary. Values within GM were found to be ranging from approximately 14% to 8%, with a mean value of $(11 \pm 2)\%$ across laminae. The $CMRO_2$ profile showed lower values at the cortical surface with a peak inside the GM. Mean $CMRO_2$ was $(30 \pm 7)\%$ with values ranging between approximately 40% and 20%. The $CMRO_2$ changes within the inner laminae (from 0.1 to 0.5 of the relative depth as shown in Fig. 50b) are found to be significantly different from the values of the outer laminae (two-tailed Student's t-test; $P < 0.01$).

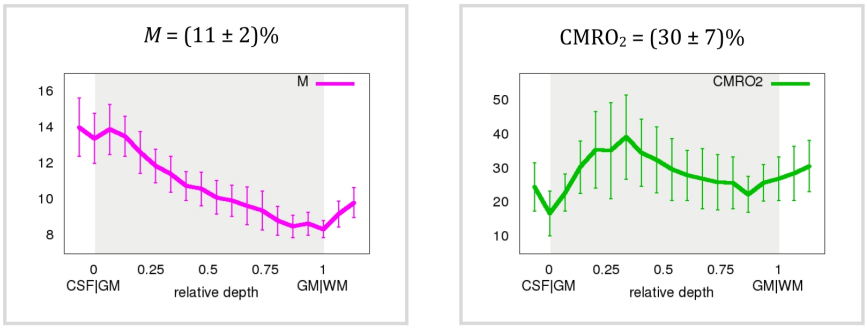

(a) (b)

Figure 50: Laminar profiles for (a) M and (b) $CMRO_2$ obtained by solving the Davis model (Eqs. 78 and 80). The calibration factor M is largest at the cortical surface and decreases with cortical depth. The $CMRO_2$ response during the finger tapping task appears to be more specific to the neural tissue below the cortical surface. Gray shades indicate the extension of the cortex (as in Fig. 49). The error bars refer to the standard error of the mean (SEM) across participants. Average GM values are $M = (11 \pm 2)\%$ and $CMRO_2 = (30 \pm 7)\%$.

Finally, the BOLD profile can be normalized by the parameter M on a laminar basis. This step removes the contributions related to baseline physiology and measurement parameters contained in the calibration constant (e.g., T_E, CBV_0, magnetic field strength, etc.) and yields more meaningful percent BOLD signal changes. The result is shown in Figure 51.

8.3 DISCUSSION

The data from our study suggest that sufficient CNR was obtained to investigate simultaneously recorded BOLD and CBV responses during finger tapping and hypercapnia, as well as for high-resolution estimation of $CMRO_2$. Fig. 47 demonstrates that significant changes in

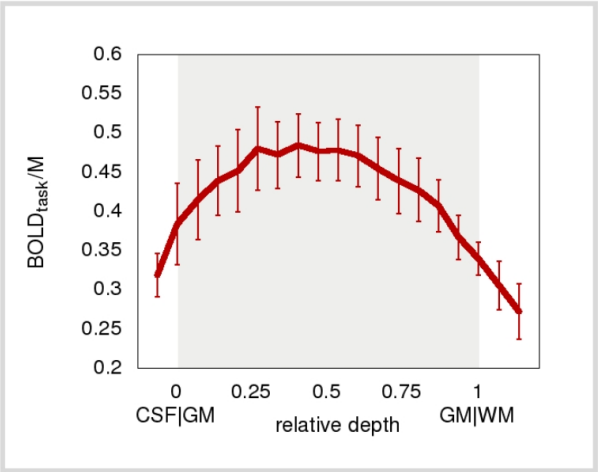

Figure 51: Laminar normalized BOLD profile. Normalized BOLD profile, obtained by dividing the tapping-induced activation profile by the M profile, lamina by lamina. Gray shades indicate the extension of the cortex (as in Fig. 49). The error bars refer to the standard error of the mean (SEM) across participants.

BOLD and VASO signals are consistently detected across participants. Independent of this consistent detectability, however, there is relatively large variability in the amplitude of the functional responses across participants, contrasts and applied stimuli. This level of variability is expected however (Liu et al., 2013a; Lu et al., 2008) due to variations in baseline physiology (e.g., CBF_0, venous baseline oxygenation, etc.) and they are one of the main motivations for the use of BOLD calibration. Significant changes in BOLD signal were detected more reliably than changes in VASO (Fig. 48), which could be due to the CNR limitations of VASO from the small CBV responses during hypercapnia or finger tapping. Nevertheless, VASO signal changes are found to be more stable than BOLD signal changes as indicated by reduced relative errors in Table 4. The quality of BOLD and VASO activation maps during hypercapnia is rather variable across participants (Fig. 48); Z-score maps show a similar variability for both contrasts, suggesting that it could be related to volunteer specific variations of vascular reactivity and baseline physiology (Lu et al., 2008), rather than imperfect blood nulling, which would only affect the VASO contrast (see Section 8.4 for more details). Participants showing less significant VASO signal changes during hypercapnia (e.g., participants 3 and 5 in Fig. 48), also show less significant BOLD changes for the same condition.

In most participants, the percent signal change during hypercapnia for BOLD signal changes is found to be larger than the activation resulting from the finger-tapping task (Table 4). This trend is, however, reversed in two participants (participants 9 and 10), although not significant due to high fluctuations. For VASO, the percent signal change

during hypercapnia is generally not higher than the one induced by the finger-tapping task. 6 participants out of 10 show higher relative VASO changes during finger-tapping than during hypercapnia.
The same table shows that the signal change to the hypercapnic stimulus is less variable across subjects (coefficient of variations (CVs) are 16% for BOLD and 18% for VASO), while the variability of the signal change due to finger tapping is higher (CV of 34% for BOLD and 32% for VASO). This variability in the functional task response might result from inter-subject variability in the tapping frequency. We note that the participants had been verbally instructed to tap a frequency of about 1-2 Hz; however, this was not paced during the paradigm. BOLD signal change was previously shown to scale positively with tapping frequency (Rao et al., 1996).

The smaller and delayed hemodynamic response to brain activity during hypercapnia compared to breathing air is consistent with previous reports (Gauthier et al., 2011), suggesting that it is more weighted towards delayed downstream capillaries and veins, when arterioles are pre-dilated (Kennerley et al., 2012). Including the tapping periods performed during hypercapnia for the calculation of $CMRO_2$ would, thus, bias the results. Consequently, they were excluded from the analysis and used only for comparison with the shape and intensity of the hemodynamic response during normal air breathing.

Assuming a baseline value of $CBV_0 = 5.5\%$, the VASO signal decrease of $(-2.5 \pm 0.5)\%$ during hypercapnia corresponds to a CBV increase of $(43 \pm 9)\%$. This is in agreement with other high-resolution VASO studies (Hua et al., 2013; Huber et al., 2015a). However, this estimate is significantly larger than earlier CBV studies (Cretti et al., 2013; Lu et al., 2003; Poser and Norris, 2009). This discrepancy may be due to the lower resolution used in these studies and the correspondingly larger partial volume effects of WM and CSF (Pfeuffer et al., 2002).

The observation that BOLD signal changes are smaller for finger tapping than for hypercapnia (Fig. 49a), while the VASO results show slightly larger signal change for finger tapping compared to hypercapnia (Fig. 49b), is consistent with predictions from the Davis model. CBV changes as detected with VASO are confined to the vasculature, while the BOLD contrast also contains contributions from increased $CMRO_2$ via a concomitant increase in the dHb concentration. In this respect, the larger vascular response (i.e., 'VASO response') and the oxygen oversupply during finger tapping compared to hypercapnia is accompanied by simultaneously increased oxygen consumption, which attenuates the BOLD signal.

The depth-dependent profiles for the BOLD and the VASO response (Fig. 49) are consistent across participants and agree with published results (Goense et al., 2012; Huber et al., 2015a; Jin and Kim, 2008a).

The profile for $CMRO_2$ (Fig. 50b) is also not dominated by the superficial vasculature. Considering the layer-dependent cytoarchitecture (Porter and Lemon, 1993), enhanced cortico-spinal output activity could be expected in layer V (Kaneko et al., 1994), whereas enhanced cortico-cortical input into M1 could be expected in layers II and III (Yu et al., 2014). Hence, two peaks of $CMRO_2$ activation corresponding to layer V and to layers II/III might be expected. The profile for $CMRO_2$ changes (Fig. 50b) is more specific to the GM than the BOLD profile (Fig. 49a), and the higher values within the GM could be indicative of an increased activity in correspondence to these layers. In fact, the profile shows a peak that could be roughly related to layer III, which would be in line with observation of glucose utilization in rats (Collins, 1978).

It is worth pointing out that the VASO profile (Fig. 49b) is virtually identical (within experimental precision) in shape and amplitude compared to the cortical profile of the $CMRO_2$ change (Fig. 50b), even when evaluated for a range of α and β values. This result suggests a high spatial specificity of the CBV response to activity-induced metabolic changes on a layer-dependent level. Furthermore, it suggests that the metabolic-vascular coupling, often summarized in the proportionality factor n (Buxton et al., 2004), is highly conserved across cortical layers. Small deviations between the profiles of the VASO and $CMRO_2$ responses at the border to WM might arise from partial volume effects with WM. In WM, CBV quantification from VASO experiments breaks down, because the underlying assumptions regarding the vasculature refilling time and the baseline CBV distribution are no longer adequate. The similarity between the VASO and $CMRO_2$ profiles might as well be related to the fact that CBV was shown to have a large impact on the model (Fig. 33). However, they indicate different aspects of brain activity. CBV changes are dominated by the arterial/arteriolar compartment, while $CMRO_2$ should be specific to the site of metabolic changes (the capillaries). This difference might not be seen at the resolution used here, hence the similarity of the profiles, but could become appreciable at finer scales.

M represents the maximum possible BOLD signal change, corresponding to the complete removal of deoxyhaemoglobin from the voxel. Since venous dHb content is higher than the arterial one, larger oxygenation changes and, in turn, higher BOLD signal changes are expected to be located in the venous compartment. This is in line with the observation that M is higher at the cortical surface (Fig. 50a), but inconsistent with some previous studies. For example, Herman et al. estimated M as the product between T_E and R_2' (defined through $R_2' = R_2^* - R_2$) and found it to be constant across the entire cortical depth (Herman et al., 2013). The results by Herman et al., how-

ever, are not completely in line with previous findings, for example in terms of the profile of laminar CBV changes (Jin and Kim, 2008b).

The cortical profile of BOLD signal changes normalized by M (Fig. 51) provides signal changes free from baseline contributions. A striking similarity in shape with the VASO profile (Fig. 49b) can be observed; they are spatially more specific to the inner cortical layers and less affected by the large surface vasculature than the uncorrected BOLD (Fig. 49a), matching expectations. It should moreover be noted that this normalization strategy differs from what is shown in Fig. 49c. There, the cortical BOLD response resulting from finger tapping is normalized by the one resulting from the hypercapnic state; hence, the calibration parameter M is not involved in the estimation. To obtain a normalization like the one in Fig. 49c, no additional physiological assumption needs to be made, nor other contrasts acquired. This is clearly a preferable method in case ASL or VASO sequences are not available. The resulting profile has some limitations which are reflected in the high errorbars shown in Fig. 49c; it is more prone to baseline effects and has more inter-subject variability than the profile in Fig. 51. Nevertheless, the pial vein contamination is removed, making it preferable to the uncorrected BOLD (Fig. 49a) for brain metabolism considerations.

It must be noted that the profiles shown in Fig. 49c and Fig. 51 have conceptual differences with respect to their dependency on the interaction between changes in CBF and $CMRO_2$ (often referred to as n value). These differences are theoretically described and simulated in (Liu et al., 2013b). According to their description and simulations, the profile shown in Fig. 51 (i.e., task BOLD response scaled by M) is expected to account for variations in baseline physiology (e.g., baseline venous oxygenation, venous baseline CBV, hematocrit), but not completely for variations in the nonlinear response properties of BOLD signal reactivity (due to BOLD signal saturation). The profile shown in Fig. 49c (i.e., the task response normalized by the hypercapnia-induced response), on the other hand, can better account for variations in BOLD reactivity properties but cannot fully account for variations in baseline physiology, which alter BOLD, CBV and CBF responses differently (e.g., n-value, venous baseline blood volume).

8.4 LIMITATIONS

The overall $CMRO_2$ changes are within the range of previously published results from calibrated BOLD studies (Blockley et al., 2013), with slightly larger values most probably due to the higher resolution used in our experiments and correspondingly smaller partial volume effects. However, the $CMRO_2$ profile (Fig. 50b) shows a high variability (even leading to negative $CMRO_2$ values in some cases, data

not shown). A few possibilities should be discussed at more detail to explain this observation:

1. Validity of Grubb's law. A single value for the Grubb relation may not correctly capture the underlying physiology. For example, there could be flow increases not accompanied by volume increases, such as in the more superficial layers, where the signal change is dominated by larger veins. This situation would not be detected by a global Grubb's law describing the coupling, thereby leading to erroneous estimations of $CMRO_2$. To clarify the importance of this effect, the flow-volume coupling assumption (i.e., Grubb's law) should be revisited and investigated on a finer, layer-dependent scale.

2. Limits of the applicability of Fick's principle. The Davis model relies on the Fick principle assuming $[dHb] \propto CMRO_2/CBF$. The underlying assumption is that all the oxygen delivered by blood flow is either metabolized or drained away. However, the individual terms of Fick's principle are usually measured in different compartments of the vascular tree. The changes in dHb measured with the BOLD signal arise from draining veins, while CBF or CBV measured with, respectively, ASL or VASO arise mainly from arterioles and capillaries. As long as all vascular compartments are equally represented in each voxel (e.g., at low spatial resolution), Fick's principle remains valid. In lamina-dependent analyses, however, this assumption must be revisited. At submillimeter resolutions, vascular compartments are no longer distributed equally in every voxel. For example, voxels at the cortical surface are dominated by large draining veins, and large changes in [dHb] result in increased BOLD signal changes. However, the corresponding changes in CBF and CBV predominantly result from other, deeper cortical layers. Hence, the applicability of Fick's principle in lamina-dependent studies might be limited.

3. Confounding inflow effects in VASO. In case of inflow effects (i.e., the flux of non-inverted, 'fresh' blood isochromates into the imaging slice), the recorded VASO signal could yield positive values. This will more likely happen if the AAT is reduced, as it is in the case during a hypercapnic state (Ho et al., 2011). In order to account for this source of error in the current study, the blood-nulling time was reduced to be shorter than the AAT by means of a custom-designed partial inversion pulse (Huber et al., 2014b). Inflow-effects in SS-SI-VASO would result in substantial signal increase up to several percent (i.e., a positive signal change instead of the expected negative VASO signal change that indicates increased CBV) and should be readily visible in the '$VASO_{hc}$ maps' with the highest probability at locations of

large feeding arteries at the cortical surface. However, such features were not evident in our data recorded during hypercapnia. As the inverted VASO signal in Fig. 49b is positive at the cortical surface, we expect that such inflow effects do not compromise our extracted profiles of $CMRO_2$ changes.

4. Confounding relaxation effects. An additional concern with VASO applications could be the difference of about 100-200 ms between the (longer) arterial and (shorter) venous blood relaxation times T_1. However, even in a worst-case scenario, the error resulting from the corresponding mismatch in the blood nulling time is smaller than the observed inter-subject variation and SS-SI-VASO can be considered to be sensitive to total CBV changes (Huber et al., 2015a). Consequently, the VASO signal is intrinsically weighted towards the arterial and arteriolar compartments due to the fact that, within the cerebral vascular tree, these are the ones capable of actively dilating and, hence, undergo the largest relative volume change (Hillman et al., 2007; Hua et al., 2011; Lee et al., 2001).

5. Limitations related to the assumed baseline CBV_0. CBV changes measured with VASO refer to relative volume changes in the voxel in units of ml blood volume change per 100 ml of tissue volume. In the Davis model (Eq. 73) however, CBV changes are in units of ml blood volume change per ml of baseline blood volume. The conversion between these units is usually done assuming a homogeneous baseline CBV distribution of 5.5% (Lu et al., 2013). On a laminar-dependent level, however, this approach must be revisited since baseline CBV varies with cortical depth (Goense et al., 2007; Kennerley et al., 2009; Kim et al., 2013). Due to relatively large (macrovascular) penetrating arteries and veins, total baseline CBV is considerably larger at the cortical surface than in deeper cortical layers (Goense et al., 2007; Kennerley et al., 2005; Kim et al., 2013). The microvascular CBV distribution, on the other hand, is relatively homogeneous across the cortex with small variations ($\approx$ 10-25%) in individual layers dependent on the area of interest (Duvernoy et al., 1981; Kim et al., 2013; Weber et al., 2008). Most of the activation-related CBV changes are confined to microvessels (Gagnon et al., 2015; Hillman et al., 2007), which are homogeneously distributed across cortical layers, and not to large vessels dominating the baseline CBV in upper layers. Accordingly, the relative CBV change as derived in our study from VASO is normalized assuming a homogeneously distributed baseline CBV value across cortical layers. This approach was chosen to avoid artifacts of inverse macrovascular weighting arising from non-reacting macrovessels in upper cortical layers (Huber et al.,

2015a). Residual variations in the microvascular baseline CBV of approximately 10-25% are considered to be negligible here. Future work should use a more realistic estimation of baseline blood volume based on human post-mortem studies (Lauwers et al., 2008).

6. Metabolic effects of hypercapnia. In the present work, mild hypercapnia is assumed to be an isometabolic challenge. To date, no general consensus is found however, with previous literature reporting both increases and decreases in $CMRO_2$ (Pike, 2012). If a decrease of 5% in $CMRO_2$ is assumed, this would result in an overestimation of the M parameter of about 5% and a subsequent overestimation of $CMRO_2$ of about 20% (taking into account the mean values for BOLD and VASO signal changes reported in Table 4). Since this bias is still lower than the intersubject variability (about 23% in this study), it can be considered negligible with respect to the interpretation of the presented results.

7. Temporal dynamics of the BOLD response. The Davis model relies on steady-state BOLD signal changes and doesn't take into account the temporal evolution of its different components. For instance, Kim and Kim (Kim and Kim, 2011) showed that the venous CBV response evolves on a much slower timescale than the arterial CBV response. Nevertheless, previous work has shown that the α exponent for hypercapnia and neuronal activation is comparable (Chen and Pike, 2010). In any case, temporal dynamics uncertainty are an issue in the whole field of calibrated BOLD based on the Davis model; in terms of laminar studies, those add to the uncertainty in the depth-dependent parameters, as mentioned above. A way of disentangling such contribution on a laminar basis would be monitoring the time evolution of the different components (Huber et al., 2014a).

8.5 CONCLUSION

We have demonstrated that it is possible to measure CBV and BOLD signal changes during finger tapping and hypercapnia on a submillimeter laminar level. By application of a modified Davis model, this data can be used to estimate changes of $CMRO_2$ and the value of the calibration parameter M across the cortical thickness on this laminar scale. We have shown that there are differences in depth-dependent activation profiles of the BOLD signal and CBV and that these features are consistent across participants. The VASO contrast was observed to be more specific to the site of neuronal activity compared to the GRE-BOLD signal, with a clear peak inside GM.

The spatial heterogeneity of the vasculature within the cortex, evidenced by the profile of the calibration parameter, M, suggests that the applicability of the Davis model on this scale is not straightforward. Our study may provide a starting point for future research investigating possible adaptations of the Davis model that better account for laminar-specific variations in the underlying physiology. In particular, the Davis model would benefit from the knowledge of the fine-scaled spatial distribution of the baseline CBV, which has a strong effect on the relaxation rate ΔR_2^* (Bandettini and Wong, 1997), and from a more realistic, layer-dependent Grubb exponent, α, which dominates CBV-CBF coupling. Similarly as calibrated BOLD experiments have yielded further insight into imaging neuronal activation at standard spatial resolutions, we may expect interesting results from future quantitative, laminar-dependent studies as intra-cortical activation patterns and efferent/afferent activities might be examined without strong non-neural bias.

9

AMPLITUDE OF CORTICAL LAMINAR RESTING-STATE FLUCTUATIONS

The amplitude of resting-state BOLD signal fluctuations has been proposed as an alternative for hypercapnia in the context of signal calibration (as discussed in Chapter 7).
In this Chapter, we investigate and validate the use of RSFA indices to normalize the BOLD signal at submillimeter spatial resolution on a laminar basis. We do this by comparing the results with other metrics obtained by gas calibration in a separate session.

Parts of this work have been presented at the 24th meeting of the International Society for Magnetic Resonance in Medicine in Singapore, with the title "Cortical Laminar Resting-State Fluctuations Scale with Hypercapnic Response" (Guidi et al., 2016b).

9.1 MATERIALS AND METHODS

9.1.1 *MRI acquisition parameters and experimental setup*

Ten right-handed participants (6 males, mean age: 25.8 ± 3.6 years) with no history of neurological disorder took part in the study. All participants gave informed written consent prior to the experiments, which had been approved by the Ethics Committee of the University of Leipzig. Participants were asked to refrain from coffee and alcohol intake on the day of the experiment. A physician was present at each session to monitor physiological values during the breathing manipulation task.

Experimental setup

All scans were performed on a MAGNETOM 7 T scanner (Siemens Healthcare, Erlangen, Germany) using a single-channel transmit, 32-channel receive head coil (Nova Medical, Wilmington, MA, USA). The gas was delivered to the participant through a tube connected to a mouth piece. A second tube was used for directing the exhaled air outside the scanner bore. Inhaled and exhaled gases were prevented from mixing via valves placed in the interior of the mouth piece. Heart beat and respiration timecourses were recorded using peripheral devices provided by Siemens (finger plethysmograph and respiratory bellow). The $P_{ET}CO_2$ and $P_{ET}O_2$ were recorded using a BIOPAC system (BIOPAC Systems, Goleta, CA, USA). Visual instructions were delivered to the participant through projection onto a screen, which could be visualized by means of a mirror fixed to the radiofrequency coil. In case of visual deficiencies, MRI-safe glasses were provided to the participant.

Functional paradigm

The paradigm consisted of two sessions, each 15 min long. The first one was a block-design hypercapnia task, followed by a resting-state session. The hypercapnia task consisted of an alternation of room air and a CO_2-enriched gas mixture (containing 5% CO_2, 21% O_2 and 74% N_2) delivered at a flow rate adjusted manually at about 18 liters/min. After an initial 2-minute block of room air breathing, the gas mixture was administered for two blocks of 3 minutes each, separated by an equally long block of room air. A final 4-minute block of room air breathing was added for baseline localization. Prior to the breathing manipulation experiment, participants were asked to wear a nose clip and to adjust the mask tightly to their faces in order to avoid inflow of room air. For the resting-state scan, a fixation image was projected onto the screen and participants were asked either to fixate it or to stay with the eyes closed for the whole duration of the experiment and not to fall asleep.

Sequence

A SS-SI-VASO sequence (Huber et al., 2016b, 2014b) with a 3D readout (Poser et al., 2010) was used for the acquisition, which is beneficial for sub-millimeter applications. The following parameters were employed: $T_E = 24$ ms; effective $T_R = 1648$ ms; $T_I = 900$ ms, GRAPPA acceleration factor = 2, partial Fourier factor = 6/8, 10 slices, bandwidth = 1042 Hz/px, nominal voxel size = $0.8 \times 0.8 \times 1.8$ mm^3, asymmetric FOV with a matrix size of 132×44. Variable flip angles were used in order to minimize T_1-related blurring along the z-direction (Huber et al., 2015c). Previously acquired MP2RAGE (Marques et al., 2010) images were inspected in order to localize the M1 region of the participants, and special care was taken at the time of slice positioning in order to have them aligned perpendicularly to the axes of the hand-knob area of the left M1, similarly as explained in Chapter 8.

Preprocessing and layering

All timecourses were corrected for rigid-body motion using the function 'Realign: Estimate and Reslice' in SPM12. Recorded respiratory and cardiac traces were used for denoising resting-state timecourses using the AFNI (Cox, 1996) implementation of RETROICOR (Glover et al., 2000). All fMRI timeseries were linearly detrended to remove low-frequency signal drifts.

The anatomical references for layering were taken from resized T_1-weighted EPI maps generated from the functional resting-state and the breathing-manipulation timeseries. The T_1-weighting was derived by quantifying the EPI signal variability of the original timeseries of SS-SI-VASO with alternating EPI signal acquired with and without preceeding inversion pulse, that is, prior to the BOLD/VASO contrast splitting. Since the signal difference of T_1-weighted VASO and BOLD is dominated by longitudinal relaxation, this 'anatomical' GM/CSF contrast in EPI space is comparable to that of an uniform T_1-weighted image (UNI) image of MP2RAGE. An example for one representative participant is shown in Fig. 52. For layering purposes, the original matrix size of 132×44 was resized by a factor of 16 to

528×176. This upscaling was done analogously to most segmentation software packages in order to obtain smooth laminae without angularity limitations in voxel space. The GM/CSF and GM/WM borders were manually drawn on the slice with the better through-plane orientation. The ROI was defined as the portion of GM, which was best aligned to the slice orientation across depth and additionally showed sufficient BOLD and VASO activation. In this ROI, 15 laminae were grown following an equivolume approach (Fig. 52) with a custom-made algorithm based on C++ and ODIN libraries (Jochimsen and von Mengershausen, 2004), similarly as detailed in (Guidi et al., 2016a; Huber et al., 2015a).

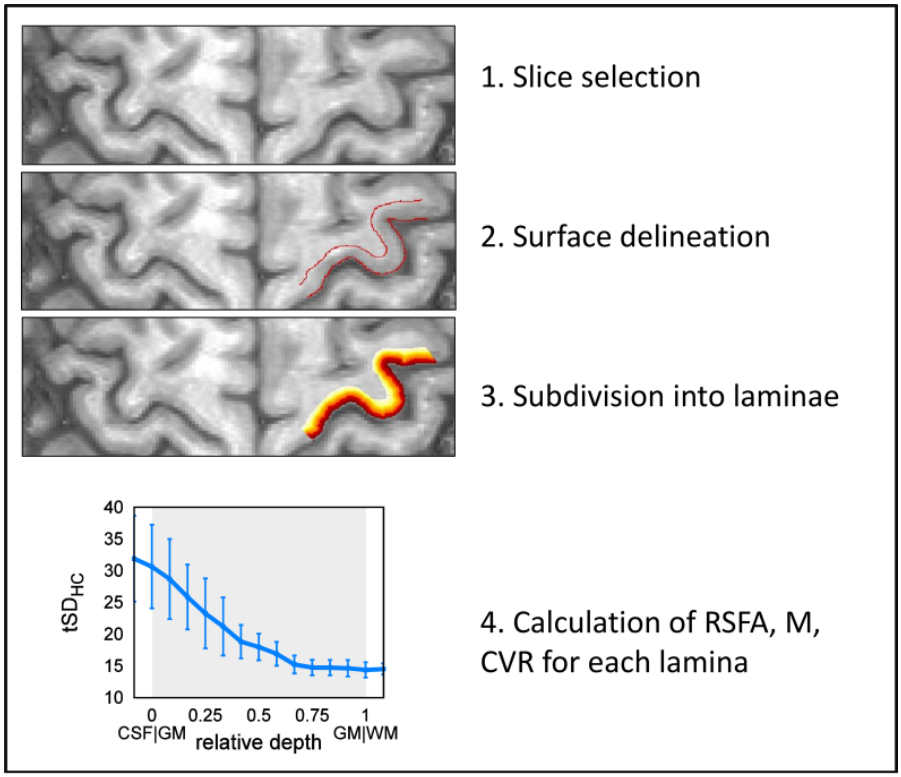

Figure 52: Schematic of the four steps behind the calculation of depth-dependent profiles. (1) The slice with the best through plane orientation is chosen and (2) the surfaces between GM/CSF and GM/WM are manually delineated. (3) Equi-volume laminae are created between these two borders. (4) Finally, the quantities of interest are averaged on each single lamina and plot as a function of depth. As an example, the laminar profile of tSD_{hc} for one representative participant is shown.

9.1.2 *Calculation of the quantities of interest*

The resting-state fluctuation amplitudes of the unfiltered (RSFA), low-frequency ($RSFA_{lf}$) and high-frequency ($RSFA_{hf}$) timeseries were taken to be the tSD of the corresponding timeseries, thus following the ap-

proach presented in (Kannurpatti et al., 2012). The low-frequency resting-state timeseries included frequencies in the band 0.01-0.1 Hz, while the high-frequency timeseries included the ones in the band 0.1-0.15 Hz. The unfiltered timeseries included frequencies in the range 0.01-0.15 Hz, given by the scan duration and T_R. RSFA was calculated for each lamina (Fig. 53). Similarly, the amplitude of hypercapnia-induced signal changes (tSD_{hc}) was taken to be the temporal standard deviation of the corresponding timeseries (Kannurpatti and Biswal, 2008).

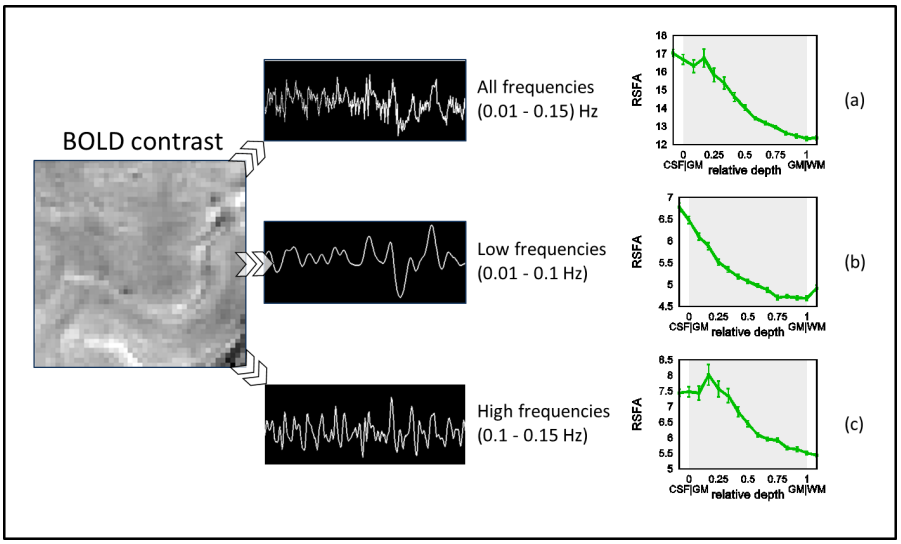

Figure 53: Schematic of the resting-state fluctuation amplitude calculation for one representative participant. A highpass cutoff of 0.01 Hz is first applied to the resting-state BOLD timeseries. The timeseries is then bandpass filtered into two frequency bands: a low-frequency band (0.01-0.1 Hz) and a high-frequency band (0.1-0.15 Hz). The RSFA for (a) the full frequency band, (b) the low-frequency band and (c) the high-frequency band are calculated as the standard deviation of the corresponding timeseries.

The calculation of the calibration parameter, M, followed the approach presented in Chapter 6.

The depth-dependent values of M and tSD_{hc} were correlated with each of the RSFA profiles separately for each participant. The correlations were constructed as scatter plots in which each point represents one lamina, and the squared Pearson correlation coefficient (R^2) for the linear regression was computed (Fig. 55).

9.2 RESULTS

All participants tolerated well the breathing manipulation and performed the experiment successfully. One participant was excluded from the final analysis due to excessive motion (above 1 mm) during the gas manipulation session.

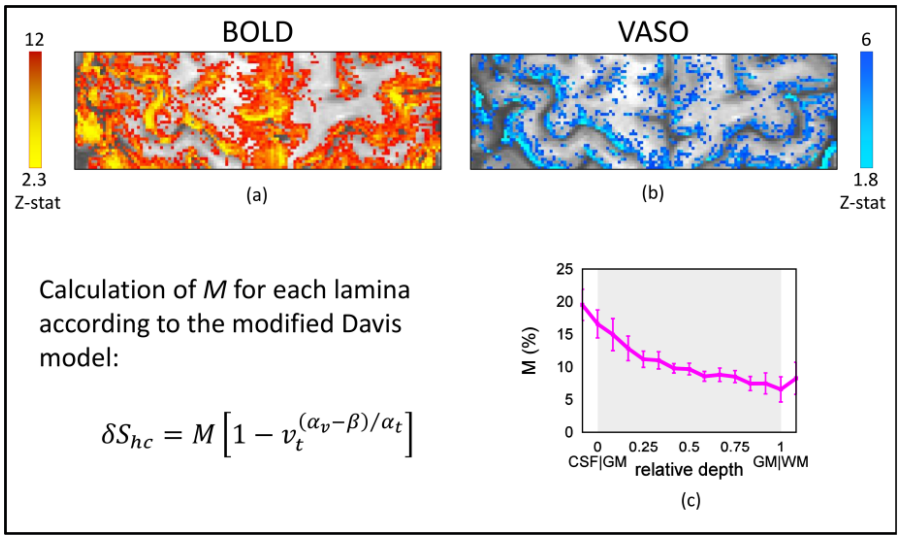

Figure 54: Z-stat maps of hypercapnia-induced (a) BOLD and (b) VASO signal changes and (c) calculation of the calibration parameter M. Errorbars refer to the standard error of the mean. A region of interest encompassing the hand-knob area of one hemisphere where BOLD and VASO signal changes are significant ($Z > 2.3$, $p < 0.01$ for BOLD and $Z > 1.8$, $p < 0.01$ for VASO) is chosen for the calculation of the calibration parameter M. The calculation of M follows the formula reported in the figure.

It was possible to accommodate up to 15 equi-volume laminae within the GM ribbon of the hand-knob of each participant. The tSNR in the ROI defined by the laminae was found to be between 25 and 35 for BOLD timeseries and between 15 and 25 for VASO timeseries.

For all participants, RSFA and tSD_{hc} profiles showed higher values at the cortical surface and gradually decreasing values towards the white matter. The mean depth-dependent profile of M showed a similarly decreasing shape (Fig. 54) but this shape was not consistently seen for each participant.

All quantities that were considered for linear regression showed a positive correlation. The correlation for the regression between RSFA and tSD_{hc} was found to be $R^2 = 0.92 \pm 0.06$ (mean $\pm$ standard deviation across participants) for RSFA of the unfiltered timeseries, 0.94 ± 0.06 for $RSFA_{lf}$, 0.92 ± 0.08 for $RSFA_{hf}$ (Table 6). The correlations were highly significant for every single participant ($p < 0.01$).

For the correlation between RSFA and M, R^2 was found to be 0.62 ± 0.19 ($p < 0.05$ for 8 out of 9 participants) for RSFA of the unfiltered timeseries, 0.60 ± 0.26 ($p < 0.05$ for 7 out of 9 participants) for $RSFA_{lf}$ and 0.55 ± 0.26 ($p < 0.05$ for 7 out of 9 participants) for $RSFA_{hf}$ (Table 6).

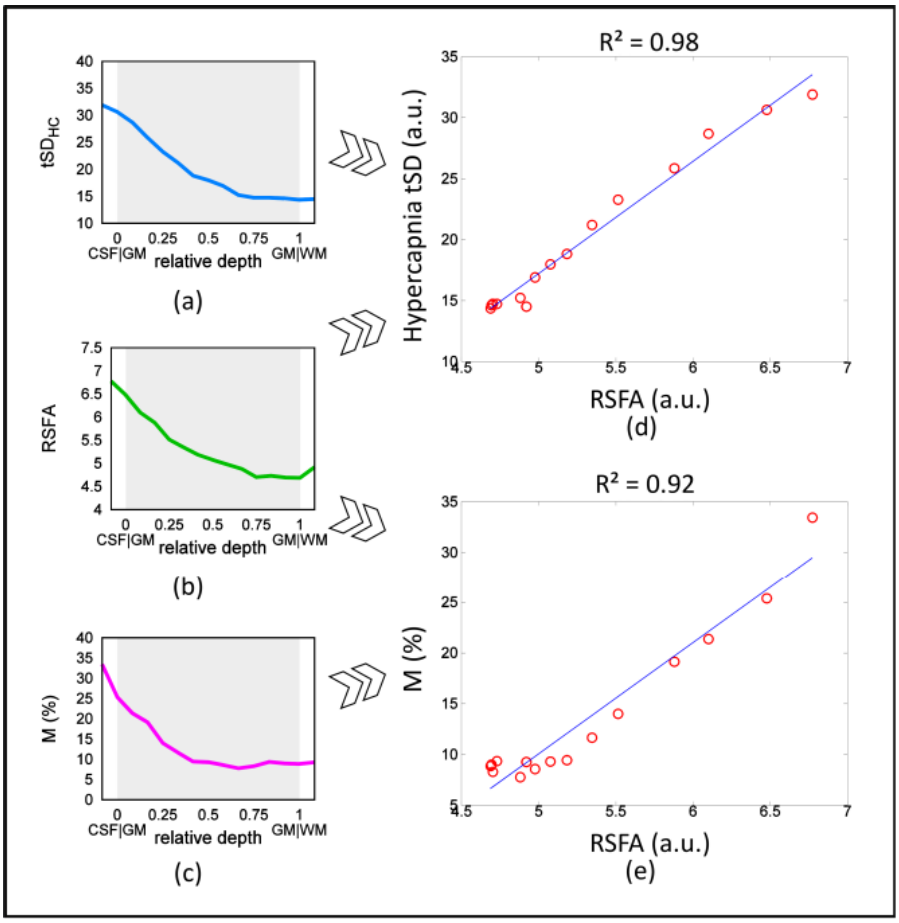

Figure 55: Example of linear regression construction for one representative participant. The laminar values of (a) tSD_{hc} and (c) M are plotted against (b) laminar RSFA. The result of the linear regression of (d) RSFA with tSD_{hc} and (e) RSFA with M are shown. Each point refers to one lamina.

9.3 DISCUSSION

A nearly perfect correlation between RSFA and tSD_{hc} was found for all frequency bands considered. This result confirms previous observations at standard resolution on a voxel-wise basis (Kannurpatti and Biswal, 2008). The correlation strength found in our work is somewhat higher than the one found in (Kannurpatti et al., 2012), which may be attributable to the fact that the linear regression was done here on a laminar basis. There was no significant difference in the strength of the correlation between high and low frequency bands, indicating that they scale similarly across depth.

A significant correlation was also found for the linear regression between RSFA and M. For the majority of the participants, there was no significant difference in the strength of the correlation between frequency bands, similarly as for the correlations with tSD_{hc}. M can be considered in our work to be modulated by subject-specific

PARTICIPANT	R^2		
	tSD_{hc}-RSFA	tSD_{hc}-$RSFA_{lf}$	tSD_{hc}-$RSFA_{hf}$
1	0.79	0.81	0.86
2	0.87	0.95	0.98
3	0.90	0.89	0.83
4	0.89	0.92	0.89
5	0.92	0.98	0.78
6	0.98	0.99	0.98
7	0.96	0.96	0.98
8	0.99	0.99	0.99
9	0.96	0.95	0.98
MEAN	0.92 ± 0.06	0.94 ± 0.06	0.92 ± 0.08

Table 5: Correlation coefficients (R^2) of the linear regression between RSFA and tSD_{hc}. $RSFA_{lf}$ refers to the frequency band 0.01-0.1 Hz, $RSFA_{hf}$ to the band 0.1-0.15 Hz and RSFA to the unfiltered time-series. Group mean values are reported with the standard deviation across participants.

parameters only, since sequence-specific parameters were kept identical for all acquisitions (see Eq. 65). On the other hand, RSFA does not uniquely depend on baseline parameters but also on the dynamic changes of CBF and CBV. Thus, the lower correlation might be on one hand attributable to the different physiological modulators of RSFA with respect to M but could also be a result of the higher variability of the M parameter, which is the result of a division between different contrasts and, hence, inherently noisier than a pure contrast.

The low-frequency and high-frequency bands considered in this study were shown to scale similarly with depth. The low-frequency band (0.01-0.1 Hz) is usually considered to be the one where the relevant neuronal activity takes place (Biswal et al., 1995; Margulies et al., 2010). It is obvious from our laminar profile, though, that this band is dominated by the superficial draining vasculature, which does not correspond to the region where the neuronal activity takes place (Turner, 2002). While this does not exclude the possibility that the neuronal component is present in the same band, it is likely to add some confounds to it (Markuerkiaga et al., 2016). The high frequency band (0.1-0.15 Hz) selected in our analysis is somewhat narrower than the 'traditional' high-frequency band (0.1-0.25 Hz), whose definition is based on typical fMRI studies with T_R on the order of 2 s. Simi-

PARTICIPANT	R^2		
	M-RSFA	M-RSFA$_{lf}$	M-RSFA$_{hf}$
1	0.48	0.57	0.62
2	0.61	0.28	0.23
3	0.82	0.80	0.75
4	0.38	0.19	0.14
5	0.70	0.93	0.50
6	0.46	0.50	0.51
7	0.74	0.74	0.84
8	0.92	0.90	0.92
9	0.44	0.46	0.46
MEAN	0.62 ± 0.19	0.60 ± 0.26	0.55 ± 0.26

Table 6: Correlation coefficients (R^2) of the linear regression between RSFA and the calibration factor M. RSFA$_{lf}$ refers to the frequency band 0.01-0.1 Hz, RSFA$_{hf}$ to the band 0.1-0.15 Hz and RSFA to the unfiltered timeseries. Group mean values are reported with the standard deviation across participants.

larly to lower frequencies, the high-frequency band is dominated by the pial surface, therefore, yielding almost identical correlations with tSD$_{hc}$ and M. Given the spatial nature of pial vein contamination, it is reasonable to expect that the correlation would be disrupted as soon as its relative contribution becomes negligible and the shape of the depth-dependent RSFA starts flattening out.

Based on our results, RSFA seems to provide a good substitute of the amplitude of the hypercapnia-induced signal changes for scaling the BOLD response. In the assumption of isometabolism of the hypercapnia challenge, RSFA and tSD$_{hc}$ are likely to be similarly driven by reactivity features of the underlying vasculature (both following a relation similar to Eq. 80) and, therefore, look like scaled versions of each other.

Although the agreement between RSFA and M is good, an equally strong statement cannot be made in this case, due to their different physiological origin, with M depending solely on baseline parameters, given that it is accurately measured (Griffeth and Buxton, 2011). In fact, the validation of RSFA with the M parameter might be not as straightforward as it seems (Lu et al., 2011). The calculation of M relies on several assumptions, whose validity is called into question, especially at high resolution. Such potential pitfalls include the valid-

ity of a Grubb-like law and the coupling exponent α; the assumption of isometabolism for the hypercapnia challenge; and the validity of the Fick's principle on a laminar basis.

Scaling methods based on normalization with BOLD-based perfusion sensitive scans, without additional CBF or CBV recordings, cannot deliver $\Delta CMRO_2$ estimates. This is also the case for the normalization with RSFA. For certain application though, such as submillimeter resolution or high field studies, the traditional way of obtaining $\Delta CMRO_2$ with a separate scan delivering CBF changes might be difficult to achieve reliably and with sufficient tSNR, leading to corrupted $\Delta CMRO_2$ estimates. Thus, some applications would not be compromised by the lack of a $\Delta CMRO_2$ estimate and could still benefit from RSFA maps.

Finally, it must be noted that the application of any form of fMRI signal normalization across cortical depths is associated with limited interpretability:

- For instance, in the process of normalization with depth dependent physiological parameters, the activity in some cortical layers can be suppressed and undesirably underestimated. As such, upon normalization, the higher values of CVR, CBV_0 and CBV_v in upper cortical layers result in an reduced normalized fMRI signal change in those layers, despite the fact that the microvascular-induced response has the same magnitude (Huber et al., 2015a).

- When the fMRI signal is normalized, the resulting activity measure depends on additional estimated parameters as opposed to the non-normalized activity measures. Hence, due to the non-linear error propagation of multiple parameters during the normalization, the resulting normalized activity measure might be noisier.

- Here, we investigate the possibility of fMRI signal normalization by means of dividing fMRI responses with various measures of signal variability. This division is a nonlinear operation and can reshape the cortical profiles to look unfamiliar and harder to interprete. As such, in voxels where CVR is noisy and very small (e.g. with large partial voluming of WM), the denominator can become very small and the normalized fMRI signal change can become unphysiologically large.

9.4 CONCLUSION

We have shown that the laminar amplitude of spontaneous brain fluctuations resembles almost perfectly the scaling of the laminar amplitude of hypercapnia-induced signal changes, which are a marker for cerebrovascular reactivity. This result points to the fact that RSFA

can be used to replace the scaling factor tSD_{hc} used to normalize the BOLD response. Although of different physiological origin, the calibration parameter M also showed remarkable similarities with the RSFA profile. The shape of laminar BOLD signal changes reflects spatial variations in resting venous blood volume, which explains the similarity found in the laminar profiles of M, tSD_{hc} and RSFA, and the consequent strong correlations.

10

FREQUENCY SIGNATURE OF CORTICAL LAMINAR FMRI

3D GRE-EPI allows high resolution in both the spatial and the temporal dimension (as detailed in Chapter 5).
In this Chapter, temporal signal fluctuations of the BOLD response are analyzed at a submillimeter, subsecond scale.

BOLD signal responses at different cortical depths have been related to electroencephalography (EEG) signatures in the α-, β-, and γ-bands (Scheeringa et al., 2016) for task-driven neural activity changes. Similarly, in the current study, we investigate the hypothesis whether the frequency spectrum of resting-state BOLD signal fluctuations is predictive of the underlying vasculature. In particular, given the convergence of signals from different capillary beds (Turner, 2002), we hypothesized a higher characteristic frequency in the capillary bed than in the post capillary vessels, as if the vascular tree would act as a low-pass filter. The mechanism for this would be that the BOLD signal oscillations at the capillary bed would lose phase coherence in downstream vessels, either because the vessels are draining different territories that are themselves not coherent, or because of differences in length and flow rate for vessels draining the capillary bed.

We investigated our hypothesis by looking at the laminar fFA of the resting-state timeseries (Chapter 7). In order to minimize aliasing of cardiac and respiratory noise, and to pick up oscillations of neuronal origin over a relatively high bandwidth, a high temporal resolution was employed (volume repetition time of 994 ms) and a physiological noise correction applied.

Parts of this work have been presented at the 24th meeting of the International Society for Magnetic Resonance in Medicine in Honolulu, HI, USA, with the title "Frequency signature of cortical laminar fMRI" (Guidi et al., 2017).

10.1 MATERIALS AND METHODS

10.1.1 *Experimental setup and MRI acquisition parameters*

Ten healthy participants with no history of neurological disorder took part in the study. Each one of them gave written informed consent in accordance with procedures previously approved by the local ethics committee. Participants were asked to refrain from coffee and alcohol intake at least two hours prior to the experiment. All scans were performed on a MAGNETOM 7 T scanner (Siemens Healthineers,

Erlangen, Germany) with SC72 (70/200) gradient coil, and using a single-channel transmit, 32-channel receive head coil (Nova Medical, Wilmington, MA, USA).

A gradient-echo BOLD sequence with a three-dimensional (3D) readout (Poser et al., 2010) was used for the study. The nominal in-plane resolution was 0.75×0.75 mm^2, and the slice thickness was 1.5 mm. A total of 16 slices were acquired. The volume repetition time (T_R) was 994 ms, and the T_E was 30 ms. Other acquisition parameters were: flip angle 16°, in-plane partial Fourier factor 6/8, in-plane GRAPPA acceleration factor 4, bandwidth 782 Hz/Px, echo spacing 1.44 ms, RF duration 2.56 ms, excitation pulse bandwidth time product 25. Physiological recordings of respiration and cardiac pulsation at a sampling rate of 20 ms were embedded in the sequence. To reduce through-plane partial voluming artefacts coming from the non-isotropic voxel dimensions, the imaging slab was oriented as to best align to the GM ribbon of the hand-knob in M1 of the left hemisphere and, hence, adapted to the local anatomy of each participant. The orientation was planned on previously acquired MP2RAGE (Marques et al., 2010) images of each participant, as previously described (Huber et al., 2016b). The external devices used for physiological recordings were a vendor-provided respiratory bellow and a plethysmograph placed on the right index finger.

The paradigm consisted of three resting-state runs acquired consecutively with no break in between. Each run lasted 9 minutes leading to a total resting-state experiment of 27 minutes. The resting-state acquisition was split into three runs with respectively preceding Larmor-frequency calibration adjustments and updates in order to minimize the low-frequency signal drift, which could represent the main cause of signal fluctuation in resting-state fMRI (Bianciardi et al., 2009). During the resting-state scan, participants were asked to stare at a fixation image and not to fall asleep.

10.1.2 *Pre- and postprocessing*

The preprocessing of the acquired datasets consisted of the following steps performed in the indicated order for each participant:

1. Physiological noise removal. Cardiac and respiratory signals were removed using AFNI's (Cox, 1996) RETROICOR implementation (Glover et al., 2000) via the command '3dretroicor'. The application of RETROICOR to 3D sequences has been shown in (Barry et al., 2012; Tijssen et al., 2014). Compared to the 2D case, in 3D acquisitions each point is acquired over a longer period of time (a few seconds vs. milliseconds for 3D and 2D sequences, respectively). The application of RETROICOR in the 3D case relies on the assumption that the cardiac and respiratory phases corresponding to the center of k-space are

assigned to the entire volume, as most of the contrast comes from k-space center (Caballero-Gaudes and Reynolds, 2016; Tijssen et al., 2014) and was shown to outperform RETROKCOR (Tijssen et al., 2014).

2. Motion correction. The three runs were corrected for rigid body motion using the option 'Realign: Estimate & Reslice' of SPM12 (http://www.fil.ion.ucl.ac.uk/spm/) and coregistered during the same step.

3. Grand mean scaling. Grand mean scaling was performed together with the removal of the first and second volume of each timeseries using FEAT of FSL (Jenkinson et al., 2012).

4. Concatenation. The three runs were concatenated according to the temporal order of their acquisition, and a high-pass filter limit of 0.01 Hz was applied to suppress residual slow signal drifts.

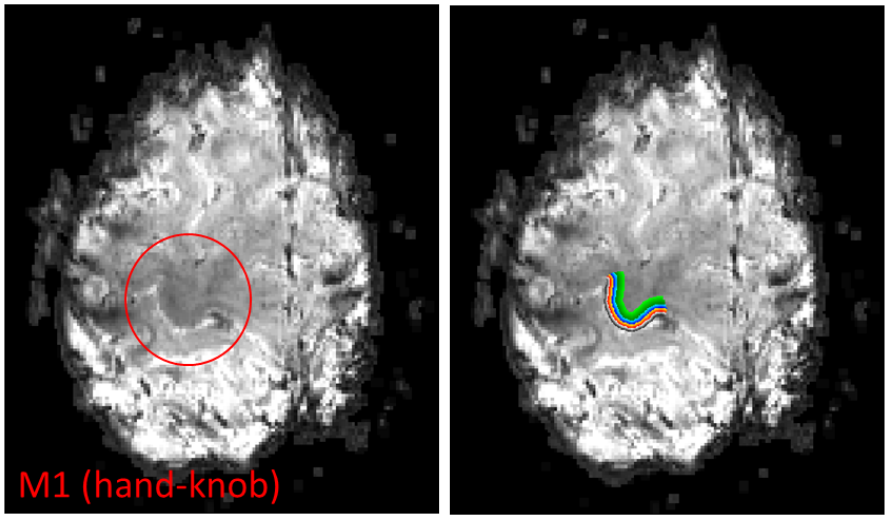

Figure 56: tSNR map of the motor hand region of the left hemisphere of one representative participant (red circle). Layering follows an equidistance approach starting from the CSF/GM interface.

The post-processing involved the following steps:

1. Layering. Layering was done directly in EPI space, exploiting the contrast of the temporal tSNR map for the definition of the CSF/GM surface. The WM/GM contrast for BOLD-based acquisitions is poor and does not allow a manual delineation. Therefore, only the border between GM and CSF was defined, and layers were grown following an equidistant approach (Fig. 56). The GM/WM border was reconstructed assuming an M1 GM thickness of 4 mm (Fischl and Dale, 2000). The images were resized by a factor of 25 (from a matrix size of 200×200 up to

1000 × 1000) in the xy-plane prior to the laminar segmentation (Guidi et al., 2016a). A total of 25 laminae were retained.

2. Laminar power spectrum calculation. The power spectrum of the timeseries was calculated and averaged across each lamina (Fig. 57a). The temporal resolution allowed to resolve frequencies up to 0.5 Hz (based on the Nyquist criterion).

3. Laminar fFA calculation. The fFA calculation followed the fALFF calculation approach (Zou et al., 2008) with some modifications. In the original approach, only the low-frequency band (0.01-0.08 Hz) is considered. Here, we included frequencies up to 0.4 Hz split into 0.1 Hz-wide bins. Additionally, in order to avoid residual biases, the power spectrum for every considered frequency band was not scaled by the power of the whole frequency range but by the power of the frequency band 0.4-0.5 Hz, which was the least affected by physiological noise contributions (Fig. 57b).

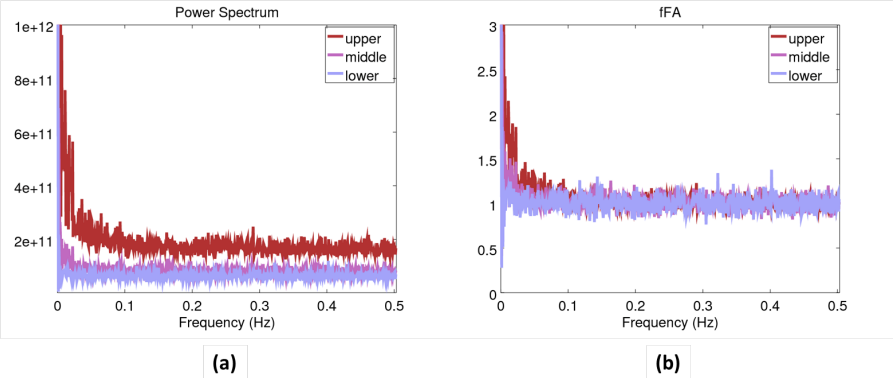

Figure 57: (a) Power spectrum and (b) fFA calculated at three different cortical depths. 'Upper' refers to the 8 laminae closer to the cortical surface, 'middle' to the 8 laminae in the middle of the cortex, and 'lower' to the 8 laminae closer to WM. Depicted fluctuation spectra refer to fMRI data after the application of physiological noise correction with RETROICOR. The y-axis in panel (a) refers to fluctuation power in arbitrary units.

10.2 RESULTS

One participant was excluded from further analysis due to excessive motion during the functional acquisition (volume-to-volume displacement above 3 mm). The mean framewise displacement for the group was found to be 0.19 ± 0.03 mm (Power et al., 2014).

Fig. 58 shows the fFA map for one participant for the band 0.01-0.1 Hz (and, hence, somehow comparable to fALFF). Fig. 58a shows the tSNR map, where the large draining veins can be identified as dark spots. Figure 58b shows the unthresholded fFA map and Figure 58c

the thresholded map, to highlight its specificity to the pial vasculature.

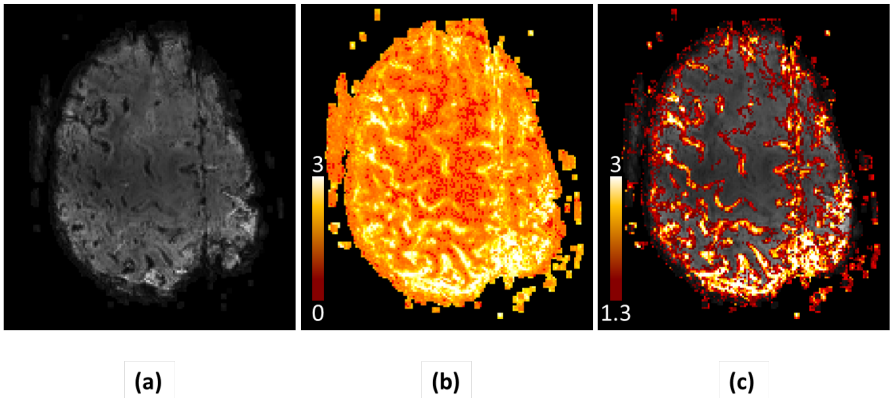

Figure 58: fFA for the frequency band 0.01-0.1 Hz. The tSNR map for one participant is shown, where the draining veins can be identified as darker spots (a). The (b) unthresholded and (c) thresholded fFA maps for the low frequency band are shown. Most of the power is found in correspondence of the large draining veins. Units of color scales refer to the fFA relative to the fluctuation power of the frequency band 0.4-0.5 Hz.

Figs. 59a and 59b show the laminar fFA with and without the low frequency band profile, respectively (not shown in Fig. 59b for better visualization of the dynamic range of the y-axis). The errorbars refer to the standard error of the mean (SEM) across nine participants. The x-axis shows the normalized cortical depth, with 0 corresponding to the border with CSF and 1 to the border with WM. The power for frequencies below 0.1 Hz is dominant at all depths, and peaks at the surface. The power in the frequency range between 0.1 and 0.3 Hz is still dominated by the pial surface (Fig. 59b), but the contribution is gradually reduced. The frequency band 0.4-0.5 Hz was used for scaling and it is not shown in the plots, as it would result in a flat line at $y = 1$.

Figs. 60a and 60b show the frequency sub-composition of the dominant low frequency bands 0.01-0.1 Hz and 0.1-0.2 Hz, respectively at steps of 0.02 Hz. Apart from the amplitude, the relative shape of the band 0.01-0.1 Hz is similar for all bins considered. The shapes of the sub-bands shown in Fig. 60b vary with increasing frequency, with a decreasing contribution from upper laminae compared to deeper laminae.

A small peak in the fFA in middle layers (corresponding to roughly 0.6 of the normalize depth shown in the figures and tentatively assigned to the histological layer V) is visible for all the frequencies considered (Figs. 59 and 60). The peak is shown to decrease in amplitude with increasing frequency, but relatively more slowly than the pial peak reduction.

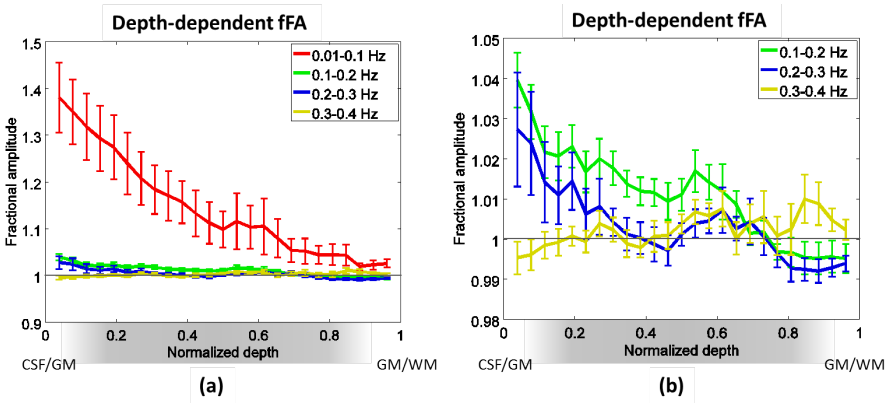

Figure 59: Laminar fFA for (a) the band 0.01-0.4 Hz and (b) 0.1-0.4 Hz split up into sub-bands 0.1 Hz wide. Slow components of the fMRI signal fluctuations are strongest in superficial locations. The fFA for the frequency band 0.4-0.5 Hz is not displayed, as it would result in a flat line. The errorbars refer to the SEM across participants. Note the different scaling of the y-axis.

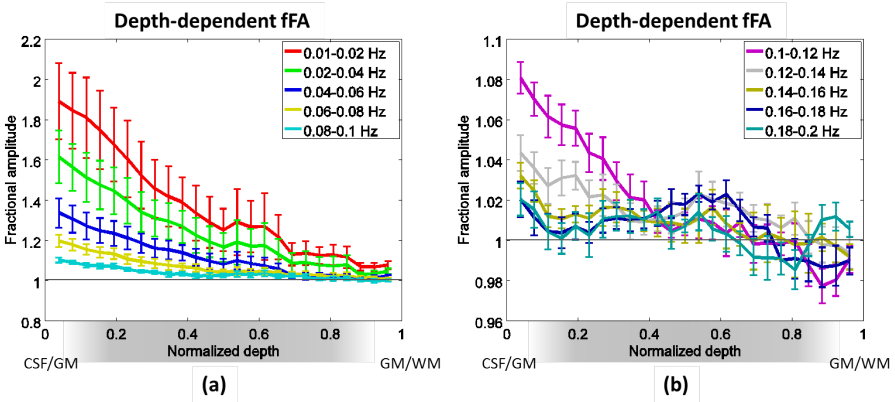

Figure 60: Laminar fFA for (a) the band 0.01-0.1 Hz and (b) 0.1-0.2 Hz split up into sub-bands 0.02 Hz wide. The relative contribution of superficial cortical depths decreases with increasing fluctuation frequencies. Fast fluctuation frequencies show higher relative fFA in middle cortical depths. The errorbars refer to the SEM across participants.

10.3 DISCUSSION

The profile of the fractional amplitude of resting-state fluctuations (Fig. 59) shows that the low-frequency band (0.01-0.1 Hz) dominates throughout the GM, peaking at the pial surface and decaying with depth. This feature was observed for each individual participant and is not a result of the averaging. Figs. 59 and 60 show that the curve starts flattening out for frequencies equal to or higher than 0.1 Hz. All frequency bands (Fig. 59) show a minimal peak or shoulder in deeper GM, located at a normalized depth of approximately 0.6. The specificity of the low-frequency band to the pial veins has implications for connectivity studies based on resting-state fMRI, in line with previous observations (Wise et al., 2004). The motivation behind this study was to investigate the possibility of characterizing the capillary and venous compartments based on their characteristic frequencies of BOLD spontaneous oscillations. The results showed that a clear distinction is not straightforward and that most of the spectral power presumably coming from neuronal-driven processes fall in the same frequency range as that of the pial veins (mostly at frequencies below 0.1 Hz).

In line with previous studies, we chose the hand-knob region of M1 to test our hypothesis (Huber et al., 2015a; Trampel et al., 2012) because the GM ribbon is relatively thick (up to 4 mm) and allows the accommodation of more voxels (Fischl and Dale, 2000).

The peak visible at a normalized depth of 0.6 (Figs. 59 and 60) could reflect a slightly higher power in correspondence of layer V, which is persistent across all frequency bands considered and does not completely flatten out (Fig. 59b).

The fact that the peak is not particularly pronounced may be expected, given that the range of oxygenation changes in GM is restricted with respect to the dynamic range available for oxygenation changes at the pial surface. This difference in intensity would be even exacerbated if the compartment that undergoes the fastest oscillations is the arterial/arteriolar one, due to its almost full oxygenation.

Moreover, the GM peak is still dominated by the same frequency band that characterizes the venous contribution. This is in line with a recent study that shows that the late response (draining veins) and the early response (microvasculature) oscillate at the same frequency upon visual flickering stimulus (Lewis et al., 2016) and can be detected above the limit imposed by the canonical linear model of the HRF. Although these results were obtained from the V1, a similar vascular arrangement can be expected in M1. In our case, the participants were not exposed to any fast-oscillating external stimulus, which could further restrict the neuronal oscillation to be located in a lower frequency range compared to (Lewis et al., 2016).

Another concern for resting-state studies comes from the physiological noise contamination. Polimeni et al. showed that the noise amplitude in GM has strong depth-dependent features in the whole brain (Polimeni et al., 2015). The performance of the noise cleaning is not always optimal and depends on a variety of factors, from the quality of the recorded physiological traces up to the cleaning strategy used (Bright et al., 2016; Caballero-Gaudes and Reynolds, 2016). Therefore, including more cleaning steps in the preprocessing might improve detectability (Caballero-Gaudes and Reynolds, 2016). Other possibilities for circumventing some sources of noise in the frequency of interest, would be (i) increasing the temporal resolution in order to resolve the cardiac peak (Viessmann et al., 2016), which would come to a cost for the spatial resolution and signal strength, or (ii) employing other functional contrasts if the application allows for a lower temporal resolution (Guidi et al., 2016a; Huber et al., 2016a,b).

10.4 CONCLUSION

This work focused on the characterization of depth-dependent BOLD responses and tested the hypothesis whether a characteristic frequency exists for different laminae in the range accessible to fMRI studies.

It was found that the dominant part of the low-frequency fluctuations corresponds to the pial surface, which is located away from the site of the dominant metabolic activity. Elimination of the pial frequency contribution through band-pass filtering is not straightforward, as this could partly eliminate the neuronal component contained in the BOLD signal within the GM. In order to avoid confounds from non-neuronal components, additional functional measures based on CBV or CBF changes might be the methods of choice.

Part V

CONCLUSION

11 CONCLUSION

Throughout this work, three methods were tested in order to improve spatial specificity of the BOLD response.
It was shown that the tSNR was sufficient for targeting the research questions on a laminar level, and that a resolution of $0.8 \times 0.8 \times 1.5$ mm^3 was suitable for discerning laminar responses in the human motor cortex.

The development and application of the modified dilution model (Chapter 8) represents, to the best of our knowledge, the first attempt to use VASO data in combination with the Davis model on a laminar level. It was shown that $CMRO_2$ changes during a motor task can be obtained within a 15 min scan time, if tasks (finger tapping and hypercapnia) and contrast acquisitions (BOLD and VASO) are interleaved. The obtained mean $CMRO_2$ changes of $(30 \pm 7)\%$ are in accordance with previously reported values, and the depth-dependent profile may be indicative of a differential layer activity. The obtained mean M parameter of $(11 \pm 2)\%$ is also in accordance with the literature and, for the first time, it was shown that values are higher at the cortical surface and decrease with depth. The two different scalings proposed, i. e., by means of normalization with the signal amplitude of the hypercapnia challenge (for BOLD and VASO) and by means of the M parameter, yield different profiles, in accordance with the fact that they correct for different components (the vascular reactivity and the baseline, respectively). Nevertheless, both seem to be more specific to the parenchyma than the uncorrected BOLD response.

The resting-state based scaling of task responses, known from lower resolution studies, was validated at submillimeter voxel sizes (Chapter 9). A high correlation with the hypercapnia-induced BOLD response profile was observed for all participants analyzed. The good correlation with the calibration parameter M indicates a similarity in the depth-dependent features of baseline parameters and vascular reactivity properties, as well. This observation confirms that BOLD signal changes are highly weighted towards the venous vasculature.

The investigation of the frequency composition of layers (Chapter 10) indicates that the low-frequency band (0.01-0.1 Hz), which is considered to be the one reflecting neuronal oscillations, is highly contaminated by the pial vasculature, but is also dominant in gray matter. Higher frequencies might be, on the other hand, more predictive of deeper layers, but the power in those frequencies is lower and might be more difficult to detect. Therefore, our initial assumption of a "vascular filter" does not seem to be fully supported by the data due

to the noise levels. The noise levels for higher frequencies might be related to the fact that hemodynamics is dampening the HRF at increasing oscillation frequency, together with the fact that the baseline dHb and CBV levels in the microvasculature are lower than the one in the venous vasculature and, therefore, the responses ought to be smaller.

11.1 OUTLOOK

At the time of writing this thesis, layer-dependent fMRI in humans could be considered to be at its initial stage, although it is markedly attracting more and more attention, and the number of published papers per year is rapidly increasing.

BOLD pitfalls become particularly penalizing on a laminar level. For this reason, further improvements to the techniques presented here would be beneficial.

Even if the results from the modified Davis model are reassuring, many assumptions were made, and any further validation can make $CMRO_2$ estimations more accurate. For example, measuring CBF at high resolution, instead of calculating it from a power-law relationship, would yield more accurate data, and also make the model applicable in cases where the CBF-CBV coupling is disrupted.

Regarding the scaling of task data with resting-state fMRI data, a validation study could be envisaged. This would test the inter-subject variability and could also be conducted longitudinally. If the stability of the technique is validated, it could be easily added to BOLD acquisitions.

The study of frequency composition of cortical laminae would benefit from a validation study as well. BOLD data, even at coarser resolutions, could be bandpass filtered and tested for differential contributions from larger veins.

A more general limitation comes from the overall low signal to noise ratio available in high resolution studies, which allows investigation of tasks producing strong responses only, such as finger tapping and hypercapnia. Averaging within laminae helps increase the signal and seems the most convenient way of dealing with high resolution data. However, ideally, this averaging may be dismissed as soon as the SNR is sufficient for voxelwise analyses. At the time being, a 3D readout for BOLD and VASO seems to be a good acquisition strategy for high resolution studies, but it suffers from physiological noise artefacts. Combining it with prospective motion correction routines may improve the results substantially.

Moreover, increased field strengths could deliver more functional contrast. A field strength of 9.4 T is currently available, and successful experiments are being performed. Our work could probably benefit from higher field strengths as well.

Finally, a clear and detailed link between anatomical, cellular and vascular features is crucial for the whole field of fMRI, and even essential for layer dependent studies. Knowing exactly the dynamics of vasodilatory and vasoconstrictive stimuli initiation and propagation, the role of neurotransmitters and the exact scale of flow regulation may clarify which technique is the best indicator of neuronal activity.

BIBLIOGRAPHY

D. C. Alsop, J. A. Detre, X. Golay, M. Günther, J. Hendrikse, L. Hernandez-Garcia, H. Lu, B. J. Macintosh, L. M. Parkes, M. Smits, M. J. P. Van Osch, D. J. J. Wang, E. C. Wong, and G. Zaharchuk. Recommended implementation of arterial spin-labeled Perfusion mri for clinical applications: A consensus of the ISMRM Perfusion Study group and the European consortium for ASL in dementia. *Magnetic Resonance in Medicine*, 73(1):102–116, 2015. ISSN 15222594. doi: 10.1002/mrm.25197.

P. A. Bandettini. Twenty years of functional MRI: the science and the stories. *NeuroImage*, 62(2):575–88, aug 2012. ISSN 1095-9572. doi: 10.1016/j.neuroimage.2012.04.026. URL http://www.ncbi.nlm.nih.gov/pubmed/22542637.

P. A. Bandettini and E. C. Wong. A hypercapnia-based normalization method for improved spatial localization of human brain activation with fMRI. *NMR in biomedicine*, 10(4-5):197–203, 1997. ISSN 0952-3480. URL http://www.ncbi.nlm.nih.gov/pubmed/9430348.

P. A. Bandettini, E. C. Wong, R. S. Hinks, R. S. Tikofsky, and J. S. Hyde. Time course EPI of human brain functioning during task activation. *Magnetic Resonance Medicine*, 25:390–397, 1992.

R. L. Barry, S. C. Strother, and J. C. Gore. Complex and magnitude-only preprocessing of 2D and 3D BOLD fMRI data at 7 T. *Magnetic Resonance in Medicine*, 67(3):867–871, 2012. ISSN 07403194. doi: 10.1002/mrm.23072.

M. Barth, F. Breuer, P. J. Koopmans, D. G. Norris, and B. A. Poser. Simultaneous multislice (SMS) imaging techniques. *Magn Reson Med*, 81:n/a–n/a, 2015. ISSN 07403194. doi: 10.1002/mrm.25897. URL http://www.ncbi.nlm.nih.gov/pubmed/26308571{%}5Cnhttp://doi.wiley.com/10.1002/mrm.25897.

M. A. Bernstein, K. F. King, and X. J. Zhou. *Handbook of MRI Pulse Sequences*. Elsevier, 2004.

M. Bianciardi, M. Fukunaga, P. van Gelderen, S. G. Horovitz, J. A. de Zwart, K. Shmueli, and J. H. Duyn. Sources of functional magnetic resonance imaging signal fluctuations in the human brain at rest: a 7 T study. *Magnetic Resonance Imaging*, 27(8):1019–1029, 2009. ISSN 0730725X. doi: 10.1016/j.mri.2009.02.004. URL http://dx.doi.org/10.1016/j.mri.2009.02.004.

B. Biswal, F. Z. Yetkin, V. M. Haughton, and J. S. Hyde. Functional connectivity in the motor cortex of resting human brain using echo-planar MRI. *Magnetic resonance in medicine : official journal of the Society of Magnetic Resonance in Medicine / Society of Magnetic Resonance in Medicine*, 34(4):537–41, 1995. ISSN 0740-3194. doi: 10.1002/mrm.1910340409. URL http://www.ncbi.nlm.nih.gov/pubmed/8524021.

B. B. Biswal, S. S. Kannurpatti, and B. Rypma. Hemodynamic scaling of fMRI-BOLD signal: validation of low-frequency spectral amplitude as a scalability factor. *Magnetic resonance imaging*, 25 (10):1358–69, dec 2007. ISSN 0730-725X. doi: 10.1016/j.mri.2007.03.022. URL http://www.pubmedcentral.nih.gov/articlerender.fcgi?artid=2701471{&}tool=pmcentrez{&}rendertype=abstract.

P. Blinder and K. Uludağ. Linking brain vascular physiology to hemodynamic response in ultra-high field MRI. *NeuroImage*, 2016. ISSN 10959572. doi: 10.1016/j.neuroimage.2017.02.063.

F. Bloch, W. W. Hansen, and M. Packard. The nuclear induction experiment. *Physical Review*, 70(7-8):474–485, 1946. ISSN 0031899X. doi: 10.1103/PhysRev.70.474.

N. P. Blockley, V. E. M. Griffeth, A. B. Simon, and R. B. Buxton. A review of calibrated blood oxygenation level-dependent (BOLD) methods for the measurement of task-induced changes in brain oxygen metabolism. *NMR in biomedicine*, 26 (8):987–1003, aug 2013. ISSN 1099-1492. doi: 10.1002/nbm.2847. URL http://www.pubmedcentral.nih.gov/articlerender.fcgi?artid=3639302{&}tool=pmcentrez{&}rendertype=abstract.

K. T. Bluestein, D. Pitt, S. Sammet, C. R. Zachariah, U. Nagaraj, M. V. Knopp, and P. Schmalbrock. Detecting cortical lesions in multiple sclerosis at 7 T using white matter signal attenuation. *Magnetic Resonance Imaging*, 30(7):907–915, 2012. ISSN 0730725X. doi: 10.1016/j.mri.2012.03.006. URL http://dx.doi.org/10.1016/j.mri.2012.03.006.

J. Bodurka, F. Ye, N. Petridou, K. Murphy, and P. A. Bandettini. Mapping the MRI voxel volume in which thermal noise matches physiological noise-Implications for fMRI. *NeuroImage*, 34(2):542–549, 2007. ISSN 10538119. doi: 10.1016/j.neuroimage.2006.09.039.

Y. Bohraus, N. Logothetis, and J. Goense. High resolution CMRO2 in visual cortex of Macaca mulatta. In *Proceedings of the 19th Annual Meeting of the ISMRM*, page 3599, Montreal, Quebec, Canada, 2011.

S. T. Bok. Der Einfluß der in den Furchen und Windungen auftretenden Krümmungen der Großhirnrinde auf die Rindenarchitekt. *Z Gesamte Neurol. Psychiatr.*, 12:682–750, 1929.

R. N. Boubela, K. Kalcher, W. Huf, C. Kronnerwetter, P. Filzmoser, and E. Moser. Beyond Noise: Using Temporal ICA to Extract Meaningful Information from High-Frequency fMRI Signal Fluctuations during Rest. *Frontiers in human neuroscience*, 7 (May):168, jan 2013. ISSN 1662-5161. doi: 10.3389/fnhum.2013.00168. URL http://www.pubmedcentral.nih.gov/articlerender.fcgi?artid=3640215{&}tool=pmcentrez{&}rendertype=abstract.

F. A. Breuer, M. Blaimer, R. M. Heidemann, M. F. Mueller, M. A. Griswold, and P. M. Jakob. Controlled aliasing in parallel imaging results in higher acceleration (CAIPIRINHA) for multi-slice imaging. *Magnetic resonance in medicine : official journal of the Society of Magnetic Resonance in Medicine / Society of Magnetic Resonance in Medicine*, 53(3):684–91, mar 2005. ISSN 0740-3194. doi: 10.1002/mrm.20401. URL http://www.ncbi.nlm.nih.gov/pubmed/15723404.

M. G. Bright and K. Murphy. Is fMRI "noise" really noise? Resting state nuisance regressors remove variance with network structure. *NeuroImage*, 114:158–169, 2015. ISSN 10959572. doi: 10.1016/j.neuroimage.2015.03.070. URL http://dx.doi.org/10.1016/j.neuroimage.2015.03.070.

M. G. Bright, C. R. Tench, and K. Murphy. Potential pitfalls when denoising resting state fMRI data using nuisance regression. *NeuroImage*, (December 2016):1–10, 2016. ISSN 10538119. doi: 10.1016/j.neuroimage.2016.12.027. URL http://linkinghub.elsevier.com/retrieve/pii/S1053811916307480.

D. P. Bulte, M. Kelly, M. Germuska, J. Xie, M. a. Chappell, T. W. Okell, M. G. Bright, and P. Jezzard. Quantitative measurement of cerebral physiology using respiratory-calibrated MRI. *NeuroImage*, 60(1):582–91, mar 2012. ISSN 1095-9572. doi: 10.1016/j.neuroimage.2011.12.017. URL http://www.ncbi.nlm.nih.gov/pubmed/22209811.

R. B. Buxton. *Introduction to functional magnetic resonance imaging: principles and techniques*. Cambridge University Press, 2009. ISBN 9780521899956.

R. B. Buxton. Dynamic models of BOLD contrast. *NeuroImage*, 62(2):953–61, aug 2012. ISSN 1095-9572. doi: 10.1016/j.neuroimage.2012.01.012. URL http://www.pubmedcentral.nih.gov/articlerender.fcgi?artid=3545646{&}tool=pmcentrez{&}rendertype=abstract.

R. B. Buxton. The physics of functional magnetic resonance imaging (fMRI). *Reports on progress in physics. Physical Society (Great Britain)*, 76(9):096601, sep 2013. ISSN 1361-6633. doi: 10.1088/0034-4885/76/9/096601. URL http://www.ncbi.nlm.nih.gov/pubmed/24006360.

R. B. Buxton, E. C. Wong, and L. R. Frank. Dynamics of blood flow and oxygenation changes during brain activation: the balloon model. *Magnetic resonance in medicine : official journal of the Society of Magnetic Resonance in Medicine / Society of Magnetic Resonance in Medicine*, 39(6):855–64, jun 1998. ISSN 0740-3194. URL http://www.ncbi.nlm.nih.gov/pubmed/9621908.

R. B. Buxton, K. Uludag, D. J. Dubowitz, and T. T. Liu. Modeling the hemodynamic response to brain activation. *NeuroImage*, 23 Suppl 1: S220–33, jan 2004. ISSN 1053-8119. doi: 10.1016/j.neuroimage.2004.07.013. URL http://www.ncbi.nlm.nih.gov/pubmed/15501093.

C. Caballero-Gaudes and R. C. Reynolds. Methods for cleaning the BOLD fMRI signal. *NeuroImage*, (December):0–1, 2016. ISSN 10959572. doi: 10.1016/j.neuroimage.2016.12.018. URL http://dx.doi.org/10.1016/j.neuroimage.2016.12.018.

B. Cauli. Revisiting the role of neurons in neurovascular coupling. *Frontiers in Neuroenergetics*, 2(June):1–8, 2010. ISSN 16626427. doi: 10.3389/fnene.2010.00009. URL http://journal.frontiersin.org/article/10.3389/fnene.2010.00009/abstract.

M. Caulo, C. Briganti, P. A. Mattei, B. Perfetti, A. Ferretti, G. L. Romani, A. Tartaro, and C. Colosimo. New morphologic variants of the hand motor cortex as seen with MR imaging in a large study population. *American Journal of Neuroradiology*, 28(8):1480–1485, 2007. ISSN 01956108. doi: 10.3174/ajnr.A0597.

J. J. Chen and G. B. Pike. BOLD-specific cerebral blood volume and blood flow changes during neuronal activation in humans. *NMR in biomedicine*, 22(10):1054–62, dec 2009. ISSN 1099-1492. doi: 10.1002/nbm.1411. URL http://www.ncbi.nlm.nih.gov/pubmed/19598180.

J. J. Chen and G. B. Pike. MRI measurement of the BOLD-specific flow-volume relationship during hypercapnia and hypocapnia in humans. *NeuroImage*, 53(2):383–91, dec 2010. ISSN 1095-9572. doi: 10.1016/j.neuroimage.2010.07.003. URL http://www.ncbi.nlm.nih.gov/pubmed/20624474.

Y. Chen and T. B. Parrish. Caffeine dose effect on activation-induced BOLD and CBF responses. *NeuroImage*, 46(3):577–583, 2009. ISSN 10538119. doi: 10.1016/j.neuroimage.2009.03.012. URL http://dx.doi.org/10.1016/j.neuroimage.2009.03.012.

E. R. Cohen, E. Rostrup, K. Sidaros, T. E. Lund, O. B. Paulson, K. Ugurbil, and S.-G. Kim. Hypercapnic normalization of {{}BOLD{}} f{{}MRI{}}: comparison across field strengths and pulse sequences. *Neuroimage*, 23(2):613–624, 2004. ISSN 1053-8119. doi: 10.1016/j.neuroimage.2004.06.021. URL http://dx.doi.org/10.1016/j.neuroimage.2004.06.021.

R. C. Collins. Use of cortical circuits during focal penicillin seizures: An autoradiographic study with [14C]deoxyglucose. *Brain Research*, 150(3):487–501, 1978. ISSN 00068993. doi: 10.1016/0006-8993(78)90815-6.

S. Conolly, D. Nishimura, A. Macovski, and G. Glover. Variable-rate selective excitation. *Journal of Magnetic Resonance (1969)*, 78(3):440–458, 1988. ISSN 00222364. doi: 10.1016/0022-2364(88)90131-X.

R. W. Cox. AFNI: software for analysis and visualization of functional magnetic resonance neuroimages. *Computers and Biomedical Research*, 29(3):162—-173, 1996.

F. R. Cretti, P. E. Summers, and C. a. Porro. Multi-shot turbo spin-echo for 3D vascular space occupancy imaging. *Magnetic resonance imaging*, 31(6):875–81, jul 2013. ISSN 1873-5894. doi: 10.1016/j.mri.2013.03.008. URL http://www.ncbi.nlm.nih.gov/pubmed/23602727.

T. L. Davis, K. K. Kwong, R. M. Weisskoff, and B. R. Rosen. Calibrated functional MRI: mapping the dynamics of oxidative metabolism. *Proceedings of the National Academy of Sciences of the United States of America*, 95(4):1834–9, feb 1998. ISSN 0027-8424. URL http://www.pubmedcentral.nih.gov/articlerender.fcgi?artid=19199{&}tool=pmcentrez{&}rendertype=abstract.

J. A. De Zwart, P. Van Gelderen, P. Kellman, and J. H. Duyn. Application of sensitivity-encoded echo-planar imaging for blood oxygen level-dependent functional brain imaging. *Magnetic Resonance in Medicine*, 48(6):1011–1020, 2002. ISSN 07403194. doi: 10.1002/mrm.10303.

M. J. Donahue, M. R. Juttukonda, and J. M. Watchmaker. Noise concerns and post-processing procedures in cerebral blood flow (CBF) and cerebral blood volume (CBV) functional magnetic resonance imaging. *NeuroImage*, 2016. ISSN 1095-9572. doi: 10.1016/j.neuroimage.2016.09.007. URL http://www.ncbi.nlm.nih.gov/pubmed/27622397.

I. D. Driver, E. L. Hall, S. J. Wharton, S. E. Pritchard, S. T. Francis, and P. a. Gowland. Calibrated BOLD using direct measurement of changes in venous oxygenation. *NeuroImage*, 63(3):1178–87, nov 2012. ISSN 1095-9572. doi: 10.1016/j.neuroimage.2012.08.045. URL http://www.pubmedcentral.nih.gov/articlerender.fcgi?artid=3485568{&}tool=pmcentrez{&}rendertype=abstract.

H. M. Duvernoy. *The Human Brain: Surface, Blood Supply, and Three-Dimensional Sectional Anatomy*. Springer-Verlag Wien New York, 2nd ed. edition, 1999.

H. M. Duvernoy, S. Delon, and J. L. Vannson. Cortical blood vessels of the human brain. *Brain Research Bulletin*, 7(5):519–578, 1981. ISSN 0361-9230. URL http://www.ncbi.nlm.nih.gov/pubmed/7317796.

C. Eichner, L. L. Wald, and K. Setsompop. A low power radiofrequency pulse for simultaneous multislice excitation and refocusing. *Magnetic Resonance in Medicine*, 72(4):949–958, 2014. ISSN 15222594. doi: 10.1002/mrm.25389.

A. Eklund, T. E. Nichols, and H. Knutsson. Cluster failure: Why fMRI inferences for spatial extent have inflated false-positive rates. *Proceedings of the National Academy of Sciences*, page 201602413, 2016. ISSN 0027-8424, 1091-6490. doi: 10.1073/pnas.1602413113. URL http://www.pnas.org/content/early/2016/06/27/1602413113{%}7B{%}25{%}7D5Cnhttp://www.ncbi.nlm.nih.gov/pubmed/27357684{%}7B{%}25{%}7D5Cnhttp://www.pnas.org/content/early/2016/06/27/1602413113.full.

A. D. Elster. Questions and answers in MRI, 2017. URL mri-q.com.

R. R. Ernst and W. A. Anderson. Application of fourier transform spectroscopy to magnetic resonance. *Review of Scientific Instruments*, 37(1):93–102, 1966. ISSN 00346748. doi: 10.1063/1.1719961.

I. Estermann and O. Stern. Über die magnetische Ablenkung von Wasserstoffmolekülen und das magnetische Moment des Protons. II. *Zeitschrift für Physik A Hadrons and Nuclei*, 85(1):17—-24, 1933.

J. Fierstra, O. Sobczyk, a. Battisti-Charbonney, D. M. Mandell, J. Poublanc, a. P. Crawley, D. J. Mikulis, J. Duffin, and J. a. Fisher. Measuring cerebrovascular reactivity: what stimulus to use? *The Journal of physiology*, 591(Pt 23):5809–21, dec 2013. ISSN 1469-7793. doi: 10.1113/jphysiol.2013.259150. URL http://www.ncbi.nlm.nih.gov/pubmed/24081155.

B. Fischl and A. M. Dale. Measuring the thickness of the human cerebral cortex from magnetic resonance images. 2000(Track II), 2000.

P. T. Fox and M. E. Raichle. Focal physiological uncoupling of cerebral blood flow and oxidative metabolism during somatosensory stimulation in human subjects. *Proceedings of the National Academy of Sciences of the United States of America*, 83(February 1986):1140–4, 1986. ISSN 0027-8424. doi: 10.1073/pnas.83.4.1140. URL http://www.pubmedcentral.nih.gov/articlerender.fcgi?artid=323027{&}tool=pmcentrez{&}rendertype=abstract.

O. R. Frisch and O. Stern. Über die magnetische Ablenkung von Wasserstoffmolekülen und das magnetische Moment des Protons. I. *Zeitschrift für Physik A Hadrons and Nuclei*, 85(1):4—-16, 1933.

L. Gagnon, S. Sakad i, F. Lesage, J. J. Musacchia, J. Lefebvre, Q. Fang, M. a. Yucel, K. C. Evans, E. T. Mandeville, J. Cohen-Adad, J. R. Polimeni, M. a. Yaseen, E. H. Lo, D. N. Greve, R. B. Buxton, a. M. Dale, a. Devor, and D. a. Boas. Quantifying the Microvascular Origin of BOLD-fMRI from First Principles with Two-Photon Microscopy and an Oxygen-Sensitive Nanoprobe. *Journal of Neuroscience*, 35(8):3663–3675, 2015. ISSN 0270-6474. doi: 10.1523/JNEUROSCI.3555-14.2015. URL http://www.pubmedcentral.nih.gov/articlerender.fcgi?artid=4339366{&}tool=pmcentrez{&}rendertype=abstract.

N. D. Gai, S. L. Talagala, and J. A. Butman. Whole-brain cerebral blood flow mapping using 3D echo planar imaging and pulsed arterial tagging. *Journal of Magnetic Resonance Imaging*, 33(2):287–295, 2011. ISSN 10531807. doi: 10.1002/jmri.22437.

A. G. Gardener, P. A. Gowland, and S. T. Francis. Implementation of quantitative perfusion imaging using pulsed arterial spin labeling at ultra-high field. *Magnetic Resonance in Medicine*, 61(4):874–882, 2009. ISSN 07403194. doi: 10.1002/mrm.21796.

C. J. Gauthier, C. Madjar, F. B. Tancredi, B. Stefanovic, and R. D. Hoge. Elimination of visually evoked BOLD responses during carbogen inhalation: implications for calibrated MRI. *NeuroImage*, 54(2):1001–11, jan 2011. ISSN 1095-9572. doi: 10.1016/j.neuroimage.2010.09.059. URL http://www.ncbi.nlm.nih.gov/pubmed/20887792.

G. H. Glover, T.-q. Li, and D. Ress. Image-Based Method for Retrospective Correction of Physiological Motion Effects in fMRI: RETROICOR. 167(March):162–167, 2000.

J. Goense, H. Merkle, and N. K. Logothetis. High-resolution fMRI reveals laminar differences in neurovascular coupling between positive and negative BOLD responses. *Neuron*, 76(3):629–39, nov 2012. ISSN 1097-4199. doi: 10.1016/j.neuron.2012.09.019. URL http://www.ncbi.nlm.nih.gov/pubmed/23141073.

J. Goense, Y. Bohraus, and N. K. Logothetis. fMRI at High Spatial Resolution: Implications for BOLD-Models. *Frontiers in computational neuroscience*, 10(June):66, 2016. ISSN 1662-5188. doi: 10.3389/fncom.2016.00066. URL http://www.ncbi.nlm.nih.gov/pubmed/27445782{%}7B{%}25{%}7D5Cnhttp://www.pubmedcentral.nih.gov/articlerender.fcgi?artid=PMC4923185.

J. B. M. Goense, A. C. Zappe, and N. K. Logothetis. High-resolution fMRI of macaque V1. *Magnetic Resonance Imaging*, 25(6):740–747, 2007. ISSN 0730725X. doi: 10.1016/j.mri.2007.02.013.

K. Grgac, P. C. M. Van Zijl, and Q. Qin. Hematocrit and oxygenation dependence of blood 1H2O T1 at 7 tesla. *Magnetic Resonance in*

Medicine, 70(4):1153–1159, 2013. ISSN 07403194. doi: 10.1002/mrm.24547.

V. E. M. Griffeth and R. B. Buxton. A theoretical framework for estimating cerebral oxygen metabolism changes using the calibrated-BOLD method: modeling the effects of blood volume distribution, hematocrit, oxygen extraction fraction, and tissue signal properties on the BOLD signal. *NeuroImage*, 58(1):198–212, sep 2011. ISSN 1095-9572. doi: 10.1016/j.neuroimage.2011.05.077. URL http://www.pubmedcentral.nih.gov/articlerender.fcgi?artid=3187858{&}tool=pmcentrez{&}rendertype=abstract.

B. Y. R. L. Grubb, M. E. Raichle, J. O. Eichling, and M. M. Ter-Pogossian. The Effects of Changes in Paco 2 on Cerebral Blood Volume , Blood Flow , and Vascular Mean Transit Time. 11059, 1974.

M. Guidi, L. Huber, L. Lampe, C. J. Gauthier, and H. E. Möller. Layer-Dependent Calibrated BOLD Response in Human M1. In *Proceedings of the 23rd Annual Meeting of ISMRM, Toronto, ON, Canada*, page 0358, 2015.

M. Guidi, L. Huber, L. Lampe, C. J. Gauthier, and H. E. Möller. Lamina-dependent calibrated BOLD response in human primary motor cortex. *NeuroImage*, 141:250–261, 2016a. ISSN 10959572. doi: 10.1016/j.neuroimage.2016.06.030. URL http://dx.doi.org/10.1016/j.neuroimage.2016.06.030.

M. Guidi, L. Huber, L. Lampe, and H. E. Möller. Cortical Laminar Resting-State Fluctuations Scale with Hypercapnic Response. In *Proceedings of the 24th Annual Meeting of the ISMRM, Singapore*, page 0769, 2016b.

M. Guidi, I. Markuerkiaga, L. J. Bains, L. Huber, H. E. Möller, and D. G. Norris. Frequency signature of cortical laminar fMRI. In *Proceedings of the 25th Annual Meeting of the ISMRM, Honolulu, HI, USA*, page 0158, 2017.

E. M. Haacke, R. W. Brown, M. R. Thompson, and R. Venkatesan. Haacke - Magnetic Resonance Imaging - Physical Principles and Sequence Design.pdf, 1999. ISSN 00218979. URL http://www.amazon.fr/dp/0471351288.

C. N. Hall, C. Reynell, B. Gesslein, N. B. Hamilton, A. Mishra, B. A. Sutherland, F. M. O'Farrell, A. M. Buchan, M. Lauritzen, and D. Attwell. Capillary pericytes regulate cerebral blood flow in health and disease. *Nature*, 508(7494):55–60, 2014. ISSN 0028-0836. doi: 10.1038/nature13165. URL http://www.nature.com/doifinder/10.1038/nature13165.

E. Hamel. Perivascular nerves and the regulation of cerebrovascular tone. *Journal of applied physiology*, 100:1059–1064, 2006. doi: 10.1152/japplphysiol.01254.2005.Editorial.

H. V. Hare, N. P. Blockley, A. G. Gardener, S. Clare, and D. P. Bulte. Investigating the field-dependence of the Davis model: Calibrated fMRI at 1.5, 3 and 7T. *NeuroImage*, 112:189–196, 2015. ISSN 10538119. doi: 10.1016/j.neuroimage.2015.02.068. URL http://linkinghub.elsevier.com/retrieve/pii/S1053811915001937.

P. Herman, B. G. Sanganahalli, H. Blumenfeld, D. L. Rothman, and F. Hyder. Quantitative basis for neuroimaging of cortical laminae with calibrated functional MRI. *Proceedings of the National Academy of Sciences of the United States of America*, 110(37):15115–20, sep 2013. ISSN 1091-6490. doi: 10.1073/pnas.1307154110. URL http://www.pubmedcentral.nih.gov/articlerender.fcgi?artid=3773779{&}tool=pmcentrez{&}rendertype=abstract.

E. M. C. Hillman, A. Devor, M. B. Bouchard, A. K. Dunn, G. W. Krauss, J. Skoch, B. J. Bacskai, A. M. Dale, and D. a. Boas. Depth-resolved optical imaging and microscopy of vascular compartment dynamics during somatosensory stimulation. *NeuroImage*, 35(1):89–104, 2007. ISSN 10538119. doi: 10.1016/j.neuroimage.2006.11.032. URL http://dx.doi.org/10.1016/j.neuroimage.2006.11.032.

Y.-C. L. Ho, E. T. Petersen, I. Zimine, and X. Golay. Similarities and differences in arterial responses to hypercapnia and visual stimulation. *Journal of cerebral blood flow and metabolism : official journal of the International Society of Cerebral Blood Flow and Metabolism*, 31(2):560–571, 2011. ISSN 0271-678X. doi: 10.1038/jcbfm.2010.126. URL http://dx.doi.org/10.1038/jcbfm.2010.126.

R. D. Hoge, J. Atkinson, B. Gill, G. R. Crelier, S. Marrett, and G. B. Pike. Linear coupling between cerebral blood flow and oxygen consumption in activated human cortex. *Proceedings of the National Academy of Sciences of the United States of America*, 96(16):9403–8, aug 1999. ISSN 0027-8424. URL http://www.pubmedcentral.nih.gov/articlerender.fcgi?artid=17795{&}tool=pmcentrez{&}rendertype=abstract.

J. P. Hornack. The Basics of MRI, 2017, 2017. URL http://www.cis.rit.edu/htbooks/mri/inside.htm.

J. Hua, Q. Qin, M. J. Donahue, J. Zhou, J. J. Pekar, and P. C. van Zijl. Inflow-based vascular-space-occupancy (iVASO) MRI. *Magnetic Resonance in Medicine*, 66(1):40–56, 2011. ISSN 07403194. doi: 10.1002/mrm.22775. URL http://doi.wiley.com/10.1002/mrm.22775.

J. Hua, C. K. Jones, Q. Qin, and P. C. M. van Zijl. Implementation of vascular-space-occupancy MRI at 7T. *Magnetic resonance in medicine : official journal of the Society of Magnetic Resonance in Medicine / Society of Magnetic Resonance in Medicine*, 69(4):1003–13, apr 2013. ISSN 1522-2594. doi: 10.1002/mrm.24334. URL http://www.ncbi.nlm.nih.gov/pubmed/22585570.

L. Huber, J. Goense, A. J. Kennerley, D. Ivanov, S. N. Krieger, J. Lepsien, R. Trampel, R. Turner, and H. E. Möller. Investigation of the neurovascular coupling in positive and negative BOLD responses in human brain at 7T. *NeuroImage*, 97:349–362, aug 2014a. ISSN 10959572. doi: 10.1016/j.neuroimage.2014.04.022. URL http://www.ncbi.nlm.nih.gov/pubmed/24742920.

L. Huber, D. Ivanov, S. N. Krieger, M. N. Streicher, T. Mildner, B. a. Poser, H. E. Möller, and R. Turner. Slab-selective, BOLD-corrected VASO at 7 Tesla provides measures of cerebral blood volume reactivity with high signal-to-noise ratio. *Magnetic resonance in medicine : official journal of the Society of Magnetic Resonance in Medicine / Society of Magnetic Resonance in Medicine*, 72(1):137–48, jul 2014b. ISSN 1522-2594. doi: 10.1002/mrm.24916. URL http://www.ncbi.nlm.nih.gov/pubmed/23963641.

L. Huber, J. Goense, A. J. Kennerley, R. Trampel, M. Guidi, E. Reimer, D. Ivanov, N. Neef, C. J. Gauthier, R. Turner, and H. E. Möller. Cortical lamina-dependent blood volume changes in human brain at 7 T. *NeuroImage*, 107:23–33, 2015a. ISSN 1053-8119. doi: 10.1016/j.neuroimage.2014.11.046. URL http://dx.doi.org/10.1016/j.neuroimage.2014.11.046.

L. Huber, D. Ivanov, M. Guidi, R. Turner, K. Uludag, H. E. Möller, and B. a. Poser. HuberFunctional cerebral blood volumemapping with simultaneous multi-slice acquisition. *NeuroImage*, m, 2015b. ISSN 10959572. doi: 10.1016/j.neuroimage.2015.10.082.

L. Huber, D. Ivanov, M. Guidi, R. Turner, K. Uludag, H. E. Möller, and B. A. Poser. Functional cerebral blood volume mapping with simultaneous multi-slice acquisition. *NeuroImage*, 125:1159–1168, 2015c. ISSN 10959572. doi: 10.1016/j.neuroimage.2015.10.082.

L. Huber, D. A. Handwerker, J. Gonzales-Castillo, D. Jangraw, M. Guidi, D. Ivanov, B. A. Poser, J. Goense, and P. Bandettini. Effective Connectivity Measured with Layer-Dependent Resting-State Blood Volume FMRI in Humans. In *Proceedings of the 24th Annual Meeting of the ISMRM, Singapore*, page 0948, 2016a.

L. Huber, D. Ivanov, D. A. Handwerker, S. Marrett, M. Guidi, K. Uludag, P. A. Bandettini, and B. A. Poser. Techniques for blood volume fMRI with VASO: From low-resolution mapping towards sub-millimeter layer-dependent

applications. *NeuroImage*, (November), 2016b. ISSN 10538119. doi: 10.1016/j.neuroimage.2016.11.039. URL http://www.ncbi.nlm.nih.gov/pubmed/27867088{%}5Cnhttp://linkinghub.elsevier.com/retrieve/pii/S1053811916306589.

S. A. Huettel, A. W. Song, and G. McCarthy. *Functional Magnetic Resonance Imaging*, volume 1. Sinauer Associates Sunderland, 2004. ISBN 0878932887.

A. C. Hurley, A. Al-Radaideh, L. Bai, U. Aickelin, R. Coxon, P. Glover, and P. A. Gowland. Tailored RF pulse for magnetization inversion at ultrahigh field. *Magnetic Resonance in Medicine*, 63(1):51–58, 2010. ISSN 07403194. doi: 10.1002/mrm.22167.

C. Iadecola. Regulation of the cerebral microcirculation during neural activity: is nitric oxide the missing link? *Trends in neurosciences*, 16(6):206–14, 1993. ISSN 0166-2236. doi: 10.1016/0166-2236(93)90156-G. URL http://www.ncbi.nlm.nih.gov/pubmed/7688160.

C. Iadecola and M. Nedergaard. Glial regulation of the cerebral microvasculature. *Nature Neuroscience*, 10(11):1369–1376, 2007. ISSN 1097-6256. doi: 10.1038/nn2003. URL http://www.nature.com/doifinder/10.1038/nn2003.

H. Ito, I. Kanno, C. Kato, T. Sasaki, K. Ishii, Y. Ouchi, A. Iida, H. Okazawa, K. Hayashida, N. Tsuyuguchi, K. Ishii, Y. Kuwabara, M. Senda, H. Ito, I. Kanno, C. Kato, T. Sasaki, K. Ishii, and Y. Ouchi. Database of normal human cerebral blood flow, cerebral blood volume, cerebral oxygen extraction fraction and cerebral metabolic rate of oxygen measured by positron emission tomography with 15 O-labelled carbon dioxide or water, carbon monoxide and oxygen:. *European Journal of Nuclear Medicine and Molecular Imaging*, 31(5):635–643, 2004. ISSN 1619-7070. doi: 10.1007/s00259-003-1430-8. URL http://link.springer.com/10.1007/s00259-003-1430-8.

D. Ivanov. *Functional mapping of hemodynamic parameters and oxygen utilization in human brain using magnetic resonance imaging techniques at 7 Tesla*. PhD thesis, Universit\"at Leipzig, 2012.

D. Ivanov, A. Schäfer, A. Deistung, M. N. Streicher, S. Kabisch, I. Henseler, E. Roggenhofer, T. H. Jochimsen, F. Schweser, J. R. Reichenbach, K. Uludag, and R. Turner. In vivo estimation of the transverse relaxation time dependence of blood on oxygenation at 7 tesla. In *Proceedings of the 21st Annual Meeting of ISMRM, Salt Lake City, USA*, page 2472, 2013.

J. Jeener, B. H. Meier, P. Bachmann, and R. R. Ernst. Investigation of exchange processes by two-dimensional NMR spectroscopy. *Journal of Chemical Physics*, 71(11):4546–4553, 1979. ISSN 00219606 (ISSN). doi: 10.1063/1.438208. URL http://www.scopus.com/inward/

record.url?eid=2-s2.0-0343359244{&}partnerID=40{&}md5=40eaad0fd12b399b96046f2c64ce134b.

M. Jenkinson, C. F. Beckmann, T. E. J. Behrens, M. W. Woolrich, and S. M. Smith. Fsl. *NeuroImage*, 62(2):782–790, 2012. ISSN 10538119. doi: 10.1016/j.neuroimage.2011.09.015. URL http://linkinghub.elsevier.com/retrieve/pii/S1053811911010603.

S. N. Jespersen and L. Østergaard. The roles of cerebral blood flow, capillary transit time heterogeneity, and oxygen tension in brain oxygenation and metabolism. *Journal of cerebral blood flow and metabolism : official journal of the International Society of Cerebral Blood Flow and Metabolism*, 32(2):264–77, 2012. ISSN 1559-7016. doi: 10.1038/jcbfm.2011.153. URL http://www.ncbi.nlm.nih.gov/pubmed/22044867{%}5Cnhttp://www.pubmedcentral.nih.gov/articlerender.fcgi?artid=PMC3272609.

T. Jin and S.-G. Kim. Cortical layer-dependent dynamic blood oxygenation, cerebral blood flow and cerebral blood volume responses during visual stimulation. *NeuroImage*, 43(1):1–9, oct 2008a. ISSN 1095-9572. doi: 10.1016/j.neuroimage.2008.06.029. URL http://www.pubmedcentral.nih.gov/articlerender.fcgi?artid=2579763{&}tool=pmcentrez{&}rendertype=abstract.

T. Jin and S.-G. Kim. Improved cortical-layer specificity of vascular space occupancy fMRI with slab inversion relative to spin-echo BOLD at 9.4 T. *NeuroImage*, 40(1):59–67, mar 2008b. ISSN 1053-8119. doi: 10.1016/j.neuroimage.2007.11.045. URL http://www.pubmedcentral.nih.gov/articlerender.fcgi?artid=2375293{&}tool=pmcentrez{&}rendertype=abstract.

T. H. Jochimsen and M. von Mengershausen. ODIN - Object-oriented Development Interface for NMR. *Journal of Magnetic Resonance*, 170 (1):67–78, 2004. ISSN 10907807. doi: 10.1016/j.jmr.2004.05.021.

T. Kaneko, M. A. Caria, and H. Asanuma. Information processing within the motor cortex. II. Intracortical connections between neurons receiving somatosensory cortical input and motor output neurons of the cortex. *Journal of Comparative Neurology*, 345(2):172–184, 1994. ISSN 10969861. doi: 10.1002/cne.903450203.

S. S. Kannurpatti and B. B. Biswal. Detection and scaling of task-induced fMRI-BOLD response using resting state fluctuations. *NeuroImage*, 40(4):1567–74, may 2008. ISSN 1053-8119. doi: 10.1016/j.neuroimage.2007.09.040. URL http://www.ncbi.nlm.nih.gov/pubmed/18343159.

S. S. Kannurpatti, B. Rypma, and B. B. Biswal. Prediction of Task-Related BOLD fMRI with Amplitude Signatures of Resting-State fMRI. *Frontiers in systems neuroscience*, 6(March):

7, jan 2012. ISSN 1662-5137. doi: 10.3389/fnsys.2012.00007. URL http://www.pubmedcentral.nih.gov/articlerender.fcgi?artid=3294272{&}tool=pmcentrez{&}rendertype=abstract.

A. J. Kennerley, J. Berwick, J. Martindale, D. Johnston, N. Papadakis, and J. E. Mayhew. Concurrent fMRI and optical measures for the investigation of the hemodynamic response function. *Magnetic resonance in medicine : official journal of the Society of Magnetic Resonance in Medicine / Society of Magnetic Resonance in Medicine*, 54(2):354–65, aug 2005. ISSN 0740-3194. doi: 10.1002/mrm.20511. URL http://www.ncbi.nlm.nih.gov/pubmed/16032695.

A. J. Kennerley, J. Berwick, J. Martindale, D. Johnston, Y. Zheng, and J. E. Mayhew. Refinement of optical imaging spectroscopy algorithms using concurrent BOLD and CBV fMRI. *NeuroImage*, 47(4):1608–1619, 2009. ISSN 10538119. doi: 10.1016/j.neuroimage.2009.05.092.

A. J. Kennerley, S. Harris, M. Bruyns-Haylett, L. Boorman, Y. Zheng, M. Jones, and J. Berwick. Early and late stimulus-evoked cortical hemodynamic responses provide insight into the neurogenic nature of neurovascular coupling. *Journal of Cerebral Blood Flow & Metabolism*, 32(3):468–480, 2012. ISSN 0271-678X. doi: 10.1038/jcbfm.2011.163. URL http://dx.doi.org/10.1038/jcbfm.2011.163.

I. Kida, R. P. Kennan, D. L. Rothman, K. L. Behar, and F. Hyder. High-resolution CMR(O2) mapping in rat cortex: a multiparametric approach to calibration of BOLD image contrast at 7 Tesla. *Journal of cerebral blood flow and metabolism : official journal of the International Society of Cerebral Blood Flow and Metabolism*, 20(5):847–60, 2000. ISSN 0271-678X. doi: 10.1097/00004647-200005000-00012. URL http://jcb.sagepub.com/content/20/5/847.full.

S.-G. Kim and S. Ogawa. Biophysical and physiological origins of blood oxygenation level-dependent fMRI signals. *Journal of cerebral blood flow and metabolism : official journal of the International Society of Cerebral Blood Flow and Metabolism*, 32(7):1188–206, jul 2012. ISSN 1559-7016. doi: 10.1038/jcbfm.2012.23. URL http://www.pubmedcentral.nih.gov/articlerender.fcgi?artid=3390806{&}tool=pmcentrez{&}rendertype=abstract.

S. G. Kim and K. Ugurbil. High-resolution functional magnetic resonance imaging of the animal brain. *Methods*, 30(1):28–41, 2003. ISSN 10462023. doi: 10.1016/S1046-2023(03)00005-7.

S.-G. Kim, N. Harel, T. Jin, T. Kim, P. Lee, and F. Zhao. Cerebral blood volume MRI with intravascular superparamagnetic iron oxide nanoparticles. *NMR in biomedicine*, 26

(8):949–62, aug 2013. ISSN 1099-1492. doi: 10.1002/nbm.2885. URL http://www.pubmedcentral.nih.gov/articlerender.fcgi?artid=3700592{&}tool=pmcentrez{&}rendertype=abstract.

T. Kim and S.-G. Kim. Temporal dynamics and spatial specificity of arterial and venous blood volume changes during visual stimulation: implication for BOLD quantification. *Journal of cerebral blood flow and metabolism : official journal of the International Society of Cerebral Blood Flow and Metabolism*, 31(5):1211–1222, 2011. ISSN 1559-7016. doi: 10.1038/jcbfm.2010.226. URL http://dx.doi.org/10.1038/jcbfm.2010.226.

V. Kiviniemi, J. Jauhiainen, O. Tervonen, E. Pääkkö, J. Oikarinen, V. Vainionpää, H. Rantala, and B. Biswal. Slow vasomotor fluctuation in fMRI of anesthetized child brain. *Magnetic Resonance in Medicine*, 44(3):373–378, 2000. ISSN 07403194. doi: 10.1002/1522-2594(200009)44:3<373::AID-MRM5>3.0.CO;2-P.

P. J. Koopmans, R. Manniesing, W. J. Niessen, M. A. Viergever, and M. Barth. MR venography of the human brain using susceptibility weighted imaging at very high field strength. *Magnetic Resonance Materials in Physics, Biology and Medicine*, 21(1-2):149–158, 2008. ISSN 09685243. doi: 10.1007/s10334-007-0101-3.

P. J. Koopmans, M. Barth, S. Orzada, and D. G. Norris. Multi-echo fMRI of the cortical laminae in humans at 7 T. *NeuroImage*, 56(3):1276–85, jun 2011. ISSN 1095-9572. doi: 10.1016/j.neuroimage.2011.02.042. URL http://www.ncbi.nlm.nih.gov/pubmed/21338697.

P. J. Koopmans, R. Boyacioglu, M. Barth, and D. G. Norris. Simultaneous multislice inversion contrast imaging using power independent of the number of slices (PINS) and delays alternating with nutation for tailored excitation (DANTE) radio frequency pulses. *Magnetic Resonance in Medicine*, 69(6):1670–1676, 2013. ISSN 07403194. doi: 10.1002/mrm.24402.

C. Kramer, H. J. Gerhardt, and W. Bleifeld. A model for closure of arterial vessels with special regard to the coronary arteries. *Basic Research in Cardiology*, 69(6):585–596, 1974. ISSN 03008428. doi: 10.1007/BF01914494.

S. N. Krieger, C. J. Gauthier, D. Ivanov, L. Huber, E. Roggenhofer, B. Sehm, R. Turner, and G. F. Egan. Regional reproducibility of calibrated BOLD functional MRI: Implications for the study of cognition and plasticity. *NeuroImage*, 101:8–20, 2014a. ISSN 10959572. doi: 10.1016/j.neuroimage.2014.06.072. URL http://dx.doi.org/10.1016/j.neuroimage.2014.06.072.

S. N. Krieger, D. Ivanov, L. Huber, E. Roggenhofer, B. Sehm, R. Turner, G. F. Egan, and C. J. Gauthier. Using carbogen for calibrated fMRI

at 7Tesla: comparison of direct and modelled estimation of the M parameter. *NeuroImage*, 84:605–14, jan 2014b. ISSN 1095-9572. doi: 10.1016/j.neuroimage.2013.09.035. URL http://www.ncbi.nlm.nih.gov/pubmed/24071526.

G. Krüger and G. H. Glover. Physiological noise in oxygenation-sensitive magnetic resonance imaging. *Magnetic Resonance in Medicine*, 46(4):631–637, 2001. ISSN 07403194. doi: 10.1002/mrm.1240.

G. Krüger, A. Kastrup, and G. H. Glover. Neuroimaging at 1.5 T and 3.0 T: Comparison of Oxygenation-Sensitive Magnetic Resonance Imaging. *Magnetic Resonance in Medicine*, 45:595–604, 2001.

A. Kumar, R. Ernst, and K. Wüthrich. A two-dimensional nuclear Overhauser enhancement (2D NOE) experiment for the elucidation of complete proton-proton cross-relaxation networks in biological macromolecules. *Biochemical and Biophysical Research Communications*, 95(1):1–6, 1980. ISSN 0006291X. doi: 10.1016/0006-291X(80)90695-6. URL http://www.sciencedirect.com/science/article/pii/0006291X80906956{%}5Cnhttp://linkinghub.elsevier.com/retrieve/pii/0006291X80906956{%}5Cnhttp://www.ncbi.nlm.nih.gov/pubmed/7417242{%}5Cnhttp://linkinghub.elsevier.com/retrieve/pii/0006291X80906956.

K. K. Kwong, J. W. Belliveau, D. A. Chesler, I. E. Goldberg, R. M. Weisskoff, B. P. Poncelet, D. N. Kennedy, B. E. Hoppel, M. S. Cohen, and R. Turner. Dynamic magnetic resonance imaging of human brain activity during primary sensory stimulation. *Proceedings of the National Academy of Sciences of the United States of America*, 89(12):5675–5679, 1992. ISSN 0027-8424. doi: 10.1073/pnas.89.12.5675. URL http://www.pubmedcentral.nih.gov/articlerender.fcgi?artid=49355{&}tool=pmcentrez{&}rendertype=abstract.

D. J. Larkman, J. V. Hajnal, A. H. Herlihy, G. A. Coutts, I. R. Young, and G. Ehnholm. Use of multicoil arrays for separation of signal from multiple slices simultaneously excited. *Journal of Magnetic Resonance Imaging*, 13(2):313–317, 2001. ISSN 10531807. doi: 10.1002/1522-2586(200102)13:2<313::AID-JMRI1045>3.0.CO;2-W.

P. C. Lauterbur. Image formation by induced local interactions. Examples employing nuclear magnetic resonance. *Nature (London, United Kingdom)*, 242:190–191, 1973. ISSN 0028-0836. doi: 10.1038/242190a0.

F. Lauwers, F. Cassot, V. Lauwers-Cances, P. Puwanarajah, and H. Duvernoy. Morphometry of the human cerebral cortex microcirculation: General characteristics and space-related profiles. *NeuroIm-*

age, 39(3):936–948, 2008. ISSN 10538119. doi: 10.1016/j.neuroimage.2007.09.024.

S. P. Lee, T. Q. Duong, G. Yang, C. Iadecola, and S. G. Kim. Relative changes of cerebral arterial and venous blood volumes during increased cerebral blood flow: Implications for bold fMRI. *Magnetic Resonance in Medicine*, 45(5):791–800, 2001. ISSN 07403194. doi: 10.1002/mrm.1107.

L. D. Lewis, K. Setsompop, B. R. Rosen, and J. R. Polimeni. Fast fMRI can detect oscillatory neural activity in humans. *Proceedings of the National Academy of Sciences*, 113(43):E6679–E6685, 2016. ISSN 0027-8424. doi: 10.1073/pnas.1608117113.

T. Q. Li, P. van Gelderen, H. Merkle, L. Talagala, A. P. Koretsky, and J. Duyn. Extensive heterogeneity in white matter intensity in high-resolution T2*-weighted MRI of the human brain at 7.0 T. *NeuroImage*, 32(3):1032–1040, 2006. ISSN 10538119. doi: 10.1016/j.neuroimage.2006.05.053.

I. Lipp, K. Murphy, X. Caseras, and R. G. Wise. Agreement and repeatability of vascular reactivity estimates based on a breath-hold task and a resting state scan. *NeuroImage*, 113:387–396, 2015. ISSN 10959572. doi: 10.1016/j.neuroimage.2015.03.004. URL `http://dx.doi.org/10.1016/j.neuroimage.2015.03.004`.

P. Liu, A. C. Hebrank, K. M. Rodrigue, K. M. Kennedy, D. C. Park, and H. Lu. A comparison of physiologic modulators of fMRI signals. *Human brain mapping*, 34(9):2078–88, sep 2013a. ISSN 1097-0193. doi: 10.1002/hbm.22053. URL `http://www.pubmedcentral.nih.gov/articlerender.fcgi?artid=3432155{&}tool=pmcentrez{&}rendertype=abstract`.

P. Liu, A. C. Hebrank, K. M. Rodrigue, K. M. Kennedy, J. Section, D. C. Park, and H. Lu. Age-related differences in memory-encoding fMRI responses after accounting for decline in vascular reactivity. *NeuroImage*, 78:415–425, 2013b. ISSN 10538119. doi: 10.1016/j.neuroimage.2013.04.053. URL `http://dx.doi.org/10.1016/j.neuroimage.2013.04.053`.

P. Liu, Y. Li, M. Pinho, D. C. Park, B. G. Welch, and H. Lu. Cerebrovascular reactivity mapping without gas challenges. *NeuroImage*, 146(November 2016):320–326, 2017. ISSN 10959572. doi: 10.1016/j.neuroimage.2016.11.054. URL `http://dx.doi.org/10.1016/j.neuroimage.2016.11.054`.

T. T. Liu. Neurovascular factors in resting-state functional MRI. *NeuroImage*, 80:339–348, 2013. ISSN 10538119. doi: 10.1016/j.neuroimage.2013.04.071. URL `http://dx.doi.org/10.1016/j.neuroimage.2013.04.071`.

N. K. Logothetis, J. Pauls, M. Augath, T. Trinath, and a. Oeltermann. Neurophysiological investigation of the basis of the fMRI signal. *Nature*, 412(6843):150–7, jul 2001. ISSN 0028-0836. doi: 10.1038/35084005. URL http://www.ncbi.nlm.nih.gov/pubmed/11449264.

H. Lu and P. C. M. van Zijl. Experimental measurement of extravascular parenchymal BOLD effects and tissue oxygen extraction fractions using multi-echo VASO fMRI at 1.5 and 3.0 T. *Magnetic resonance in medicine : official journal of the Society of Magnetic Resonance in Medicine / Society of Magnetic Resonance in Medicine*, 53(4):808–16, apr 2005. ISSN 0740-3194. doi: 10.1002/mrm.20379. URL http://www.ncbi.nlm.nih.gov/pubmed/15799063.

H. Lu, X. Golay, J. J. Pekar, and P. C. M. Van Zijl. Functional magnetic resonance imaging based on changes in vascular space occupancy. *Magnetic resonance in medicine : official journal of the Society of Magnetic Resonance in Medicine / Society of Magnetic Resonance in Medicine*, 50(2):263–74, aug 2003. ISSN 0740-3194. doi: 10.1002/mrm.10519. URL http://www.ncbi.nlm.nih.gov/pubmed/12876702.

H. Lu, C. Zhao, Y. Ge, and K. Lewis-Amezcua. Baseline blood oxygenation modulates response amplitude: Physiologic basis for intersubject variations in functional MRI signals. *Magnetic Resonance in Medicine*, 60(2):364–372, 2008. ISSN 07403194. doi: 10.1002/mrm.21686.

H. Lu, J. Hutchison, F. Xu, and B. Rypma. The Relationship Between M in "Calibrated fMRI" and the Physiologic Modulators of fMRI. *The open neuroimaging journal*, 5:112–9, jan 2011. ISSN 1874-4400. doi: 10.2174/1874440001105010112. URL http://www.pubmedcentral.nih.gov/articlerender.fcgi?artid=3263507{&}tool=pmcentrez{&}rendertype=abstract.

H. Lu, J. Hua, and P. Zijl. Noninvasive functional imaging of cerebral blood volume with vascular space occupancy (VASO) MRI. *NMR in Biomedicine*, 26(October 2012):932–948, 2013. doi: 10.1002/nbm.2905. URL http://onlinelibrary.wiley.com/doi/10.1002/nbm.2905/full.

Y. Ma, M. A. Shaik, M. G. Kozberg, S. H. Kim, J. P. Portes, D. Timerman, and E. M. C. Hillman. Resting-state hemodynamics are spatiotemporally coupled to synchronized and symmetric neural activity in excitatory neurons. *Proceedings of the National Academy of Sciences*, 113(52):E8463–E8471, 2016. ISSN 0027-8424. doi: 10.1073/pnas.1525369113. URL http://www.pnas.org/lookup/doi/10.1073/pnas.1525369113.

P. Mansfield. Multi-planar image formation using NMR spin echoes. *Journal of Physics C: Solid State Physics*, 10(3):L55, 1977.

D. S. Margulies, J. Böttger, X. Long, Y. Lv, C. Kelly, A. Schäfer, D. Goldhahn, A. Abbushi, M. P. Milham, G. Lohmann, and A. Villringer. Resting developments: a review of fMRI post-processing methodologies for spontaneous brain activity. *Magma (New York, N.Y.)*, 23(5-6):289–307, dec 2010. ISSN 1352-8661. doi: 10.1007/s10334-010-0228-5. URL http://www.ncbi.nlm.nih.gov/pubmed/20972883.

I. Markuerkiaga, M. Barth, and D. G. Norris. A cortical vascular model for examining the specificity of the laminar BOLD signal. *NeuroImage*, 132:491–498, 2016. ISSN 1095-9572. doi: 10.1016/j.neuroimage.2016.02.073. URL http://www.sciencedirect.com/science/article/pii/S1053811916001919.

J. P. Marques, T. Kober, G. Krueger, W. van der Zwaag, P.-F. Van de Moortele, and R. Gruetter. MP2RAGE, a self bias-field corrected sequence for improved segmentation and T1-mapping at high field. *NeuroImage*, 49(2):1271–1281, 2010. ISSN 10538119. doi: 10.1016/j.neuroimage.2009.10.002. URL http://linkinghub.elsevier.com/retrieve/pii/S1053811909010738.

J. Martindale, A. J. Kennerley, D. Johnston, Y. Zheng, and J. E. Mayhew. Theory and generalization of Monte Carlo models of the BOLD signal source. *Magnetic Resonance in Medicine*, 59(3):607–618, 2008. ISSN 07403194. doi: 10.1002/mrm.21512.

A. Maudsley. Multiple-line-scanning spin density imaging. *Journal of Magnetic Resonance (1969)*, 41(1):112–126, 1980. ISSN 00222364. doi: 10.1016/0022-2364(80)90207-3. URL http://www.sciencedirect.com/science/article/pii/0022236480902073.

R. S. Menon. Postacquisition Suppression of Large-Vessel BOLD Signals in High-Resolution fMRI. 9:1–9, 2002. doi: 10.1002/mrm.10041.

S. Moeller, E. Yacoub, C. a. Olman, E. Auerbach, J. Strupp, N. Harel, and K. Ugurbil. Multiband multislice GE-EPI at 7 tesla, with 16-fold acceleration using partial parallel imaging with application to high spatial and temporal whole-brain fMRI. *Magnetic resonance in medicine : official journal of the Society of Magnetic Resonance in Medicine / Society of Magnetic Resonance in Medicine*, 63(5):1144–53, may 2010. ISSN 1522-2594. doi: 10.1002/mrm.22361. URL http://www.pubmedcentral.nih.gov/articlerender.fcgi?artid=2906244{&}tool=pmcentrez{&}rendertype=abstract.

F. B. Mohamed. *Functional MRI: basic principles and clinical applications*. Springer Science \& Business Media, 2006.

A. Mosso. Concerning the circulation of the blood in the human brain. *Leipzig: Verlag von Viet \& Company*, 1881.

A. Mosso. *Applicazione della bilancia allo studio della circolazione sanguigna nell'uomo*. Salviucci, 1884.

L. Muckli, F. De Martino, L. Vizioli, L. S. Petro, F. W. Smith, K. Ugurbil, R. Goebel, and E. Yacoub. Contextual Feedback to Superficial Layers of V1. *Current Biology*, 25(20):2690–2695, 2015. ISSN 09609822. doi: 10.1016/j.cub.2015.08.057. URL http://dx.doi.org/10.1016/j.cub.2015.08.057.

S. Müller. Multifrequency selective rf pulses for multislice MR imaging. *Magnetic Resonance in Medicine*, 6(3):364–371, 1988. ISSN 15222594. doi: 10.1002/mrm.1910060315.

K. Murphy, J. Bodurka, and P. a. Bandettini. How long to scan? The relationship between fMRI temporal signal to noise ratio and necessary scan duration. *NeuroImage*, 34(2):565–74, 2007. ISSN 1053-8119. doi: 10.1016/j.neuroimage.2006.09.032. URL http://www.pubmedcentral.nih.gov/articlerender.fcgi?artid=2223273{&}tool=pmcentrez{&}rendertype=abstract.

S. Ogawa, T. M. Lee, A. R. Kay, and D. W. Tank. Brain magnetic resonance imaging with contrast dependent on blood oxygenation. *Proceedings of the National Academy of Sciences of the United States of America*, 87(24):9868–72, 1990. ISSN 0027-8424. doi: 10.1073/pnas.87.24.9868. URL http://www.pubmedcentral.nih.gov/articlerender.fcgi?artid=55275{&}tool=pmcentrez{&}rendertype=abstract.

S. Ogawa, R. S. Menon, D. W. Tank, S. G. Kim, H. Merkle, J. M. Ellermann, and K. Ugurbil. Functional brain mapping by blood oxygenation level-dependent contrast magnetic resonance imaging. A comparison of signal characteristics with a biophysical model. *Biophysical journal*, 64(3):803–812, 1993. ISSN 0006-3495. doi: 10.1016/S0006-3495(93)81441-3. URL http://www.sciencedirect.com/science/article/pii/S0006349593814413.

C. a. Olman, N. Harel, D. a. Feinberg, S. He, P. Zhang, K. Ugurbil, and E. Yacoub. Layer-specific fMRI reflects different neuronal computations at different depths in human V1. *PloS one*, 7(3):e32536, jan 2012. ISSN 1932-6203. doi: 10.1371/journal.pone.0032536. URL http://www.pubmedcentral.nih.gov/articlerender.fcgi?artid=3308958{&}tool=pmcentrez{&}rendertype=abstract.

S.-H. Park, T. Hayashi, and S.-G. Kim. Determination of Intracortical Venous Vessel Density Using Venography at 9.4 T. In *Proceedings of the 13th Annual Meeting of the ISMRM*, page 1410, 2005.

L. Pellerin and P. J. Magistretti. Glutamate uptake into astrocytes stimulates aerobic glycolysis: a mechanism coupling neuronal activity to glucose utilization. *Proceedings of the National Academy of Sciences*, 91(22):10625–10629, 1994. ISSN 0027-8424. doi: 10.1073/pnas.91.22.

10625. URL http://www.pnas.org/cgi/doi/10.1073/pnas.91.22.10625.

A. M. Peters, M. J. Brookes, F. G. Hoogenraad, P. A. Gowland, S. T. Francis, P. G. Morris, and R. Bowtell. T2* measurements in human brain at 1.5, 3 and 7 T. *Magnetic Resonance Imaging*, 25(6):748–753, 2007. ISSN 0730725X. doi: 10.1016/j.mri.2007.02.014.

J. Pfeuffer, G. Adriany, A. Shmuel, E. Yacoub, P. F. Van De Moortele, X. Hu, and K. Ugurbil. Perfusion-based high-resolution functional imaging in the human brain at 7 Tesla. *Magnetic Resonance in Medicine*, 47(5):903–911, 2002. ISSN 07403194. doi: 10.1002/mrm.10154.

J. Pfeuffer, H. Merkle, M. Beyerlein, T. Steudel, and N. K. Logothetis. Anatomical and functional MR imaging in the macaque monkey using a vertical large-bore 7 Tesla setup. *Magnetic Resonance Imaging*, 22(10 SPEC. ISS.):1343–1359, 2004. ISSN 0730725X. doi: 10.1016/j.mri.2004.10.004.

S. K. Piechnik, P. A. Chiarelli, and P. Jezzard. Modelling vascular reactivity to investigate the basis of the relationship between cerebral blood volume and flow under CO2 manipulation. *NeuroImage*, 39 (1):107–118, 2008. ISSN 10538119. doi: 10.1016/j.neuroimage.2007.08.022.

G. B. Pike. Quantitative functional MRI: Concepts, issues and future challenges. *NeuroImage*, 62(2):1234–1240, 2012. ISSN 10538119. doi: 10.1016/j.neuroimage.2011.10.046. URL http://dx.doi.org/10.1016/j.neuroimage.2011.10.046.

J. R. Polimeni, M. Mianciardi, B. Keil, and L. L. Wald. Cortical depth dependence of physiological fluctuations and whole-brain resting-state functional connectivity at 7T. *Proceedings of the International Society of Magnetic Resonance in Medicine*, 23(2010):592, 2015.

J. R. Polimeni, H. Bhat, T. Witzel, T. Benner, T. Feiweier, S. J. Inati, V. Renvall, K. Heberlein, and L. L. Wald. Reducing sensitivity losses due to respiration and motion in accelerated echo planar imaging by reordering the autocalibration data acquisition. *Magnetic Resonance in Medicine*, 75(2):665–679, 2016. ISSN 15222594. doi: 10.1002/mrm.25628.

R. Porter and R. Lemon. *Corticospinal function and voluntary movement*. Oxford University Press, USA, 1993.

B. A. Poser and D. G. Norris. 3D single-shot VASO using a Maxwell gradient compensated GRASE sequence. *Magnetic resonance in medicine : official journal of the Society of Magnetic Resonance in Medicine / Society of Magnetic Resonance in Medicine*, 62(1):255–62,

jul 2009. ISSN 1522-2594. doi: 10.1002/mrm.22000. URL http://www.ncbi.nlm.nih.gov/pubmed/19319900.

B. A. Poser, P. J. Koopmans, T. Witzel, L. L. Wald, and M. Barth. Three dimensional echo-planar imaging at 7 Tesla. *NeuroImage*, 51(1): 261–6, may 2010. ISSN 1095-9572. doi: 10.1016/j.neuroimage.2010.01.108. URL http://www.pubmedcentral.nih.gov/articlerender.fcgi?artid=2853246{&}tool=pmcentrez{&}rendertype=abstract.

J. D. Power, A. Mitra, T. O. Laumann, A. Z. Snyder, B. L. Schlaggar, and S. E. Petersen. Methods to detect, characterize, and remove motion artifact in resting state fMRI. *NeuroImage*, 84:320–341, 2014. ISSN 10538119. doi: 10.1016/j.neuroimage.2013.08.048. URL http://dx.doi.org/10.1016/j.neuroimage.2013.08.048.

E. Purcell, H. Torrey, and R. Pound. Resonance Absorption by Nuclear Magnetic Moments in a Solid. *Physical Review*, 69(1-2): 37–38, 1946. ISSN 0031-899X. doi: 10.1103/PhysRev.69.37. URL http://journals.aps.org/pr/abstract/10.1103/PhysRev.69.37{%}5Cnhttp://link.aps.org/doi/10.1103/PhysRev.69.37.

I. I. Rabi. Space quantization in a gyrating magnetic field. *Physical Review*, 51(8):652, 1937.

I. I. Rabi, S. Millman, P. Kusch, and J. R. Zacharias. The molecular beam resonance method for measuring nuclear magnetic moments. the magnetic moments of li 6 3, li 7 3 and f 19 9. *Physical Review*, 55 (6):526, 1939.

M. E. Raichle. Cognitive neuroscience: bold insights. *Nature*, 412 (6843):128–130, 2001.

S. M. Rao, P. a. Bandettini, J. R. Binder, J. a. Bobholz, T. a. Hammeke, E. a. Stein, and J. S. Hyde. Relationship between finger movement rate and functional magnetic resonance signal change in human primary motor cortex. *Journal of cerebral blood flow and metabolism : official journal of the International Society of Cerebral Blood Flow and Metabolism*, 16(6):1250–4, nov 1996. ISSN 0271-678X. doi: 10.1097/00004647-199611000-00020. URL http://www.ncbi.nlm.nih.gov/pubmed/8898698.

W. D. Rooney, G. Johnson, X. Li, E. R. Cohen, S. G. Kim, K. Ugurbil, and C. S. Springer. Magnetic field and tissue dependencies of human brain longitudinal 1H2O relaxation in vivo. *Magnetic Resonance in Medicine*, 57(2):308–318, 2007. ISSN 07403194. doi: 10.1002/mrm.21122.

E. Rostrup, G. M. Knudsen, I. Law, S. Holm, H. B. W. Larsson, and O. B. Paulson. The relationship between cerebral blood flow and

volume in humans. *NeuroImage*, 24(1):1–11, jan 2005. ISSN 1053-8119. doi: 10.1016/j.neuroimage.2004.09.043. URL http://www.ncbi.nlm.nih.gov/pubmed/15588591.

S. Sakadžić, E. T. Mandeville, L. Gagnon, J. J. Musacchia, M. A. Yaseen, M. A. Yucel, J. Lefebvre, F. Lesage, A. M. Dale, K. Eikermann-Haerter, C. Ayata, V. J. Srinivasan, E. H. Lo, A. Devor, and D. A. Boas. Large arteriolar component of oxygen delivery implies a safe margin of oxygen supply to cerebral tissue. *Nature Communications*, 5:5734, 2014. ISSN 2041-1723. doi: 10.1038/ncomms6734. URL http://www.pubmedcentral.nih.gov/articlerender.fcgi?artid=4260810{&}tool=pmcentrez{&}rendertype=abstract.

S. Sandrone, M. Bacigaluppi, M. R. Galloni, S. F. Cappa, A. Moro, M. Catani, M. Filippi, M. M. Monti, D. Perani, and G. Martino. Weighing brain activity with the balance: Angelo Mosso's original manuscripts come to light. *Brain*, 137(2):621–633, 2014. ISSN 14602156. doi: 10.1093/brain/awt091.

R. Scheeringa, P. J. Koopmans, T. van Mourik, O. Jensen, and D. G. Norris. The relationship between oscillatory EEG activity and the laminar-specific BOLD signal. *Proceedings of the National Academy of Sciences*, page 201522577, 2016. ISSN 0027-8424. doi: 10.1073/pnas.1522577113. URL http://www.pnas.org/lookup/doi/10.1073/pnas.1522577113.

F. Schmid, M. J. Barrett, P. Jenny, and B. Weber. Vascular density and distribution in neocortex. *NeuroImage*, 2017. ISSN 10538119. doi: 10.1016/j.neuroimage.2017.06.046. URL http://linkinghub.elsevier.com/retrieve/pii/S1053811917305165.

J. K. Seo, E. J. Woo, U. Katscher, and Y. Wang. *Electro-magnetic tissue properties MRI*. World Scientific, modelling edition, 2014.

Q. Shen, H. Ren, and T. Q. Duong. CBF, BOLD, CBV, and CMRO2 fMRI signal temporal dynamics at 500-msec resolution. *Journal of Magnetic Resonance Imaging*, 27(3):599–606, 2008. ISSN 10531807. doi: 10.1002/jmri.21203.

R. G. Shulman, F. Hyder, and D. L. Rothman. Lactate efflux and the neuroenergetic basis of brain function. *NMR in Biomedicine*, 14(7-8):389–396, 2001. ISSN 09523480. doi: 10.1002/nbm.741.

J. C. W. Siero, J. Hendrikse, H. Hoogduin, N. Petridou, P. Luijten, and M. J. Donahue. Cortical depth dependence of the BOLD initial dip and poststimulus undershoot in human visual cortex at 7 Tesla. *Magnetic Resonance in Medicine*, 73(6):2283–2295, 2015. ISSN 15222594. doi: 10.1002/mrm.25349.

S. P. Souza, J. Szumowski, C. L. Dumoulin, D. P. Plewes, and G. H. Glover. SIMA: simultaneous multislice acquisition of MR images by Hadamard-encoded excitation, 1988. ISSN 0363-8715. URL http://www.ncbi.nlm.nih.gov/pubmed/3183105.

B. Stefanovic, E. Hutchinson, V. Yakovleva, V. Schram, J. T. Russell, L. Belluscio, A. P. Koretsky, and A. C. Silva. Functional reactivity of cerebral capillaries. *Journal of cerebral blood flow and metabolism : official journal of the International Society of Cerebral Blood Flow and Metabolism*, 28(5):961–972, 2008. ISSN 0271-678X. doi: 10.1038/sj.jcbfm.9600590.

J. Stelzer, G. Lohmann, K. Mueller, T. Buschmann, and R. Turner. Deficient approaches to human neuroimaging. *Frontiers in Human Neuroscience*, 8(July):1–16, jul 2014. ISSN 1662-5161. doi: 10.3389/fnhum.2014.00462. URL http://www.frontiersin.org/Human{_}Neuroscience/10.3389/fnhum.2014.00462/abstract.

P. Tian, I. C. Teng, L. D. May, R. Kurz, K. Lu, M. Scadeng, E. M. C. Hillman, A. J. De Crespigny, H. E. D'Arceuil, J. B. Mandeville, J. J. A. Marota, B. R. Rosen, T. T. Liu, D. a. Boas, R. B. Buxton, A. M. Dale, and A. Devor. Cortical depth-specific microvascular dilation underlies laminar differences in blood oxygenation level-dependent functional MRI signal. *Proceedings of the National Academy of Sciences of the United States of America*, 107(34):15246–15251, 2010. ISSN 0027-8424. doi: 10.1073/pnas.1006735107.

R. H. N. Tijssen, M. Jenkinson, J. C. W. Brooks, P. Jezzard, and K. L. Miller. Optimizing RetroICor and RetroKCor corrections for multi-shot 3D FMRI acquisitions. *NeuroImage*, 84:394–405, 2014. ISSN 10538119. doi: 10.1016/j.neuroimage.2013.08.062. URL http://dx.doi.org/10.1016/j.neuroimage.2013.08.062.

R. Trampel, P.-L. Bazin, A. Schäfer, R. M. Heidemann, D. Ivanov, G. Lohmann, S. Geyer, and R. Turner. Laminar-specific fingerprints of different sensorimotor areas obtained during imagined and actual finger tapping. *Proc Intl Soc Mag Reson Med*, 20:663, 2012.

C. Triantafyllou, R. D. Hoge, G. Krueger, C. J. Wiggins, a. Potthast, G. C. Wiggins, and L. L. Wald. Comparison of physiological noise at 1.5 T, 3 T and 7 T and optimization of fMRI acquisition parameters. *NeuroImage*, 26(1):243–50, may 2005. ISSN 1053-8119. doi: 10.1016/j.neuroimage.2005.01.007. URL http://www.ncbi.nlm.nih.gov/pubmed/15862224.

C. Triantafyllou, J. R. Polimeni, and L. L. Wald. Physiological noise and signal-to-noise ratio in fMRI with multi-channel array coils. *NeuroImage*, 55(2):597–606, 2011. ISSN 10538119. doi: 10.1016/j.neuroimage.2010.11.084. URL http://dx.doi.org/10.1016/j.neuroimage.2010.11.084.

P. S. Tsai, J. P. Kaufhold, P. Blinder, B. Friedman, P. J. Drew, H. J. Karten, P. D. Lyden, and D. Kleinfeld. Correlations of Neuronal and Microvascular Densities in Murine Cortex Revealed by Direct Counting and Colocalization of Nuclei and Vessels. *Journal of Neuroscience*, 29(46):14553–14570, 2009. ISSN 0270-6474. doi: 10.1523/JNEUROSCI.3287-09.2009. URL http://www.jneurosci.org/cgi/doi/10.1523/JNEUROSCI.3287-09.2009.

J. Tsao. Interpolation artifacts in multimodality image registration based on maximization of mutual information. *IEEE Transactions on Medical Imaging*, 22(7):854–864, 2003. ISSN 02780062. doi: 10.1109/TMI.2003.815077.

R. Turner. How Much Cortex Can a Vein Drain? Downstream Dilution of Activation-Related Cerebral Blood Oxygenation Changes. *NeuroImage*, 16(4):1062–1067, aug 2002. ISSN 10538119. doi: 10.1006/nimg.2002.1082. URL http://linkinghub.elsevier.com/retrieve/pii/S1053811902910827.

D. B. Twieg. The k-trajectory formulation of the NMR imaging process with applications in analysis and synthesis of imaging methods., 1983. ISSN 0094-2405. URL http://www.ncbi.nlm.nih.gov/pubmed/6646065.

H. Uhlirova, K. Kılıç, P. Tian, M. Thunemann, M. Desjardins, P. A. Saisan, S. Sakadžić, T. V. Ness, C. Mateo, Q. Cheng, K. L. Weldy, F. Razoux, M. Vandenberghe, J. A. Cremonesi, C. G. L. Ferri, K. Nizar, V. B. Sridhar, T. C. Steed, M. Abashin, Y. Fainman, E. Masliah, S. Djurovic, O. A. Andreassen, G. A. Silva, D. A. Boas, D. Kleinfeld, R. B. Buxton, G. T. Einevol, A. M. Dale, and A. Devor. Cell type specificity of neurovascular coupling in cerebral cortex. *eLife*, 5(MAY2016):1–23, 2016. ISSN 2050084X. doi: 10.7554/eLife.14315.

S. Ulmer and O. Jansen. *fMRI: Basics and clinical applications*. Springer, 2010. ISBN 9783540681311. doi: 10.1007/978-3-540-68132-8.

K. Uludag. To dip or not to dip: Reconciling optical imaging and fMRI data. *Proceedings of the National Academy of Sciences*, 107(6):E23–E23, 2010. ISSN 0027-8424. doi: 10.1073/pnas.0914194107. URL http://www.pnas.org/cgi/doi/10.1073/pnas.0914194107.

K. Uludag, B. Müller-Bierl, and K. Ugurbil. An integrative model for neuronal activity-induced signal changes for gradient and spin echo functional imaging. *NeuroImage*, 48(1):150–65, oct 2009. ISSN 1095-9572. doi: 10.1016/j.neuroimage.2009.05.051. URL http://www.ncbi.nlm.nih.gov/pubmed/19481163.

K. Uludag, K. Ugurbil, and L. Berliner. *fMRI: From Nuclear Spins to Brain Functions*, volume 30. Springer, 2015. ISBN 9788578110796. doi: 10.1017/CBO9781107415324.004.

W. van der Zwaag, S. Francis, K. Head, A. Peters, P. Gowland, P. Morris, and R. Bowtell. fMRI at 1.5, 3 and 7 T: Characterising BOLD signal changes. *NeuroImage*, 47(4):1425–1434, 2009. ISSN 10538119. doi: 10.1016/j.neuroimage.2009.05.015. URL http://linkinghub.elsevier.com/retrieve/pii/S105381190900500X.

W. van der Zwaag, A. Schäfer, J. P. Marques, R. Turner, and R. Trampel. Recent applications of UHF-MRI in the study of human brain function and structure: a review. *NMR in biomedicine*, (October 2014), mar 2015. ISSN 1099-1492. doi: 10.1002/nbm.3275. URL http://www.ncbi.nlm.nih.gov/pubmed/25762497.

P. C. van Zijl, S. M. Eleff, J. a. Ulatowski, J. M. Oja, a. M. Ulug, R. J. Traystman, and R. a. Kauppinen. Quantitative assessment of blood flow, blood volume and blood oxygenation effects in functional magnetic resonance imaging. *Nature medicine*, 4(2):159–167, 1998. ISSN 1078-8956.

P. C. M. van Zijl, J. Hua, and H. Lu. The BOLD post-stimulus undershoot, one of the most debated issues in fMRI. *NeuroImage*, 62(2):1092–102, aug 2012. ISSN 1095-9572. doi: 10.1016/j.neuroimage.2012.01.029. URL http://www.pubmedcentral.nih.gov/articlerender.fcgi?artid=3356682{&}tool=pmcentrez{&}rendertype=abstract.

O. Viessmann, P. Jezzard, and H. E. Möller. Improved Characterization of Low-Frequency Fluctuations in Resting-State fMRI using GLM Correction of Baseline and Physiological Noise. In *Proceedings of the 24th Annual Meeting of the ISMRM*, page 3812, Singapore, 2016.

C. F. von Economo and G. N. Koskinas. *Die Cytoarchitektonik der Hirnrinde des erwachsenen Menschen*. Wien und Berlin: Julius Springer Verlag, 1925.

M. D. Waehnert, J. Dinse, M. Weiss, M. N. Streicher, P. Waehnert, S. Geyer, R. Turner, and P.-L. Bazin. Anatomically motivated modeling of cortical laminae. *NeuroImage*, 93 Pt 2:210–20, jun 2014. ISSN 1095-9572. doi: 10.1016/j.neuroimage.2013.03.078. URL http://www.ncbi.nlm.nih.gov/pubmed/23603284.

J. P. Wansapura, S. K. Holland, R. S. Dunn, and W. S. Ball. NMR relaxation times in the human brain at 3.0 Tesla. *Journal of Magnetic Resonance Imaging*, 9(4):531–538, 1999. ISSN 10531807. doi: 10.1002/(SICI)1522-2586(199904)9:4<531::AID-JMRI4>3.0.CO;2-L.

B. Weber, A. L. Keller, J. Reichold, and N. K. Logothetis. The microvascular system of the striate and extrastriate visual cortex of the macaque. *Cerebral cortex (New York, N.Y. : 1991)*, 18(10):2318–30, oct 2008. ISSN 1460-2199. doi: 10.1093/cercor/bhm259. URL http://www.ncbi.nlm.nih.gov/pubmed/18222935.

R. M. Weisskoff and S. Kiihne. MRI susceptometry: Image-based measurement of absolute susceptibility of MR contrast agents and human blood, 1992. ISSN 15222594.

R. G. Wise, K. Ide, M. J. Poulin, and I. Tracey. Resting fluctuations in arterial carbon dioxide induce significant low frequency variations in BOLD signal. *NeuroImage*, 21(4):1652–1664, 2004. ISSN 10538119. doi: 10.1016/j.neuroimage.2003.11.025.

E. Wong. Optimized Phase Schedules for Minimizing Peak RF Power in Simultaneous Multi-Slice RF Excitation Pulses. *Proceedings of the 20th Annual Meeting of ISMRM, Melbourne, Australia*, 20:2209, 2012.

M. Wyss, T. Kirchner, A. Ringenbach, K. P. Pruessmann, and A. Henning. Relaxation Parameter Mapping Adapted for 7T and Validation against Optimized Single Voxel MRS. In *Proceedings of the 21st Annual Meeting of ISMRM, Salt Lake City, USA*, page 2464, 2013.

F. Xu, J. Uh, M. R. Brier, J. Hart, U. S. Yezhuvath, H. Gu, Y. Yang, and H. Lu. The influence of carbon dioxide on brain activity and metabolism in conscious humans. *Journal of cerebral blood flow and metabolism : official journal of the International Society of Cerebral Blood Flow and Metabolism*, 31(1): 58–67, jan 2011. ISSN 1559-7016. doi: 10.1038/jcbfm.2010.153. URL http://www.pubmedcentral.nih.gov/articlerender.fcgi?artid=3049465{&}tool=pmcentrez{&}rendertype=abstract.

D. A. Yablonskiy and E. M. Haacke. Theory of NMR signal behavior in magnetically inhomogeneous tissues: The static dephasing regime. *Magnetic Resonance in Medicine*, 32(6):749–763, 1994. ISSN 07403194. doi: 10.1002/mrm.1910320610.

E. Yacoub, a. Shmuel, J. Pfeuffer, P. F. Van De Moortele, G. Adriany, P. Andersen, J. T. Vaughan, H. Merkle, K. Ugurbil, and X. Hu. Imaging brain function in humans at 7 Tesla. *Magnetic Resonance in Medicine*, 45(4):588–94, 2001a. ISSN 0740-3194. doi: 10.1002/mrm.1080. URL http://www.ncbi.nlm.nih.gov/pubmed/11283986.

E. Yacoub, A. Shmuel, J. Pfeuffer, P. F. Van De Moortele, G. Adriany, K. Ugurbil, and X. Hu. Investigation of the initial dip in fMRI at 7 Tesla. *NMR in Biomedicine*, 14(7-8):408–412, 2001b. ISSN 09523480. doi: 10.1002/nbm.715.

L. Yan, Y. Zhuo, Y. Ye, S. X. Xie, J. An, G. K. Aguirre, and J. Wang. Physiological origin of low-frequency drift in blood oxygen lcyci dependent (BOLD) functional magnetic resonance imaging (fMRI). *Magnetic Resonance in Medicine*, 61(4):819–827, 2009. ISSN 07403194. doi: 10.1002/mrm.21902.

C. C. C. Yen, D. Papoti, and A. C. Silva. Investigating the spatiotemporal characteristics of the deoxyhemoglobin-related and deoxyhemoglobin-unrelated functional hemodynamic response across cortical layers in awake marmosets. *NeuroImage*, (March): 1–10, 2017. ISSN 10959572. doi: 10.1016/j.neuroimage.2017.03.005. URL http://dx.doi.org/10.1016/j.neuroimage.2017.03.005.

X. Yu, C. Qian, D.-y. Chen, S. J. Dodd, and A. P. Koretsky. Deciphering laminar-specific neural inputs with line-scanning fMRI. *Nature methods*, 11(1):55–8, jan 2014. ISSN 1548-7105. doi: 10.1038/nmeth.2730. URL http://www.ncbi.nlm.nih.gov/pubmed/24240320.

M. Zaitsev, B. Akin, P. LeVan, and B. R. Knowles. Prospective motion correction in functional MRI. *NeuroImage*, 154(November 2016):33–42, 2017. ISSN 10959572. doi: 10.1016/j.neuroimage.2016.11.014. URL http://dx.doi.org/10.1016/j.neuroimage.2016.11.014.

Y.-F. Zang, Y. He, C.-Z. Zhu, Q.-J. Cao, M.-Q. Sui, M. Liang, L.-X. Tian, T.-Z. Jiang, and Y.-F. Wang. Altered baseline brain activity in children with ADHD revealed by resting-state functional MRI. *Brain & development*, 29(2):83–91, mar 2007. ISSN 0387-7604. doi: 10.1016/j.braindev.2006.07.002. URL http://www.ncbi.nlm.nih.gov/pubmed/16919409.

A. C. Zappe, K. Uludag, A. Oeltermann, K. Ugurbil, and N. K. Logothetis. The influence of moderate hypercapnia on neural activity in the anesthetized nonhuman primate. *Cerebral cortex (New York, N.Y. : 1991)*, 18(11):2666–73, nov 2008. ISSN 1460-2199. doi: 10.1093/cercor/bhn023. URL http://www.pubmedcentral.nih.gov/articlerender.fcgi?artid=2567427{&}tool=pmcentrez{&}rendertype=abstract.

Q. H. Zou, C. Z. Zhu, Y. Yang, X. N. Zuo, X. Y. Long, Q. J. Cao, Y. F. Wang, and Y. F. Zang. An improved approach to detection of amplitude of low-frequency fluctuation (ALFF) for resting-state fMRI: Fractional ALFF. *Journal of Neuroscience Methods*, 172(1):137–141, 2008. ISSN 01650270. doi: 10.1016/j.jneumeth.2008.04.012.

COLOPHON

This document was typeset using the typographical look-and-feel `classicthesis` developed by André Miede. The style was inspired by Robert Bringhurst's seminal book on typography "*The Elements of Typographic Style*". `classicthesis` is available for both LaTeX and LyX:

`http://code.google.com/p/classicthesis/`